5-1993

Development of New Methods for Assessing Solidification/Stabilization of Hazardous Waste Using Solid-State Nuclear Magnetic Resonance Techniques (Ph.D Dissertation, LSU)

Michael A. Janusa
janusama@sfasu.edu

Order Number 9401540

Development of new methods for assessing solidification/stabilization of hazardous waste using solid-state nuclear magnetic resonance techniques

Janusa, Michael A., Ph.D.

The Louisiana State University and Agricultural and Mechanical Col., 1993

U·M·I
300 N. Zeeb Rd.
Ann Arbor, MI 48106

DEVELOPMENT OF NEW METHODS FOR ASSESSING SOLIDIFICATION/STABILIZATION OF HAZARDOUS WASTE USING SOLID-STATE NUCLEAR MAGNETIC RESONANCE TECHNIQUES

A Dissertation

Submitted to the Graduate Faculty of the
Louisiana State University and
Agricultural and Mechanical College
in partial fulfillment of the
requirements for the degree of
Doctor of Philosophy

in

The Department of Chemistry

by
Michael A. Janusa
B.S., Louisiana Tech University, 1985
May 1993

ACKNOWLEDGEMENTS

I would like to thank Dr. Leslie G. Butler, my research director, for his guidance and support during my graduate studies at Louisiana State University. I deeply appreciate his dedication in developing my career as a scientist and allowing me to do research in my area of interest, environmental, instead of his normal area of interest. I am especially thankful to Dr. Frank K. Cartledge, whose constant support, encouragement, and helpful discussions will always be remembered.

The financial support of the LSU Center for Energy Studies is gratefully acknowledged. The purchase of the solid-state NMR spectrometer was made possible, in part, by a grant from the National Science Foundation (CHE-8711788) and by the Louisiana Educational Quality Support Fund. This research has been supported in part with Federal Funds as part of the program of the Gulf Coast Hazardous Substance Research Center, which is supported under cooperative R815197 with the United States Environmental Protection Agency. In addition, I wish to thank the Charles E. Coates Memorial Fund for financial assistance in preparing this dissertation.

I would like to express my appreciation to a number of colleagues at Louisiana State University, namely AeJa Kim, Xiao Wu, and Humayoun Akhter. There is one colleague, Youngil Lee, that I am very appreciative of his friendship and constant encouragement throughout my stay at Louisiana State University. His friendship is treasured and will be remembered for life.

Finally, I would not have made it very far without my family. I found inspiration and support through my mother's and father's unconditional love. The patience and endurance shown by my wife, Cheryl, deserves a special thanks and is well appreciated.

IN MEMORIAM OF

MY GRANDFATHERS

TABLE OF CONTENTS

LIST OF FIGURES

ABSTRACT

New methods for assessing solidification/stabilization (S/S) of hazardous waste using solid–state nuclear magnetic resonance are developed for the purpose of diagnosing on a microscopic level the performance of S/S as a hazardous waste disposal technique. There are four techniques developed and described in this dissertation: (1) Solid–state deuterium NMR spectroscopy is used to determine if a particular deuterated organic waste is effectively solidified/stabilized and to determine the lower limit of the bond strength between the waste and the cement matrix; (2) Constant time pulsed field gradient ^{1}H NMR spectroscopy is tested on a liquid waste encapsulated within a solidified matrix to determine if droplets of liquid waste are entrapped within a solidified matrix. It yields a size distribution image of vesicles containing fluids, and measures the diffusion rate of organic materials in solid matrices; (3) Three–dimensional NMR imaging of a hazardous waste/cement sample is tested for the determination of the pore structure connectivity pattern and the observation of waste leaching; (4) NMR hole–burning spectroscopy is attempted for the study of the microscopic motions of waste in the cement matrix. These NMR techniques give information on the microscopic waste/cement interactions while providing a nondestructive evaluation of the quality of S/S process much superior to the destructive techniques such as leaching.

CHAPTER 1

INTRODUCTION

The hazardous waste disposal problem is a major national concern. Due to the extremely large amounts of toxic chemicals that are being released into the environment, the Federal government has been forced to regulate the disposal and management of hazardous wastes. The Environmental Protection Agency (EPA) classifies a waste as hazardous if it is non–degradable, toxic, may cause detrimental cumulative effects and poses a substantial threat to human health or living organisms. Some wastes are recycled, detoxified, or incinerated which decreases the amount of wastes that must be disposed, but in almost all cases some residue still remains. One of the most cost effective methods available for disposing of this residue along with other wastes, not recycled or incinerated, is to place it in landfills. The 1984 Amendments of the Hazardous and Solid Wastes Act (*1*) to the Resource Conservation and Recovery Act (RCRA) (*2*) banned the placement of non–containerized liquids in landfills. As a result, it is often necessary that some form of stabilization and/or solidification pretreatment be performed prior to landfilling. The process of solidification/stabilization (S/S) is a recommended treatment alternative for many RCRA wastes (*3*). It is estimated that 16 million metric tons per year of waste are candidates for S/S treatment and landfilling (*4*).

Stabilization is the process whereby the hazardous potential of the waste is treated in ways to reduce its toxicity and to convert the waste into chemical forms that are more resistant to leaching into the environment. The mechanism may be chemical bonding or physical entrapment. Solidification is the technique in which

solidifying agents are mixed with liquid hazardous wastes or sludge to bring the waste into a solid state that will allow landfilling. It implies no chemical interaction between the waste and binding agent (*5*).

There are a number of S/S processes used for waste disposal such as pozzolanic (cement, lime), thermoplastic, organic polymers, surface encapsulation, and glassification (*6*). The bulk of solidified/stabilized wastes in both radioactive waste and hazardous waste disposal consists of cementitious waste forms because cementitious materials are the least expensive (*4*). Selected materials such as portland cement, fly ash, pozzolan, lime, etc. are used in the S/S process for binding the hazardous waste prior to landfilling.

In practice, because of the fact that cementitious materials are relatively inexpensive, and the technology required to mix and place the solidified product is relatively simple, there is a strong tendency to use S/S for the treatment of hazardous wastes where it might not be appropriate. Solidification/stabilization technology is currently being utilized in the United States to treat inorganic, organic, and radioactive waste generated from industrial processes today and in the past (Superfund sites). According to the Toxic Release Inventory for 1990, 440 million pounds of toxic wastes were disposed in landfills in 1990 (*7*). Approximately 40% of all wastes that are disposed in landfills are pretreated by S/S processes. Solidification/stabilization of hazardous wastes is a widely used technology, therefore, it is very crucial to be able to evaluate its effectiveness and to make attempts to improve the technique. Significant questions remain about the range of its applicability, and if the process is adversely affected by multiple wastes. The chemical interactions between waste and fixing agents used in the S/S process has not been well understood.

Hazardous waste as aqueous solutions are isolated from the environment by placing them into cement–based waste containment systems where there are several possible results: the waste is encapsulated within the cement matrix with no chemical bonding; the waste reacts with the cement matrix to yield a solid product incorporated in the cement matrix; or the waste reacts with the matrix, but the product remains fluid and is encapsulated within the cement matrix. The more desired mechanism is a chemical reaction that takes place between the fixing agent and the hazardous constituent of the waste which results in detoxification of the waste or transformation of the waste into a form less accessible to leaching. Consequently, the waste is maintained in the solidified matrix and the possibility of environmental contamination is eliminated.

Solidification/stabilization technology has been known for a long period of time, but since its beginning, S/S has been dominated by the engineering disciplines. These engineering disciplines tend to stress the physical aspects of waste treatment such as compressive strength, permeability, and resistance to weathering. Physical properties by themselves are not very meaningful as performance indicators for hazardous wastes disposal of in landfills. The physical and chemical changes that take place as a result of the interaction of waste with cement have not been fully characterized. All the fundamental mechanisms involved in solidifying waste into cementitious waste forms are not known yet, and much remains to be done before one can design a waste S/S process for a given waste, from fundamental principles, or predict performance over decades and centuries with confidence. This is hardly surprising, since the fundamental mechanism of the chemistry and microstructure of cement pastes are still not completely known with confidence, and they have been studied for over 100 years. It is not easy to determine the fate of waste contaminants in a complex environment

such as cement. Certainly, it is much easier to test some overall property such as leach resistance than to prove the fundamental mechanisms of immobilization and leaching.

There are a number of techniques used to obtain chemical information about the effects waste additives have upon the cement matrix itself. While this information is very important for both understanding and improving the performance of S/S technology, it only gives information on macroscopic waste transport. Currently, EPA testing procedures rely heavily on leaching studies. The tests give the mean concentration of the contaminant released regardless of their original distribution, which may be quite heterogeneous among a variety of solid phases. Many leaching tests are batch procedures which give only a spatial mean concentration of release or the total concentration over leaching time (*4*). While leaching tests have merit, the macroscopic character of the test makes it difficult to intelligently improve the cement composition. Current understanding of S/S of waste cannot design waste S/S processes or predict durability with confidence. Hence the critical need for analytical techniques that probe the microscopic waste/cement structure.

It is believed that the wide range of waste research, development and quality control problems can only be solved by a technique or techniques which probes the composition, surface, or internal structure of a material with high spatial resolution and elemental or molecular sensitivity. Until recently limited research efforts were focused on the microscopic characterization of waste that has been solidified/stabilized. The inadequacy of our analytical tools, as well as the complexity of the cement hydration process has slowed progress in gaining a complete understanding of cement chemistry. Now, mix this with the mutual chemical and physical interactions occurring with the abundant chemistry of hazardous waste and an extremely challenging problem arises of finding out where

the hazardous substance is located in the cement matrix. A waste chemical component may chemisorb, precipitate, form a surface compound to any of several cement component surfaces, form inclusions or be chemically incorporated into the cement structure, or have simultaneous occurrence of several of these situations. Over the last 10 years, there has been a small group of researchers doing experiments directed towards understanding the basic chemistry of the process, including reactions that waste materials undergo during S/S conditions, and effects of waste on the chemistry and microstructure of the binder matrix. This research has been done using modern surface analysis techniques (x–ray photoelectron spectroscopy, auger electron spectroscopy, etc.), physical/bulk characterization techniques (scanning electron microscopy, x–ray diffraction, etc.), and optical molecular spectroscopy (FTIR, solid–state NMR, etc.). While these techniques can be useful in revealing the chemistry and leaching mechanisms of cementitious materials, they do not address the matter of microscopic motions of the waste. Clearly, this is relevant to an evaluation of the reliability of the S/S process for a particular waste and to get a better understanding of the S/S process, in order that S/S can be applied intelligently, and one can rationally design improved technology.

As mentioned previously, NMR has been used as a method for characterizing the matrix and the chemical forms of wastes, but its potential as a routine diagnostic tool has been largely untouched. Some crucial questions that need to be addressed about solid wastes, both before and after S/S treatment are the following:

1) What is the chemical form of the waste and the containing matrix?
2) To what extent are the waste molecules loosely or tightly bound to the cement?

3) Are there microscopic droplets of waste entrapped in the cement? If so, how big are the waste droplets?
4) Is there microscopic and long range mobility of the wastes through pores in the matrix?

NMR is uniquely capable of addressing these questions. The present research is exploratory in the sense that it will begin to answer these questions, but obviously there is a great deal more research that needs to be done before all of these questions are fully answered.

The specific aim of this research is to develop efficient methods for characterizing waste in cement on a microscopic scale. Chapter 4 describes the technique of solid–state deuterium NMR spectroscopy. This technique is used to determine if a particular deuterated organic waste is effectively solidified/stabilized and to determine the lower limit of the bond strength between the waste and the cement matrix. Chapter 5 details the bounded diffusion pulsed field gradient ^{1}H NMR spectroscopy experiment. This NMR–based procedure is tested on a liquid waste encapsulated within a solidified matrix to determine if droplets of liquid waste are entrapped within a solidified matrix. This technique yields a size distribution image of vesicles containing fluids, and measures the diffusion rate of organic material in solid matrices. Chapter 6 contains a demonstration of 3–D NMR imaging of a hazardous waste/cement sample. This method is tested for the determination of the pore structure connectivity pattern and the observation of waste leaching. Chapter 7 describes the NMR spectroscopy technique of "hole–burning". This method is attempted for the study of the microscopic motions of waste in the cement matrix. Chapter 8 contains results of ^{13}C NMR experiments that show the chemical form and state of phenol solidified/stabilized in cement.

CHAPTER 2

SHORT BACKGROUND OF PHENOL IN CEMENT

The bulk of this research was performed using phenol as a model waste to develop these new NMR–based procedures for studying waste/cement interactions. Phenol is water soluble and representative of organic wastes that are found in organic–inorganic mixed waste systems. It has a functional group that can react under the basic aqueous conditions that exist during cement matrix formation. Presumably for maximum immobilization, one would desire deprotonation of the alcohol function and formation of a rigid, insoluble material with tight binding between the phenoxide anion and the cations of the cement matrix.

Since phenols are common constituents of aqueous waste streams, there have been a number of studies of S/S using phenols as model wastes (*8-15*). Most of these centered on leachability of the phenol from the matrix, and for cement–stabilized phenols, leaching procedures such as the EP Tox or toxicity characteristic leaching procedure (TCLP) show very high percent recovery, and equilibrium leaching procedures afford large leachability indices (*8-10,12*).

Indeed, there is a substantial history of studies of interactions of phenol (PhOH) with cement. It has been assumed in cement literature that PhOH is converted to calcium phenoxide on contact with cement clinker. Interestingly, a qualitative test for the presence of free lime in clinker involves treatment with PhOH in nitrobenzene and water and microscopic observation of the characteristic long needles of "calcium phenoxide" (*16*). Phenol and mono–substituted phenols typically have pK_a's in the range 9–11, and the pH of pore waters in cements is

very basic, up to about pH 13. Consequently, the potential for conversion of phenols to their anions exists, but the extent of conversion may depend upon a number of factors controlling the acidity of the phenol and the basicity of the pore waters. The cation present in overwhelming amount is Ca^{2+}, consequently a Ca phenoxide would be expected. It has recently been shown (*17*) that combination of equimolar quantities of $Ca(OH)_2$ and PhOH produces PhOCaOH, not $(PhO)_2Ca$, and the latter can only be formed under forcing conditions with continuous removal of water.

There has been previous work that investigated several substituted phenols with respect to both leachability and chemical and physical properties. The following results have been obtained with samples prepared with normal portland cement (Type I cement; has a high Fe content, ca. 1–5% Fe_2O_3) using a 0.5 water–to–cement ratio by weight and containing 10% by weight of the organic. In the presence of 10% *p*–chlorophenol (*p*CP), setting times are approximately doubled, compared to cement alone, and strength is slower to develop (*18*). However, the 28–day compressive strength is the same as that of the cement paste without *p*CP. The effects of *p*–bromophenol (*p*BP) are similar, but setting is slightly slower and the 28–day compressive strength is about 10% lower. These samples have also been investigated using scanning electron microscopy (SEM) and X–ray diffraction (XRD) (*11*). SEM and XRD do show matrix changes with increasing proportions of organic. There is decreasing crystallinity, as judged qualitatively from SEM and from the increasing background noise relative to sharp peaks in the XRD patterns. Nevertheless, even at 20% by weight phenol, both transmission electron microscopy (*20*) and XRD (*11,21*) show $Ca(OH)_2$ to still be present in the matrix. XRD shows increased occurrence of new sharp peaks not present in cement alone. Comparison of XRD patterns of phenol–containing

cements with those of Ca salts of phenols prepared separately shows peak coincidences, but enough of the salt peaks are obscured by noise or overlapping strong cement peaks that it is not possible to positively identify the salts in the phenol–cement mixture by XRD alone (*11*). Scanning electron microscope results show that phenol in cement creates readily observable spherical vesicles in the cement matrix with diameters up to 1 mm (*22*). From these results one would suspect that the vesicles contain phenoxide salt dissolved in pore water.

It is possible to distinguish ionized from nonionized phenol by solid–state ^{13}C NMR, since the *ipso*–carbon of the aromatic ring shifts upfield by about 8 ppm in either PhOCaOH or $(PhO)_2Ca$ compared to PhOH (*17*). In our samples at 10% loading in Type I portland cement, PhOH is completely ionized (although some combinations of substituted phenols, cement and metal salts do show both ionized and nonionized phenol (*14*)).

Thus, there is considerable evidence for phenol–cement interactions, despite the fact that phenol is only poorly immobilized toward water leaching. In order to obtain more detailed information about the environment of the phenol in the cement matrix, we have developed new techniques using solid–state NMR spectroscopy to study waste/cement interactions.

CHAPTER 3

NUCLEAR MAGNETIC RESONANCE SPECTROSCOPY

3.1. Introduction

Nuclear magnetic resonance (NMR) spectroscopy involves the interaction of radio–frequency electromagnetic radiation with a collection of spinning nuclei immersed in a strong magnetic field. These nuclei are parts of atoms, which, in turn are assembled into molecules. NMR spectroscopy is the most important spectroscopic method for obtaining detailed information about molecular structure of low molecular weight compounds, polymers, and macromolecules. NMR spectroscopy has been used for decades to study the chemistry of various NMR active nuclei. It is applied across many areas such as organic, inorganic, organometallic, biological, and medicinal chemistry. NMR spectroscopy has many other applications in which it is used such as biosynthetic studies, chemical dynamics, and in live organ and whole body imaging.

3.2. NMR Phenomenon

Because the nucleus has a mass and that mass is in motion (spinning), the nucleus has spin angular momentum. Since the nucleus has an electrical charge and any electrical charge in motion sets up a magnetic field, the nucleus has a magnetic moment, μ, associated with it. Only nuclei that have spin number, I, not equal to zero will possess a magnetic moment and be NMR detectable. This magnetic moment has only certain possible spin orientations:

$$\text{number of states} = 2I + 1 \qquad (3.1)$$

where I is the spin number of the nucleus. Each of these states has its own spin quantum number, m, in the range m = I, (I – 1), (I – 2)..., –I. These orientations are degenerate (i.e., have the same energy) in the absence of an external magnetic field. However, when a collection of these nuclei is immersed in a magnetic field, the spin orientations are no longer degenerate. They separate in energy, with the largest positive m value corresponding to the lowest energy (most stable) state. This separation of orientations in a magnetic field is referred to as the nuclear Zeeman effect. The energy of a given spin orientation, E_i, is as follows:

$$E_i = -m_i H_o \frac{\gamma h}{2\pi} \qquad (3.2)$$

where m_i – spin quantum number;

H_o – applied magnetic field;

γ – gyromagnetic ratio;

h – Plank's constant.

3.3. Precession and the Larmor Frequency

Nuclei with $I \neq 0$ will have certain spin orientations when immersed in a magnetic field, each with a different energy. In these energy levels the nucleus is spinning about an axis of rotation creating a magnetic moment. This magnetic moment also rotates in a circular manner around the axis of the applied field. This rotation is called precession. The magnetic moment of a spinning nucleus precesses with a characteristic angular frequency called the Larmor frequency, ω,

$$\omega = \gamma H_o = 2\pi\nu \qquad (3.3)$$

where ν is the precession frequency expressed in hertz. Equation 3.3 is the Larmor

equation, which is the basis of NMR for the direct relationship between the precession frequency, ν, and the applied magnetic field, H_o.

3.4. Boltzmann Distribution

At thermal equilibrium, there will always be more spins in the lower energy state(s) than in the upper state(s). The ratio of the number of spins at the lower energy state and the number of spins at the higher energy state would reach a relationship according to the Boltzmann distribution equation:

$$\frac{N_U}{N_L} = e^{\frac{-\Delta E}{kT}} \qquad (3.4)$$

where N_U – number of spins in upper state;

N_L – number of spins in lower state;

ΔE – energy difference between the two state;

k – Boltzmann's constant;

T – absolute temperature.

At room temperature, the difference in population of the two states is exceedingly small, on the order of a few parts per million. This small difference in population accounts for part of the reason NMR has a relatively low sensitivity compared to other absorption techniques. However, sensitivity can be increased by changing anything that increases the population difference such as lowering temperature or using a higher applied field. It is the population difference that gives rise to a net magnetization and is sufficient to generate an NMR signal. There must be more spins in the lower–energy state than the higher one for net absorption of radiation to occur. If the two populations happen to be equal, no net absorption is possible, a condition called saturation.

3.5. NMR Signal

Before irradiation, if a species (such as a proton I = 1/2) is placed within a magnetic field, nuclei will align in both spin states precessing with characteristic frequency, but they are completely out of phase, i.e., randomly oriented around the z axis. According to Boltzmann's distribution, there will be a net magnetization, **M** – vector sum of all the nuclear magnetic moments. This **M** will be aligned statically along the z axis (magnetic field direction) with no component in the x,y plane. If the equilibrium system is disturbed by applying a radiofrequency field, H_1, perpendicular to the magnetic field at the Larmor frequency, the input energy will be absorbed by some of the nuclei which are at the lower energy level and these nuclei will jump to the higher energy state. The absorption of the energy gives rise to the NMR signal. All of the individual nuclear magnetic moments become phase coherent and track the H_1 of the radiation. This phase coherence forces **M** to precess around the z axis with the characteristic Larmor frequency. As such, **M** has a component in the x,y plane ($\mathbf{M}_{x,y}$) also oscillating with the same frequency. The strength and duration of the H_1 electromagnetic irradiation will determine the tip angle,θ, that **M** makes with the z axis which controls the magnitude of $\mathbf{M}_{x,y}$.

$$\mathbf{M}_{x,y} = \mathbf{M}\sin\theta \qquad (3.5)$$

3.6. Relaxation Process

Once an NMR signal is obtained, the equilibrium Boltzmann distribution is destroyed. The system must be able to return some way to the equilibrium state, otherwise the spin system will become saturated. The process of the excited nucleus losing its energy of excitation and returning to the unexcited state is called relaxation. The relaxation process is usually exponential and can be described by a relaxation time. There are two principal modes of relaxation which are spin–lattice and spin–spin relaxation.

3.6.1. Spin–Lattice Relaxation

The first is the spin–lattice relaxation process called T_1. During this process nuclei lose their excess magnetic energy as thermal energy to the lattice. The thermal energy is defined as translational and rotational energy. T_1 involves the return, after irradiation, of the nuclei to a Boltzmann distribution. For crystalline solids, T_1 values are much longer than that for liquids or solutions. The exact relationship of T_1 is as follows:

$$M_z(\tau) = M_z^{eq} (1 - e^{\frac{-\tau}{T_1}}) \qquad (3.6)$$

where $M_z(\tau)$ is the magnetization at time τ, and M_z^{eq} is magnetization at equilibrium, $\tau = 0$.

3.6.2. Spin–Spin Relaxation

After irradiation ceases, not only do the population states revert to a Boltzmann distribution, but also the individual nuclear magnetic moments begin to lose their phase coherence and return to a random arrangement around the z axis. This

process is called spin–spin relaxation, T_2. A nucleus in the upper energy state can transfer its energy to a neighboring nucleus in a lower energy state by a mutual exchange of spin. The most important feature of T_2 is that it determines the natural width of the line in the spectrum,

$$\nu_{1/2} = \frac{1}{\pi T_2} \tag{3.7}$$

where $\nu_{1/2}$ is the full width at half maximum of the spectrum. Usually, T_2 is considerably shorter than T_1.

3.6.3. Paramagnetic Relaxation

The presence of unpaired electrons can induce a very powerful relaxation mechanism within a sample. The γ of an electron is about 1833 times larger than that of a proton; therefore, paramagnetic impurities such as Fe^{3+}, dissolved oxygen, etc. can significantly shorten the relaxation times in a sample.

3.7. Solid–State NMR Spectroscopy

3.7.1. Cross–Polarization / Magic Angle Spinning

Most studies using NMR have been confined to pure liquids or solutions because until the early 1980's attempts to examine solid–state samples by NMR usually gave low–resolution spectra with such horrendously broad lines that little useful information could be derived from them.

There are several reasons why it is difficult to produce the same high–resolution spectra as for solid samples as for liquids. Most local anisotropic effects in solutions are averaged out by dynamic processes such as rotation. In solids, these processes are greatly retarded or stopped altogether thereby losing

their averaging effects. Thus, in solid samples there is a range of orientations with respect to the applied magnetic field, leading to a range of chemical shifts for each nuclear site and hence to broad lines. This effect is known as chemical–shift anisotropy. NMR signals in solids are broadened also by unaveraged magnetic dipole–dipole interactions through space. Another major problem is that spin–lattice relaxation is very inefficient in solids leading to long T_1 values and long relaxation delays that amount to unacceptably long spectrum–accumulation periods.

In the last 15 years, solid–state NMR has seen the development of methods that can overcome the problems associated with solids and yield high–resolution spectra comparable to those obtained for liquid systems. One such technique that overcomes these problems is cross–polarization/magic angle spinning (CP/MAS). This technique averages out many of the anisotropic effects while overcoming the effects of slow relaxation.

3.7.1.1. Cross–Polarization (CP)

In solids, molecular motion is limited and this leads to very inefficient spin–lattice relaxation. Slow relaxation times in solids can be overcome by a technique known as cross–polarization. This technique takes advantage of the fact that proton spin diffusion generally causes all of the protons in a solid to have the same short T_1 compared to carbon T_1 (note: the common case of CP from protons to carbons will be discussed, but these concepts apply to polarization between other spins as well). The abundant hydrogens are irradiated with a powerful decoupling field, and their resulting polarization is transferred to the nearby, but less abundant ^{13}C nuclei. This procedure was demonstrated by Hartmann and Hahn in 1962 (*23*). The Hartmann–Hahn condition is obtained when the energy transfer between nuclei with widely differing Larmor frequencies is made to occur by

meeting the condition of the following equation.

$$\gamma_C H_{1C} = \gamma_H H_{1H} \tag{3.8}$$

Because of the fact that γ_H is four times γ_C, the Hartmann–Hahn condition occurs when the strength of the applied carbon field, H_{1C}, is four times the strength of the applied proton field H_{1H}. When the proton and carbon rotating frame energy levels match, polarization is transferred from the abundant protons to the rare carbon 13 nucleus. Since polarization is being transferred from protons to carbons, the shorter T_1 of the protons dictates the repetition rate for signal averaging thereby accounting for the effectiveness of this technique.

3.7.1.2. Magic Angle Spinning (MAS)

The energy, E, associated with the interaction between two magnetic dipoles is as follows:

$$E = \frac{\gamma^2(1 - 3\cos^2\theta)}{r^3} \tag{3.9}$$

where θ is the angle the pair of dipoles makes with the applied magnetic field. The rapid rotation of molecules in liquid samples averages this energy to zero, while a solid sample must be rapidly spun around an axis that is 54.7° (magic angle) with the applied magnetic field to average this interaction energy to zero. The net result is spectral lines that are sharpened considerably which allow valuable information to be obtained from solids. The rate of rotation around this magic axis must be greater than the frequency of the dipole–dipole interaction, typically 4000–5000 Hz.

3.7.2 Solid–State Deuterium NMR Spectroscopy

The deuterium nucleus has a few disadvantages compared to other common nuclei studied by NMR spectroscopy. It has a low natural abundance, low gyromagnetic ratio, and a spin of 1. These disadvantages of the the ^2H nucleus can be used to give information on the details of molecular motions in solids, something that the other nuclei cannot do.

Due to the fact that ^2H has a low natural abundance, it must be specifically labeled to observe its solid–state NMR signal. The nice thing about this is that once labeled, the marked site affords a very high degree of selectivity. Since the ^2H nucleus has a spin of 1, in the presence of a magnetic field it has three quantized energy levels: +1, 0, and –1. Deuterium is quadrupolar, therefore has a nonspherical charge distribution at the nucleus. A substantial perturbation of the Zeeman energy levels occurs because of the interaction of the quadrupole moment with the electric field gradient tensor at the nucleus.

In most solid–state deuterium NMR spectroscopy of static systems, i.e., a reorientation rate slower than about 10^3 s^{-1}, there are four factors that determine the deuterium NMR transition frequencies: the Larmor frequency, the quadrupolar coupling constant, the asymmetry parameter, and the angle between the z–axis of the electric field gradient and the applied magnetic field, H_0 (*24*). The deuterium line shape is symmetric about the Larmor frequency and is composed of two sets of spin state transitions, $|+1\rangle \rightarrow |0\rangle$ and $|0\rangle \rightarrow |-1\rangle$. As shown in Figure 3.1 for a quadrupole coupling constant of +175 kHz and an asymmetry parameter of zero, the $|0\rangle \rightarrow |-1\rangle$ transition varies from an offset frequency of –65 kHz to +131 kHz. The transition at +131 kHz corresponds to the z–axis of the electric field gradient aligned with the applied magnetic field ($\theta = 0°$); –65 kHz corresponds to the perpendicular orientation, $\theta = 90°$, and is more intense due to a sin (θ) weighting

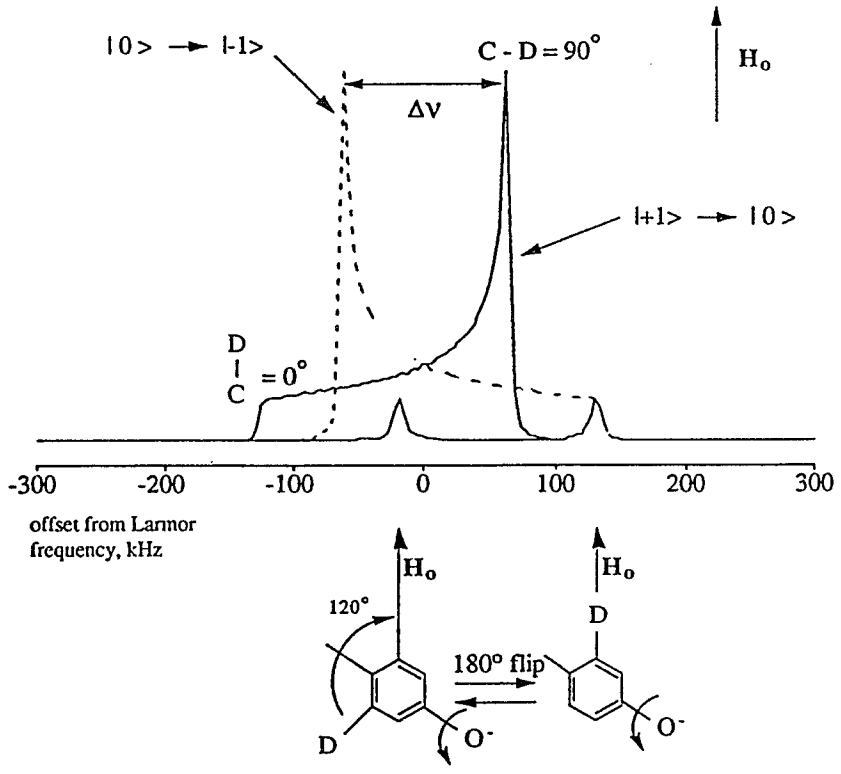

Figure 3.1 Details of a solid–state deuterium NMR spectrum showing how 180° ring flips can average portions of the deuterium NMR spectrum. Here, $e^2qQ/h = +175$ kHz and $\eta = 0$.

factor. For a C–D bond, the electric field gradient z–axis is roughly aligned with the C–D bond vector, hence the labeling in Figure 3.1.

The quadrupole coupling constant determines the width of the line shape and can be obtained from the frequency separation between two sets of transitions at the same angle, θ,

$$\Delta\nu = \frac{3}{4}\left(\frac{e^2 q_{zz} Q}{h}\right)\left(3\cos^2\theta - 1\right) \qquad (3.10)$$

where $e^2q_{zz}Q/h$ is the quadrupole coupling constant, typically about 175 kHz (we assume that the asymmetry parameter is near zero) (*25*). Hence, for a static, C–D site, one expects a frequency separation between the peaks of the line shape (θ = 90°) of $\Delta\nu$ = (3/4) 175 kHz = 131 kHz, as shown in Figure 3.1.

If there is motion on a time scale faster than that defined by the separation between the rf pulse of the quadrupolar echo sequence, then one obtains an average of transition frequencies. However, the mode of motion affects the averaging process. Shown in Figure 3.1 is a single deuteron in phenol at two different orientations. When the C–D bond is aligned with H_o, the $|0\rangle \rightarrow |-1\rangle$ transition frequency is +131 kHz. When the phenyl ring executes a 180° flip about the axis shown, the orientation of the C–D bond with respect to the magnetic field changes. Now, θ = 120° and a different $|0\rangle \rightarrow |-1\rangle$ transition frequency is expected, about –16 kHz, as shown in Figure 3.1. Since the reorientation rate is rapid, the observed transition becomes the average of the two. The calculation of the line shape now requires averaging over all possible orientations of the flipping axis as well as over initial orientations of the C–D bond vector.

Other factors which can affect the line shape include the relative population of sites (*26*) and reorientation rates that are comparable to the time scale defined by t_1 in the pulse sequence (*27*). In this work the mirror symmetry of the phenol

molecules will assure an even population of orientations. However, reorientation rates in the intermediate regime can occur. Thus, shown in Figure 3.2 are simulated line shapes (*28*) for a wide range of rates. It is important to note that there is a loss of spectral intensity in the intermediate exchange regime. The reason for this loss is the fact that the last pulse in the quadrupole echo pulse sequence does not completely refocus the magnetization evolution due to the irreversible jump dynamics (*29*). For exchange rates in either the fast or slow limits, the integrated area of the resonance is proportional to the number of deuterons. By comparing the line shapes of the simulated spectra to the fully relaxed experimental spectra, the mode and rate of motion can be determined for the motions in the intermediate exchange regime. Lastly, in the two regimes where the line shape is independent of rate, anisotropic spin–lattice relaxation times, T_1 ($\theta = 0°$) and T_1 ($\theta = 90°$) can be used to determine the reorientation rate (Appendix A.1), provided that the mode of motion is known (*30,31*).

3.7.3. Constant Time Pulsed Field Gradient Stimulated Echo (PFGSE) NMR Spectroscopy

Recently, a new pulsed field gradient stimulated echo pulse sequence for NMR spectroscopy, constant time PFGSE NMR, was developed to probe the size distribution of fluid–filled vesicles, a bounded diffusion experiment (*32*). This is a variation of the PFGSE NMR schemes for measuring molecular diffusion (*33-41*). In the bounded diffusion experiment, one follows the molecular diffusion of spin magnetization throughout the pores of a solid. A size distribution image of the vesicles containing fluid is generated, with a potential spatial resolution of 0.1 μm.

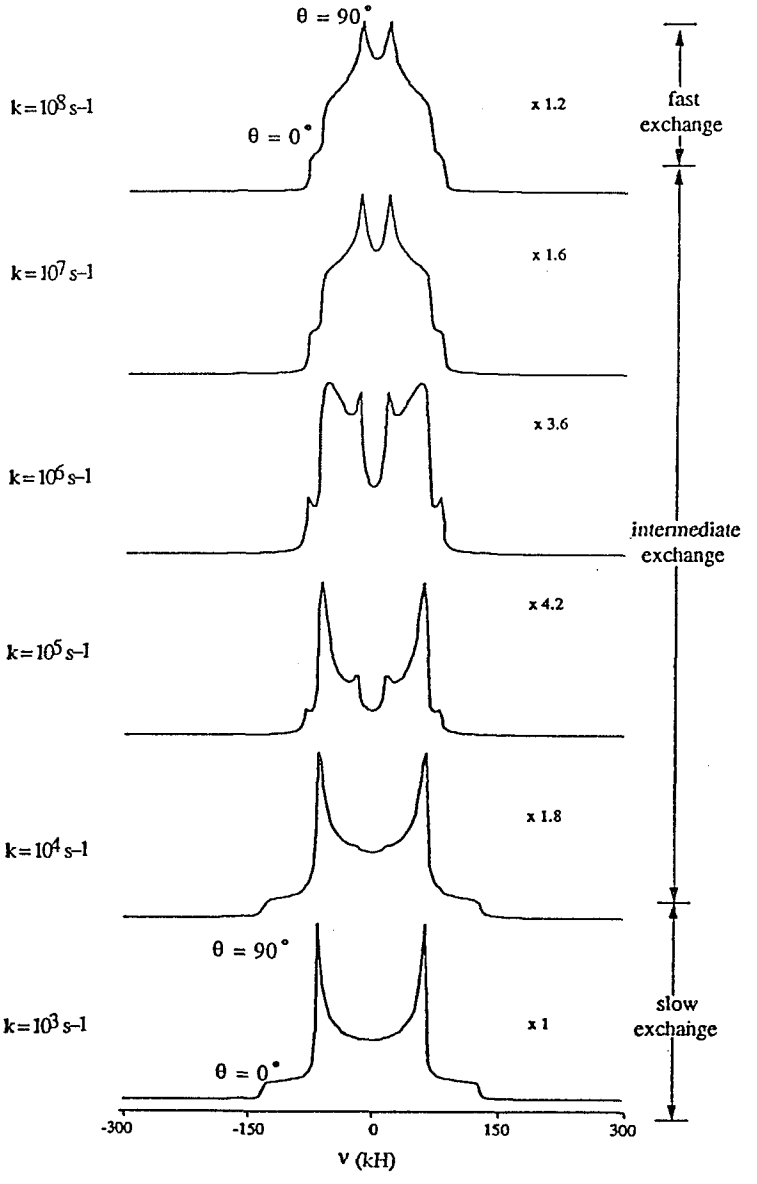

Figure 3.2 The simulated spectra for a quadrupole echo pulse sequence showing the effect of flip rate on the deuterium NMR lineshape for d_5–phenol rings executing 180° flips. Important parameters are as follows: ν_L = 30.7 MHz, 90° pulse length = 3 μs, delay between rf pulses = 25 μs, e2qQ/h = +175 kHz and $\eta = 0$. Spectra for the intermediate–exchange rates are vertically expanded by the factors shown in the figure.

The bounded diffusion experiment pulse sequence is shown in Figure 3.3. The 90° rf pulse tips the nuclear spin magnetization vector into the plane transverse to the applied magnetic field and its gradient. The gradient causes a distribution of precession frequencies that encodes the phases of spin vectors in the transverse plane during t_e, the encoding time. The gradient encodes the spins spatially as their local magnetic field is directly proportional to their coordinate along the applied magnetic field gradient. The second 90° rf pulse aligns the spin magnetization along the z axis so that the gradient has no effect on the spins while they are allowed to diffuse during t_d, the diffusion time. The third 90° rf pulse tips the spins magnetization vector again into the plane transverse to the applied magnetic field. Any spin translational diffusion that occurs during t_d will cause spin magnetization to refocus either earlier or later than those spins that do not diffuse, and this causes attenuation of the echo signal amplitude. If no spin translational diffusion occurs, then all spins will refocus to create an echo centered at time t_e after the last pulse. A series of experiments, 2^n, are done using a constant diffusion time. For each experiment the gradient level is held constant, but for each successive experiment the field gradient is incremented by a small, fixed amount equal to $1/2^n$ of the total gradient range.

The bounded diffusion experiment follows molecular diffusion of spin magnetization throughout the pores of a solid over a fixed time with increasing magnetic field gradient strength. The sample is assumed to be a liquid; therefore, magnetization displacements are associated solely with molecular displacements rather than spin diffusion (T_2 type processes).

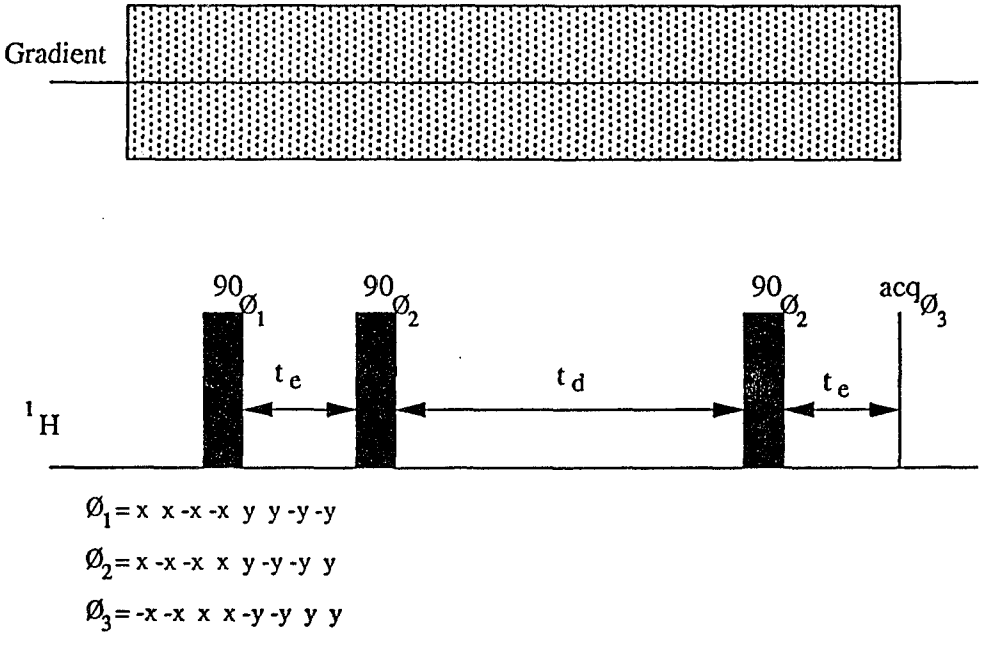

Figure 3.3 The bounded diffusion PFGSE experiment where t_e is encoding time and t_d is diffusion time.

The echo amplitude S(g) can be expressed in terms of an integral as follows (*32,42*):

$$S(\mathbf{g}) = \int \rho(\mathbf{r}_o) \int P(\mathbf{r}_o \mid \mathbf{r}, t_d)\exp[i\gamma t_e \mathbf{g}(\mathbf{r} - \mathbf{r}_o)]d\mathbf{r}d\mathbf{r}_o \qquad (3.11)$$

where $\rho(\mathbf{r}_o) \equiv$ initial concentration as a function of the initial position, r_o;

$P(\mathbf{r}_o \mid \mathbf{r}, t_d) \equiv$ probability that a spin initially at r_o will move to r within a time t_d;

$t_e \equiv$ encoding time;

$\mathbf{g} \equiv$ magnetic field gradient strength;

$\gamma \equiv$ gyromagnetic ratio; and

$\mathbf{r} - \mathbf{r}_o \equiv$ represents a possible spatial displacement during the diffusion time, t_d.

Equation 3.11 requires $t_e << t_d$.

The Fourier transform of the echo amplitude for the 2^n experiments becomes the diffusion displacement profile (*37,43*). The variables are relative displacement along the gradient direction, x, and the conjugate variable $4\gamma t_e \mathbf{g}$, with units of cm^{-1}. The diffusion displacement profile yields the distribution of spins along the field direction at the end of the diffusion time and can be examined for free or bounded diffusion. For free diffusion, the profile will broaden with increasing diffusion times, while for bounded diffusion, the profile will have a full width at half–maximum that remains constant. In the free diffusion case, there is a linear relationship between the full width at half maximum of the profile versus the square–root of the diffusion time. From the slope of this plot, the diffusion coefficient of a liquid can be extracted.

3.7.4. Three–Dimensional NMR Imaging

NMR imaging is a noninvasive technique that generates images of "slices" of a material. There are many techniques for obtaining an NMR image, but the basic concept consists of NMR imaging taking advantage of the direct proportionality between the nuclear magnetic resonance frequency and the applied field strength (*44-47*). By placing the sample within a linearly magnetic field gradient, the spatial distribution in the spin density along the gradient direction is mapped into a frequency distribution. By employing gradients that increase along each of the three cartesian axes, the three–dimensional variation in nuclear spin density, which is related to the elemental or molecular concentration, can be measured. Except for the data processing, NMR imaging is conceptually similar to the NMR diffusion experiments described above.

3.7.5. Hole–Burning NMR Spectroscopy

Chemical shift anisotropy produces inhomogeneous broadening of NMR lines in solids. This inhomogeneous line is composed of narrow isochromats (Figure 3.4), and each isochromat arises from molecules or functional groups being at certain orientations relative to the external magnetic field. By selectively saturating a frequency interval within this NMR line (*48, 97*), one saturates only spins on molecules or groups at particular physical orientations. Therefore, these orientations have been distinguished or "tagged". This tag is z magnetization and will only last the time of the spin–lattice relaxation time, T_1.

NMR frequency and orientation are connected through chemical shift anisotropy, therefore, any molecular reorientations which occur after the hole is burned will diffuse the hole through the line. In other words, spins that were in the saturated region may move to new frequencies, carrying their saturation with them;

while spins initially in the unsaturated region may move into the burned region, carrying their magnetization with them. As a result, while maintaining a constant integrated intensity of the line (ignoring for the moment the spin–lattice relaxation of the resonance), there is a redistribution of the magnetization through the line.

By examining the NMR line shape, the new frequency locations and hence the new orientations of the tagged spins can be determined. If there is no microscopic motion, the burned hole will remain the same shape, but there will be some change in the depth of the hole due to T_1 recovery (Figure 3.4). If there is microscopic motion of the spins, the burned hole will broaden as the diffusion time is increased (Figure 3.5).

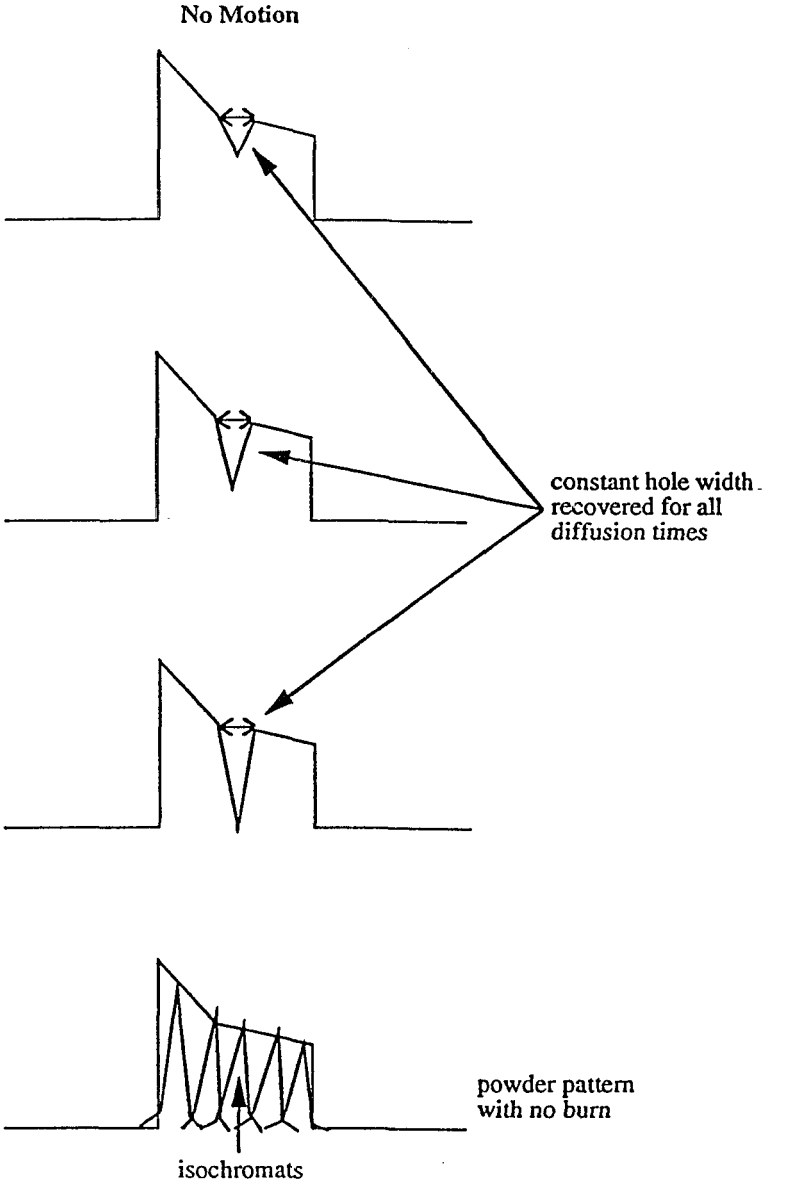

Figure 3.4 A scheme of no microscopic motion showing how the hole width remains constant at all diffusion times indicating no motion of the nuclei under investigation.

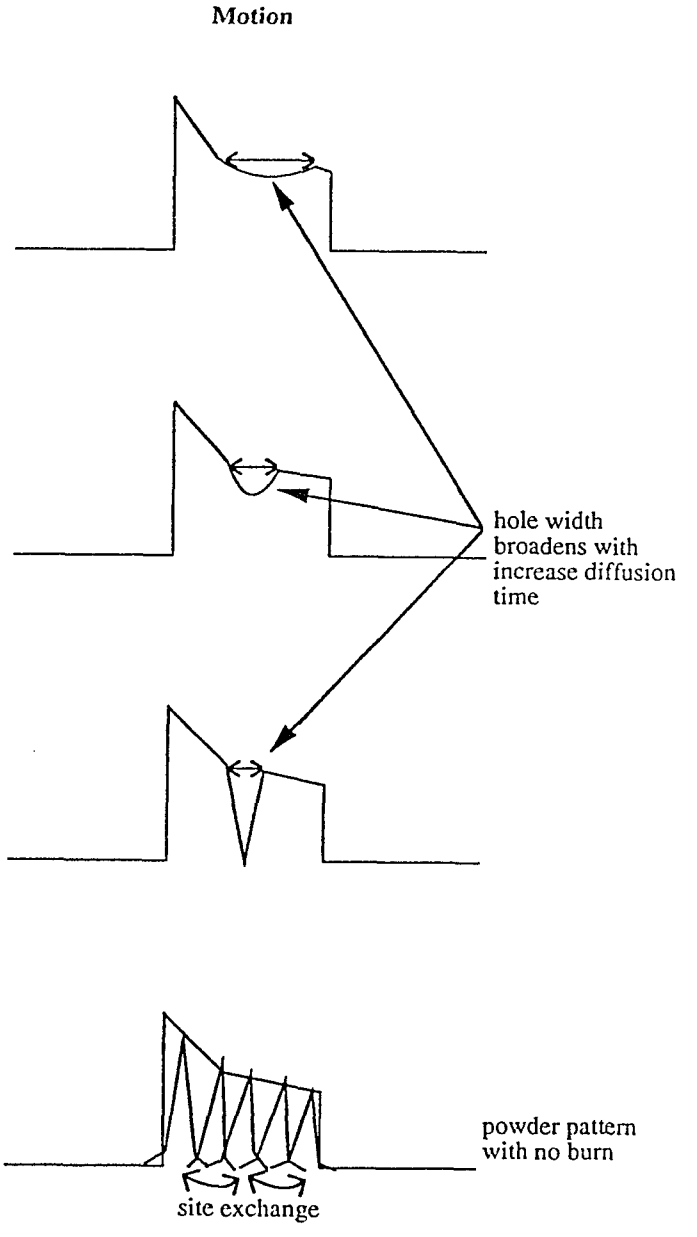

Figure 3.5 A scheme of microscopic motion showing how the hole width broadens with increasing diffusion times indicating motion of the nuclei under investigation.

CHAPTER 4

SOLID–STATE DEUTERIUM NMR SPECTROSCOPY

4.1. Introduction

Recently, solid–state ^{27}Al and ^{29}Si nuclear magnetic resonance (NMR) techniques have been used to monitor immobilization mechanisms in the solidification/stabilization of waste in portland cement (*19,49-51*). While these data have been useful for following the curing of waste/cement mixtures, they do not address the matter of microscopic motions of the waste. Our research has applied deuterium solid–state NMR techniques with the goal of addressing the following question: "For the case of low concentrations of organic waste in cement, are the waste molecules loosely or tightly bound to the cement matrix?" The answer to this question is very important in order to evaluate the reliability of the solidification/stabilization process for a particular waste.

In order to obtain more detailed information about the environment of waste solidified/stabilized in a cement matrix, we have applied solid–state deuterium NMR spectroscopy, which is an excellent probe for obtaining the details of molecular motions in solids. Based on a line shape analysis, reorientation modes, such as methyl group rotation, can be distinguished from 180° phenyl ring flips, and reorientation rates can be measured in the region of 10^3 to 10^6 s^{-1} (*52,53*). Based on T_1 measurements, reorientation rates from 10^6 s^{-1} to more than 10^{11} s^{-1} can be determined (*30,54,55*). Solid–state deuterium NMR spectroscopy has been frequently applied to various systems such as proteins, lipids, organometallics, and polymers (*30,52-56*).

Herein, we have applied solid–state deuterium NMR spectroscopy to the study of phenol/cement interactions. This is the first use of deuterium NMR spectroscopy to study waste solidification/stabilization (S/S). The main feature of deuterium NMR spectroscopy is the ability to monitor molecular reorientations over a wide range of reorientation rates. This technique allows one to determine if a particular deuterated organic waste is effectively solidified/stabilized and to determine the lower limit of the bond strength between the waste and the cement matrix. Two different phenol components were found, both a liquid–like component, presumably phenol dissolved in pore waters, and a rigid form, presumably solid calcium phenoxide. As the sample cures from one month to one year, the liquid–like component decreases, but still constitutes a significant fraction ($\approx$ 50%) of phenol at one year. After evaporation of the pore water from the cement matrix the ^2H line shape and T_1 were measured at 230 – 360 K; the maximum activation energy for the 180° ring flip process is 5.5 kcal/mol. Hence, the lower limit of the bond strength between phenol and the cement matrix is approximately 5.5 kcal/mol.

4.2. Experimental

4.2.1. Sample Preparation

Low iron content white portland cement (Lehigh Cement Company, Waco, TX), about 0.3% Fe_2O_3 by weight, was used to reduce the interference of paramagnetic relaxation upon the ^2H NMR spectra. d_5–Phenol *(98%)* was obtained from Cambridge Isotopes Laboratories. The procedure used to make the samples was as follows: All samples were prepared under a nitrogen atmosphere in order to reduce the formation of carbonates on the surface of the cement. To a phenol/cement mixture enough deionized water was added to yield a water/cement ratio of 0.5 by weight. The mixture was stirred in a borosilicate glass vial until

apparent homogeneity (ca. 2 minutes). Some samples were immediately transferred to 5 mm NMR glass tubes while others were allowed to solidify in the glass vials. The latter were broken out of the vials as needed, crushed with a mortar and pestle to a fine powder, then loaded into NMR tubes. In some cases, the crushed samples were reexamined at a later date.

There were three different loading percentages of waste in the cement: 10% phenol by weight relative to cement (1.0 g white cement, 0.1 g d_5–phenol, 0.5 mL deionized water); 1% phenol by weight (10.0 g, 0.1 g, 5 mL); and 0.1% phenol by weight (10.0 g, 0.01 g, 5 mL).

4.2.2. Solid–State Deuterium NMR Spectroscopy

Solid–state deuterium NMR spectra were acquired at 30.7 MHz on a Bruker MSL200 solid–state spectrometer. The basic pulse program was a quadrupole solid echo pulse sequence (*57,58*): $90_{x,-x} - t_1 - 90_y - t_2 - \text{acquire}_{x,-x}$. The 90° pulse length was 3.0 μs and t_1 was 25 μs; the second delay, t_2, was adjusted to the echo maximum. In order to cancel the effects of probe ringing, a two–step phase–cycling routine was used where the phase of the first rf pulse and the receiver phase were alternated between 0° and 180° (*59*). The relaxation delay between scans was 200 ms. A line broadening factor of 5000 Hz was used in exponential multiplication to improve the signal–to–noise ratio of the spectrum. Approximately 2000 to 4000 scans were averaged for each experiment.

Deuterium spin–lattice relaxation times were measured with the inversion recovery technique. The inversion recovery technique uses the quadrupole echo pulse sequence with a $[180°_x - \tau -]$ prior to the pulse sequence. The τ is a variable delay period and typically, 10 different τ delays were used. Experiments at different temperatures were done, but care was taken to adjust the relaxation delay

between scans to no less than five times the T_1 at the 90° orientation (see Fig. 3.1) at each temperature. This was done to assure that 99% of the magnetization was recovered before each scan. The T_1 values at the 90° orientation, T_1 (90°), were calculated by fitting (Simplex algorithm) the spectral intensity at the corresponding frequency, I, to the following equation:

$$I = I_0 [1 - A \exp^{-\tau / T_1}] \qquad (4.1)$$

where I_0, T_1, and A are the intensity at equilibrium, corresponding relaxation time, and measure of the efficiency of the 180° pulse which should have a value near 2 for the more nearly on–resonance 90° orientation.

For the purpose of accurate modeling of NMR line shape, spectra were transferred as binary data files from the Bruker Aspect–3000 computer to a Macintosh II computer via an RS–232 serial connection and the KERMIT file transfer protocol (*60,61*). A program (*62*) written in LabVIEW, a graphical programming language, (*63*) was used to convert the binary files to ASCII data files. The spectra were then fitted to a gaussian which represents the liquid–like component and a 180° ring flip simulation spectrum which represents the solid calcium phenoxide. The Levenberg–Marquardt nonlinear least–squares algorithm (*64,65*) was used to obtain the best fit. This program was written in Matlab v3.5f, a vector oriented programming language (*66,67*).

4.3. Results and Discussion

Spectra were acquired on pure d_5–phenol using the quadrupole solid echo pulse sequence at various temperatures and are shown in Figure 4.1. Figure 4.1a is the spectrum near the melting point of phenol at 41 °C and shows a single narrow resonance which indicates that d_5–phenol has liquid–like mobility. Near room

temperatures the line shape is broader, but the motion is more complicated than just 180° ring flips. Probably there is a combination of 180° ring flips and libration; similar spectra can be found for phenyl rings in polymers (*68*). At 250 K, a broad resonance is obtained which is nearly that of static phenyl rings or flip rates less than 10^4 s^{-1}.

At this point, we wish for the reader to note and remember three ^2H NMR line shapes: a) the narrow, simple peak for liquid phenol (Figure 4.1a); b) the broad resonance for solid phenol (Figure 4.1d); and c) the broad, but well–defined resonance of a phenyl ring constrained to move only by 180° flips about a C_2 axis (Figure 3.2, $k = 10^8 s^{-1}$). The last spectrum is the one that implies binding between the phenol waste and the cement matrix and, therefore, perhaps successful S/S. Observation of liquid phenol will certainly indicate that the phenol is able to move within the matrix on a microscopic scale (and probably also on a macroscopic scale).

Samples at 0.1, 1, and 10% d_5–phenol by weight in cement were studied at various temperatures. These samples were placed in NMR tubes upon mixing and allowed to cure for one month (cement matrix undisturbed). Representative spectra are shown in Figure 4.2. The dominant feature for all samples studied between 260 and 360 K is a liquid–like spectrum. The shoulders of the spectra (4.2b, 4.2c) at ± 65 kHz are evidence of deuterons executing 180° ring flips while the large spike in the middle indicates deuterons that have liquid–like mobility. At lower temperatures, say 230 K, a static line shape (4.2e) is observed and is similar to that obtained for pure d_5–phenol at 250 K. Even the 0.1% sample shows liquid–like and static line shapes similar to that for 10% sample at the corresponding temperature. The same samples were examined after one year of cure, and the spectra are very similar to those obtained at one month.

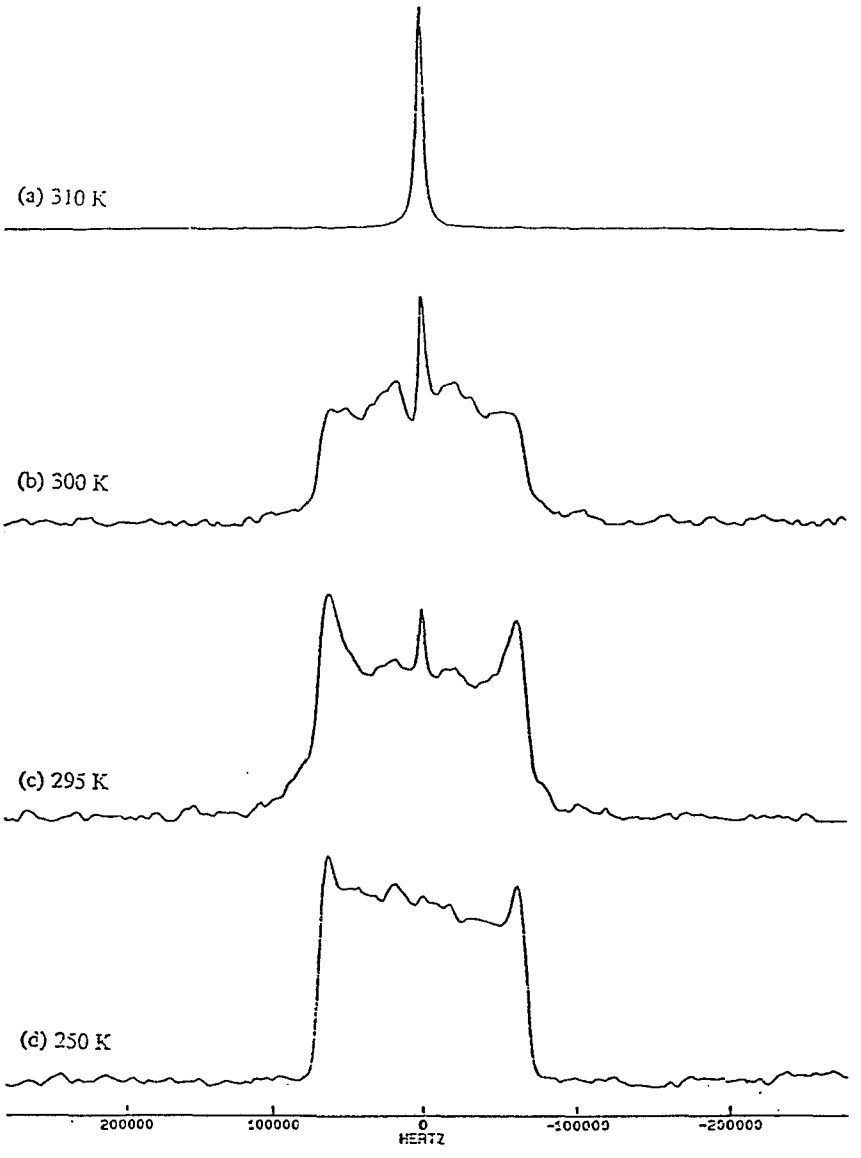

Figure 4.1 Deuterium NMR spectra for pure d_5–phenol. The line shape at 310 K indicates liquid–like mobility whereas the more complex line shape at the lower temperature shows restricted mobility. However, some motion is still present at 250 K.

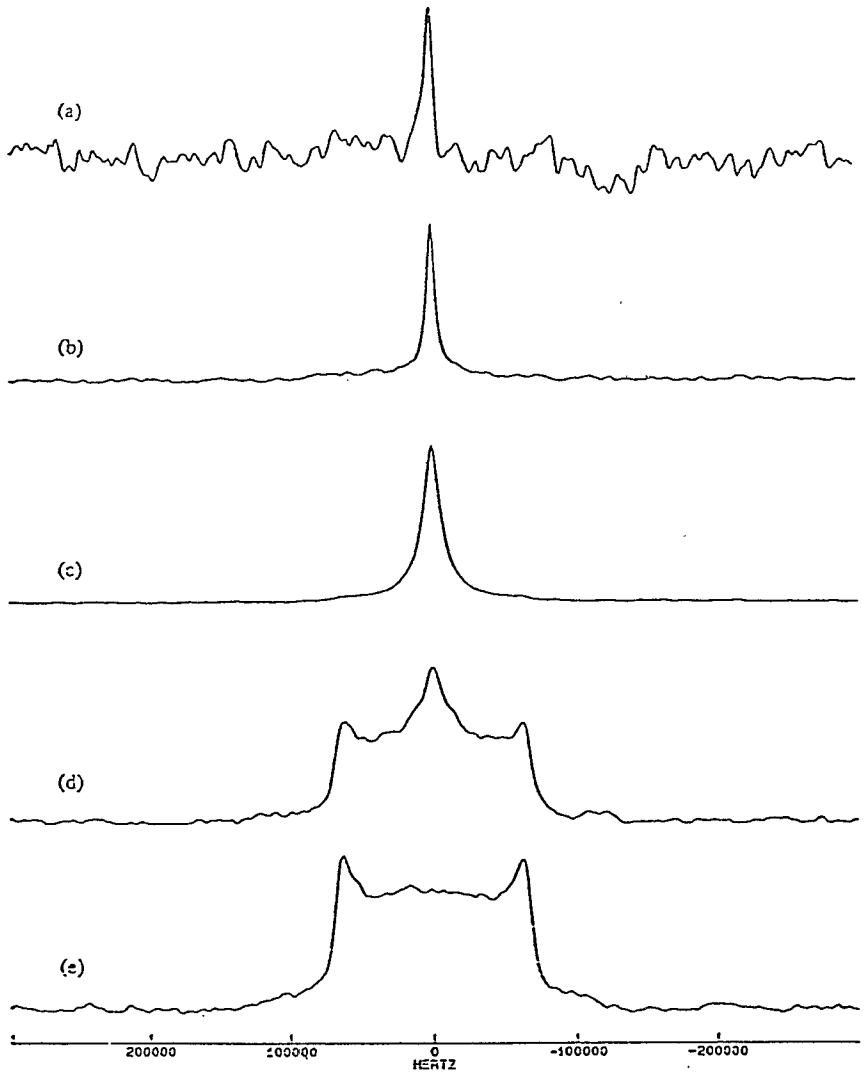

Figure 4.2 Deuterium NMR spectra for d_5–phenol in white portland cement cured in NMR tubes for one month: a) 0.1% phenol by wt., 293 K; b) 1% phenol by wt., 293 K; c) 10% phenol by wt., 293 K; d) 10% phenol by wt., 240 K; e) 10% phenol by wt., 230 K. Even at low loading, there is still liquid–like mobility for most of the phenol.

These results suggest that there are two different environments for phenol in cement and that these environments persist for a long time. One environment consists of the phenol in cement that has a mobility like liquid phenol and appears not to be bound to the cement matrix; we will refer to this component as the liquid–like component. This component probably consists of phenol present in cement pore water in ionized form. A second environment consists of the phenol in cement that is executing 180° ring flips; the constrained motion implies binding of the phenol through the hydroxy group. This more rigid form is presumably a calcium phenoxide salt and may or may not be bound to the cement matrix (precipitated Ca phenoxide salt or phenoxide bound to surface Ca). For simplicity, we will refer to this rigid form as solid calcium phenoxide. The most important result is the observation of liquid–like phenol, even after one year of cure. Clearly, S/S with portland cement has failed to immobilize phenol on a microscopic scale.

The NMR spectra were fitted to a simple model to determine what percentage of the phenol exists as liquid–like phenol and,therefore, not bound to the cement matrix (Appendix A.2.). The model consists of a simple gaussian representing the liquid–like phenol and the line shape corresponding to fast two–site jump motion (180° ring flips). The equation used for the fit is as follows:

$$g(\nu)=A^{liq}\exp\left[-\ln(2)\left(\frac{\nu}{\Delta\nu}\right)^2\right]+A^{2\text{-site}}\,g(2\text{-site})+\text{offset} \qquad (4.2)$$

where A^{liq} and A^{2-site} are the coefficients for the contribution for the liquid–like and two–site jump motion (Figure 3.2, $k = 10^8 s^{-1}$). The parameter $\Delta\nu$, the half–width at half–maximum, and the vertical offset are variables. The choice of the two–site line shape for $k = 10^8 s^{-1}$ is made on the basis of temperature independent line shapes and constant intensities, down to 260 K, implying that the jump rate for the two–site phenols is faster than $k = 10^8 s^{-1}$ at 300 K. The fit,

eq.4.2, includes only the line shape for the ortho and meta deuterons of the d_5–phenol. The deuteron bound to the para–carbon is aligned with the C_2 axis, therefore, this deuteron is not affected by the 180° flips. Even with rapid flipping, this deuteron should still show a static powder pattern (*69*). The line shape for the para deuterons, given by Figure 3.2 ($k = 10^3 s^{-1}$), was excluded based upon the conclusion that the ^2H T_1 is longer for this site compared to the other deuterium sites. Two observations lead to this conclusion: (1) The $k = 10^3 s^{-1}$ line shape was not observed in any tube samples. (2) A inversion–recovery experiment yielded two components in the resonance at ± 65 kHz; the larger component has a short T_1 (0.016 s) while the less abundant component has a T_1 of 0.32 s (*70*). Based on the longer T_1 and the smaller abundance, the smaller component is believed to be due to the para deuteron. Since all experiments done to measure the ratio of liquid–like to solid calcium phenoxide were done with a relaxation delay of 0.2 s, the interference of the para deuteron is partially eliminated. Table 4.1 contains a summary of all the results obtained by this fitting procedure and one example is shown in Figure 4.3 while the remainder are in Appendix B.1. For the 10% phenol in cement sample, the percent solid calcium phenoxide increased from 44 (2)% at one month solidified to 55 (2)% at one year. The fraction of solid calcium phenoxide continued to increase with additional cure time, Table 4.1. The 1% phenol in cement sample remains basically the same from one month to one year with approximately 46 (2)% being solid calcium phenoxide. These results suggest that for cure times up to one year approximately 50% of the phenol in cement has a mobility like a liquid and appears not to be bound to the cement matrix.

Because of the extremely basic aqueous solution in portland cement, pH≈12, and the weak acidity of phenol, $pK_a \approx 10$, most of the liquid–like phenol is probably dissolved as the phenoxide ion in the pore water of the cement matrix. We have

Table 4.1: Fraction of d_5-Phenol Bound to, or Precipitated in, Cement Matrix

wt. % phenol in white portland cement	cure time	χ^2_ν	solid calcium phenoxide (% phenol executing 180° flips)
1% in NMR tube[a]	1 month	0.82	45 (2)%
	1 year	0.95	48 (2)%
	14 month	1.2	52 (2)%
10% in NMR tube[a]	1 month	0.55	44 (2)%
	1 year	0.62	55 (2)%
	15 month	1.1	80 (2)%
10% crushed at 2 month[b] no oven treatment	2 month	0.85	55 (2)%
10% crushed at 2 month[b] oven treated at 2 month, 36 hr, 90°C	2 month	0.28	95 (3)%

[a] Sample prepared, then forced into 5 mm NMR tube and allowed to cure.

[b] Sample removed from vial, then crushed to fine powder,~ 100 mesh.

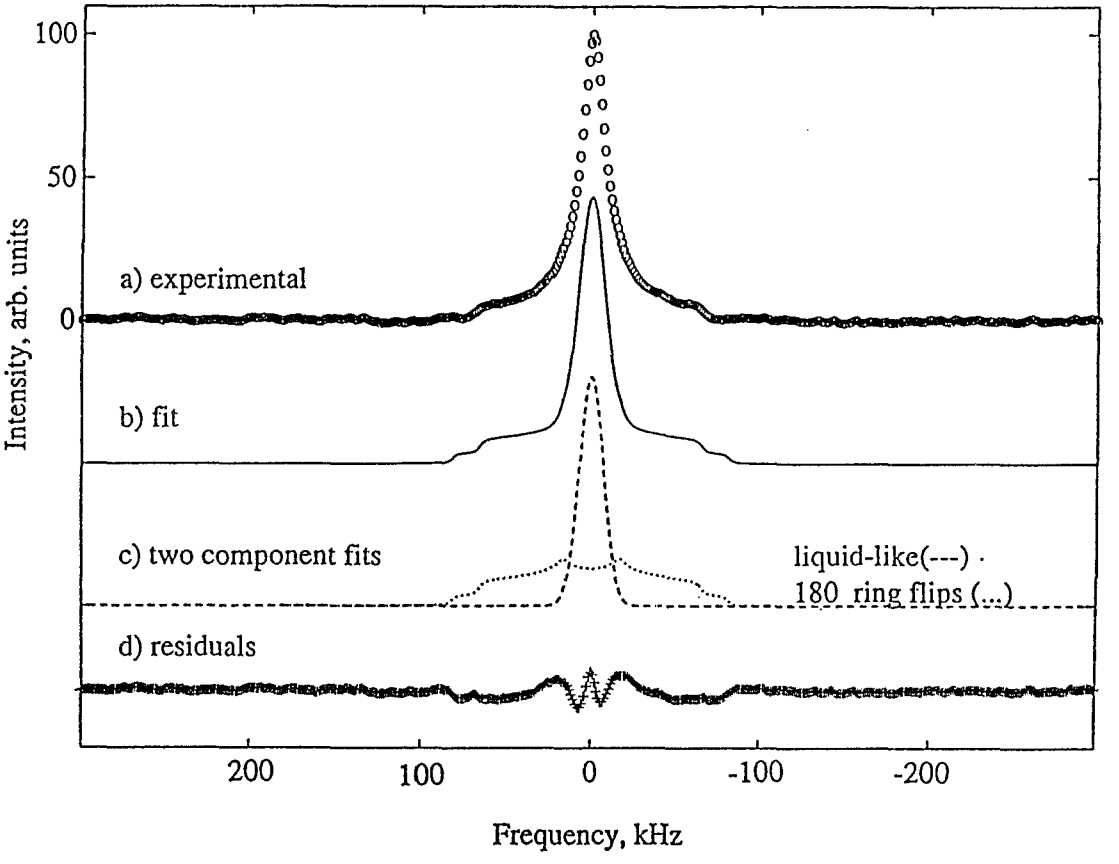

Figure 4.3 Results from a nonlinear least–squares analysis of the ^2H NMR spectrum 10% d_5–phenol by wt. in white portland cement solidified in an NMR tube for one year: a) experimental ^2H NMR spectrum; b) best calculated fit with eq. 4.2; c) the fit is composed of two deuterium components: liquid–like (——) and 180° ring flips (...); d) residuals. $\chi^2_\nu = 0.62$. The amount of solid calcium phenoxide (phenol executing 180° ring flips) = 55 (2)%; the remaining phenol exists in a freely mobile, liquid–like phase and is not bound to the cement matrix.

independent ^{13}C NMR spectral data confirming that ionization has taken place (*14*). An operative assumption here is that much of the pore water in the cement matrix can be removed by crushing the sample, followed by overnight oven treatment, for example, 24 hours at 95°C. After oven treatment, one sample had a 13.5% lost in weight due to the evaporation of pore water. As a result the precipitation of the phenoxide, mainly as Ca salts, will occur. Figure 4.4 shows spectra of 10% d_5–phenol in cement sample that was crushed after 2 months of cure. Figure 4.4a, taken at 295 K immediately after crushing, shows a liquid–like spectrum; the best fit indicates 45 (2)% of phenol in the sample has liquid–like mobility. In contrast, after oven treatment, Figure 4.4b, the spectrum shows a line shape corresponding to 180° ring flips, and little evidence of a liquid–like phase; only 5 (3)% of the phenol retains liquid–like mobility. The samples corresponding to Figures 4.4a,b were studied again at 1 yr. An increase in the liquid–like component for sample 4.4b indicated readsorption of water from the atmosphere. Additional experiments on other samples including monitoring of sample mass (water gain/loss) shows effective reversibility for the oven treatment process. That is, dried samples were rehydrated and the ^2H NMR line shape was transformed from restricted motion (Figure 4.4b) to mostly liquid–like mobility (Figure 4.2c).

Since the spectrum in Figure 4.4b, showing 180° ring flips, is in the fast exchange regime (Figure 3.2), the ring flip rate must be 10^8 s^{-1} or faster. In principle, the ^2H spin–lattice relaxation time,T_1, can be used to measure the rate in the fast exchange regime. The theoretical T_1 ($\theta = 0°$) and T_1 ($\theta = 90°$) curves as a function of the 180° flip rate for phenol at a Larmor frequency of 30.7 MHz are shown in Figure 4.5. Unfortunately, over a range of temperatures, 200–360 K, a rather narrow range of T_1's (7–20 ms) was obtained. This small range in ^2H T_1 is probably due to the interference of paramagnetic relaxation from Fe^{+3} sites,

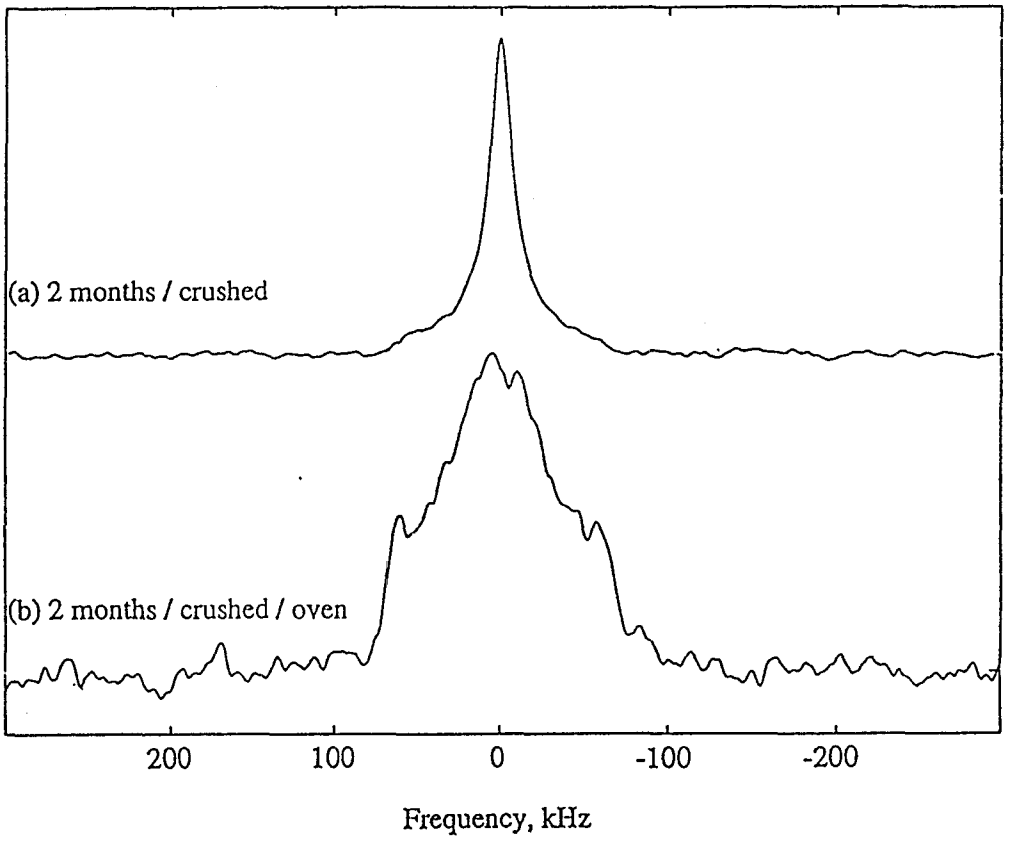

Figure 4.4 Deuterium NMR spectra for 10% d_5–phenol by wt. in white portland cement sample that has been crushed after 2 month cure: a) immediately after crushing, 298 K, spectrum shows large liquid–like phenol resonance, 45 (2)%; b) a similar sample as in (a), but after forced drying of pore water (oven treatment for 36 hours at 90 °C). Spectrum acquired at 298 K and shows very little liquid--like phenol, about 5 (3)%.

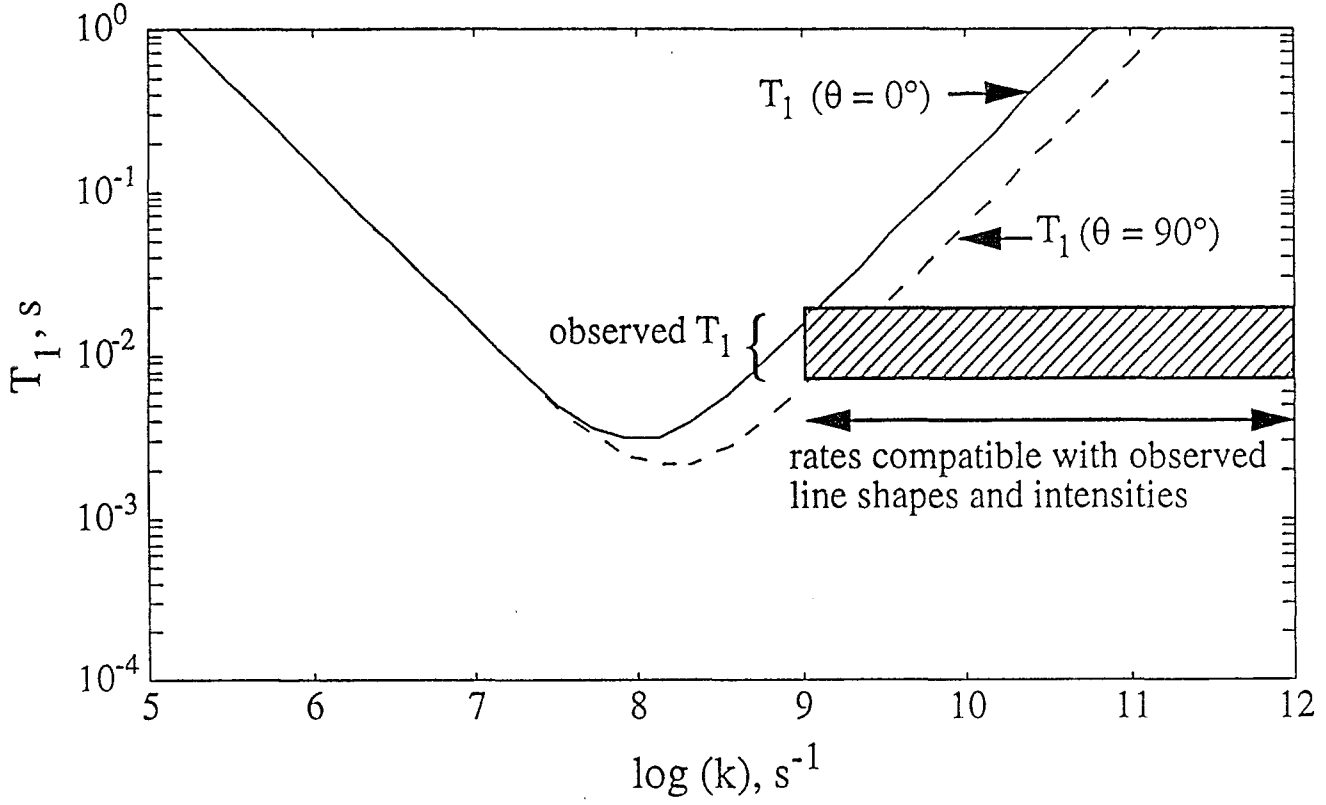

Figure 4.5 Theoretical deuterium T_1 curves at 30.7 MHz as a function of 180° flip rate and tentative minimum jump rate at low temperature, 260 K, based on experimental T_1 data and line shape.

otherwise longer T_1's would have been observed at the higher temperatures. Therefore, the quality of the T_1 data for samples showing 180° ring flips is not sufficient to allow us to determine the activation energy, E_a, unambiguously. Also, there seems to be a distribution of activation energies within the solid–like component that cannot be resolved from the T_1 data. However, based on constant spectral intensities and unvarying line shapes between 260–360 K, and combined with the T_1 data, the bulk of the sites have jump rates $\geq 10^9$ s^{-1}. By using an estimated value for the preexponential factor of 4×10^{13} s^{-1} and the lowest temperature (260 K) for which constant intensity and line shape were obtained, we estimate that the largest possible activation energy for 180° ring flips is approximately 5.5 kcal/mol.

For comparison, in amorphous poly(*p*–phenylene) at room temperature, 180° ring flips are rapid and have a correlation time of about 10^{-7} s^{-1} (*71*). This corresponds to an activation energy close to 9 kcal/mol. The crystalline component of poly(*p*–phenylene) has a higher, but undetermined, activation energy. In fact, the spectra for poly(*p*–phenylene) at different temperatures are quite similar to those found herein for phenol/cement (after oven treatment or evaporation), with the single difference of a somewhat lower activation barrier for phenol/cement.

Solid–state ^2H NMR spectroscopy has several highly useful advantages for the study of solidification/stabilization (S/S) processes: (1) Since the isotope is not abundant, the molecules to be studied must be isotopically enriched. Thus, only a selected component of a rather complex material is visible; the rest of the material is a non–interfering matrix. (2) Solid–state ^2H NMR is particularly useful for detecting microscopic motion of molecular species, both the rate and the mode of motion. Because of the goal of S/S, the study of molecular motions is crucial to identifying successful strategies. (3) Solid–state ^2H NMR is a non–invasive,

nondestructive technique. The same sample can be studied repeatedly. (4) Solid–state ^{2}H NMR spectra will always consist of overlapping resonances, i.e., a narrow liquid–like resonance and a broad resonance from a constricted site. Within some modest limits, multiple components (usually two) can be monitored. Limitations here are similar to those affecting any technique used to study a system having broad distributions of sites within each component. (5) Temperature dependent solid–state ^{2}H NMR spectra are relatively easy to acquire. Therefore, the rate of motion can be studied as a function of temperature and activation energies can be extracted. Under favorable circumstances, the measured activation energy may correspond to a feature important in the S/S process.

There is a wide variation in the deuterium line shape, corresponding to changes in the mode and rate of d_5–phenol reorientation in portland cement. At room temperature, most phenol in cement is very mobile, even to relatively low loadings, 0.1% by weight, of phenol in cement. These results can be compared with other research on phenol and related wastes in cement, which shows that phenol is poorly immobilized by portland cement. Even though the samples are nominally dry and solid in appearance, we believe voids containing liquid–like phenol are present because of the liquid–like ^{2}H NMR resonance for a significant fraction of the phenol. Furthermore, the liquid–like spectrum was observed for loadings ranging from 0.1% to 10%. The content of the voids is not given by deuterium NMR, nor by SEM which has shown evidence of voids in the phenol/cement matrix (*22*). Possibilities are an aqueous solution of an alkali or alkaline earth salt of phenol. The calcium salt of phenol has been characterized by FTIR and ^{13}C CP/MAS NMR techniques which indicate that the ipso carbon shifts down–field by about 7–10 ppm upon formation of the salt (*17*). The ^{13}C CP/MAS NMR spectroscopy of phenol/cement (*51,72*) and the ^{13}C NMR spectra of [1–$^{13}C_1$]phenol versus

[1–$^{13}C_1$]phenol/cement (*73*) shows that there is approximately a 8 ppm shift of the ipso carbon. This indicates the formation of a phenoxide, and the ^{13}C NMR spectrum also show no presence of phenol in the non–ionic form .

This research has shown that the majority of the phenol in a cement matrix, even at 0.1% loading, is in a liquid–like form, but there is at least one environment that exists in which the phenolic oxygen is immobilized within the matrix. It is certainly understandable that the chemistry of phenol could be quite complex under the conditions of a hydrating cement paste. The basic chemical forms could be PhOH, PhOCaOH or $(PhO)_2Ca$ or even ones in which the PhO replaces HO bound to Si or Al, i.e., $PhOSiO_3^{3-}$ or $PhOAl(OH)_3^-$, for instance. The solubilities of these chemical forms are not known, certainly not in the high ionic strength cement pore water. In addition, there are many possibilities for binding to surfaces by ionic interaction of PhO^- or hydrogen bonding by PhOH.

Our current physical interpretation of these results is that most of the phenol is dissolved as the phenoxide ion in the pore water of the cement matrix. Calcium phenoxide is formed, which in a highly basic condition such as the cement hydration process is believed to be slightly soluble in water. It has been previously determined by a study of proton relaxation times of white cement and deionized water that there is 50% pore water available after one month (*74*) and some pore water after one year (*75*). Since calcium phenoxide is slightly soluble, the excess pore water in cured portland cement is a major problem for S/S of phenol in cement. We assume that our crushed samples allow the evaporation of pore water and eventual precipitation of the phenoxide as mainly Ca salts. The activation energy of phenol undergoing 180° flips is approximately 5.5 kcal/mol, which is approximately ten times greater than RT. The activation energy for this process is important as it sets a lower limit for the phenol–cement bond strength (Figure 4.6).

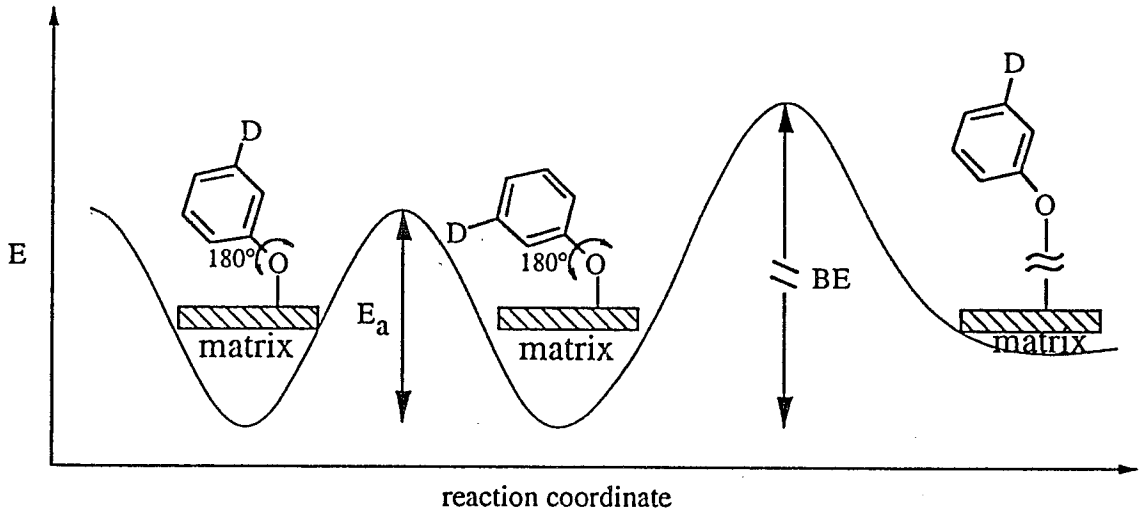

Figure 4.6 A scheme for molecular motion and ultimate dissociation of phenoxide from a matrix illustrating the connection between E_a for 180° ring flips and the phenoxide–matrix binding energy. Based on the ^2H NMR line shape and T_1 results for an oven dried sample, the maximum barrier for 180° ring flips is 5.5 kcal/mol at most sites, though, some sites may have a smaller value for E_a. Since the ^2H fast exchange line shape is observed, the activation energy for 180° ring flips must be less than the bond dissociation energy, BE. If BE < E_a, then only the static and liquid–like line shapes would have been observed, not the k = 10^9 s^{-1} line shape as found here. Since the maximum E_a is 5.5 kcal/mol, the BE at most sites must be greater than 5.5 kcal/mol.

Since the activation energy for ring flipping must be less than the phenol–matrix dissociation energy, the phenol–matrix dissociation energy must be greater than 5.5 kcal/mol; that is, 23 kJ/mol of energy can be added to the system, and the phenol stays in a bound state. It is not surprising that the phenol is easily leached by water even if the binding energy of phenol in the cement matrix is much more than about 23 kJ/mol, solvation energies can provide a driving force that can overcome such binding. In fact, the studies of dried and rehydrated sample, which then show liquid–like mobility, are consistent with the macroscopic observation of leaching.

CHAPTER 5

CONSTANT TIME PULSED FIELD GRADIENT STIMULATED ECHO NMR SPECTROSCOPY

5.1. Introduction

The solidification/stabilization (S/S) process for any liquid–phase hazardous waste has several possible results: the waste may react with the matrix to yield a solid product incorporated in the matrix; the waste may fail to react with the matrix, yet becomes encapsulated in the form of liquid–filled vesicles within the matrix; or the waste reacts with the matrix, yet the reaction product remains fluid and is encapsulated in vesicles.

Because aqueous waste streams commonly contain phenols as constituents, there have been many studies done on S/S using phenols as model wastes (*8-15*). We know from previous ^{2}H and ^{13}C NMR research that phenol reacts with the cement to form a phenoxide salt, but at a cure time of one month, almost all of the salt remains highly mobile at a molecular scale, and consequently, is not properly immobilized. The ^{2}H NMR experiments show that phenol in a cement matrix is mainly present as a salt dissolved in pore water, but with time the amount of pore water decreases, and the proportion of solid phenoxide salt increases (*14,76*). Scanning electron microscope results show that phenol in cement creates readily observable spherical vesicles in the cement matrix with diameters up to 1 mm (*22*). From these results one would suspect that the vesicles contain phenoxide salt dissolved in pore water.

A NMR–based procedure, constant time pulsed field gradient stimulated echo (PFGSE), is tested for a liquid waste encapsulated within a solidified matrix.

PFGSE NMR spectroscopy yields a size distribution image of vesicles containing fluid, with a potential resolution of 0.1 μm.

Herein, we have applied bounded diffusion PFGSE NMR spectroscopy to the study of phenol/monoclinic tricalcium silicate (C_3S) paste interactions to determine if there are liquid waste vesicles entrapped in the C_3S paste. The results show that most fluid–filled vesicles of waste are less than 3.8 μm in diameter.

5.2. Experimental

Monoclinic tricalcium silicate (C_3S) was used as the solidifying agent and was obtained from Construction Technology Laboratories in Skokie, Illinois. C_3S was used because it consists of less than 0.1% Fe_2O_3 by weight which reduces the interference of paramagnetic relaxation. The procedure used to make the samples was as follows: All samples were prepared under a nitrogen atmosphere in order to reduce the formation of carbonates on the surface of the cement. Samples studied contain 10% phenol by weight relative to C_3S (5 g C_3S, 0.5 g phenol, 1.6 mL D_2O) and a water/C_3S ratio of 0.32 by weight. The mixture was stirred in a borosilicate glass vial until apparent homogeneity (ca. 2 minutes) and allowed to solidify in the glass vial. At three months a sample was broken out of a vial and a small solid portion of the sample, approximately a 0.4 cm cube, was transferred to 5 mm NMR glass tube.

We attempted to do the bounded diffusion experiment with white portland cement but were unsuccessful due to its Fe content (about 0.3% Fe_2O_3 by weight) that caused paramagnetic relaxation which led to extremely short ^1H and ^{13}C spin–lattice relaxation times, T_1, 4 ms and 20 ms respectively. In order for the bounded diffusion experiment to be performed, T_1 must be comparable or larger than diffusion time, t_d, and encoding time, t_e, must be less than t_d. The diffusion

coefficient, D, of the sample, the T_1, and the maximum gradient sets the range of vesicles that can be observed (see Figure 5 in reference 32). The diffusion time used must be comparable to or longer than the time needed for spins to transverse the size vesicle that can be observed, otherwise, the spins will not reach the walls of the vesicle, and the actual vesicle size cannot be detected. In order for the bounded diffusion experiment to be performed for an organic fluid in a white portland cement matrix with ^1H T_1 = 4 ms and D = 1.3 x 10^{-6} cm^2 sec^{-1} (vida infra), the maximum gradient strength must be in excess of 1000 G/cm. With a 1000 G/cm gradient, vesicles sizes on the order of 0.1 μm can be probed (*32*). Even though the ^{13}C T_1 of [1–^{13}C]phenol (Cambridge Isotope Lab., Woburn, MA.) in white portland cement is five times larger than that of ^1H, the experiment was still unsuccessful because the ^{13}C gyromagnetic ratio is 1/4 that of ^1H, therefore, most of the advantage gained from a longer T_1 is lost by the smaller gyromagnetic ratio. Because the maximum gradient for the Doty probe is 40 G/cm, it was necessary to increase the T_1 of the sample. By using C_3S, instead of white portland cement, the ^1H T_1 of phenol in the cement matrix increased from 4 ms to 70 ms, thereby allowing this experiment to be performed with a gradient of 40 G/cm, t_e of 4 ms, and t_d times between 10 ms – 70 ms. This allows vesicles in the range of 3.8 to 10.0 μm to be detected, in which the spins have enough diffusion time to transverse.

When the sample was first prepared using C_3S, it was done with a water/C_3S ratio of 0.5 by weight and a liquid layer formed above the paste. Solution–state ^{13}C NMR spectroscopy of this liquid showed a chemical shift for the *ipso* carbon of the aromatic ring upfield by approximately 8 ppm as compared to phenol. This shift indicates deprotonation of phenol to form the phenoxide ion (*17*). It is probable that this liquid resembles that expected in the vesicles (a phenoxide salt

dissolved in pore waters), therefore, it was used to determine the diffusion coefficient of the liquid waste in the vesicles and shall be referred to as the liquid phenoxide sample for the rest of this chapter.

NMR spectra were acquired on a solution–state Bruker AC–200 spectrometer with a Doty Scientific $^{1}H/^{13}C$ 5 mm pulsed z gradient probe (g = 20 G/cm A, L = 40.3 μH). The gradient current was supplied by a Kepco bipolar operational power supply/amplifier (BOP 20–20M with IEEE–488 interface) controlled by a LabVIEW program, a graphical programming language (*63*), that monitored a TTL signal from the AC–200 (decoupler on – SPF2). A maximum value of ± 40 G/cm was used for the gradient (incremented by ±1.25 G/cm per experiment) and it was switched on 10 ms prior to the first rf pulse in order to allow the gradient to stabilize, thus avoiding problems of generating reproducible gradient pulses. Gradient stability was also aided by using a digital IEEE–488 interface built into the Kepco power supply rather than an analog current control signal. A relaxation delay of 1 s was used with a 8 pulse phase cycling scheme similar to CYCLOPS (*77*). The extensive phase cycling was used to eliminate the effects of T_1 (the loss of spin encoding) during t_d. Because this phase cycling is eliminating from the echo any spin magnetization that relaxes, there will be a loss in signal intensity by a factor of $(1- e^{-t_d/T_1})$.

Cis–polybutadiene was used to test the performance of the bounded diffusion experiment and instrumentation being used. Because cis–polybutadiene has no diffusional motion, it is a very good sample to test probe/instrument performance and obtain a minimal resolution of the experiment to which our results can be compared. Figure 5.1 is the displacement profile of cis–polybutadiene. The experimental system passed the test for a maximum gradient of 40 G/cm, but our experimental resolution was limited by the conditions used. The experimental

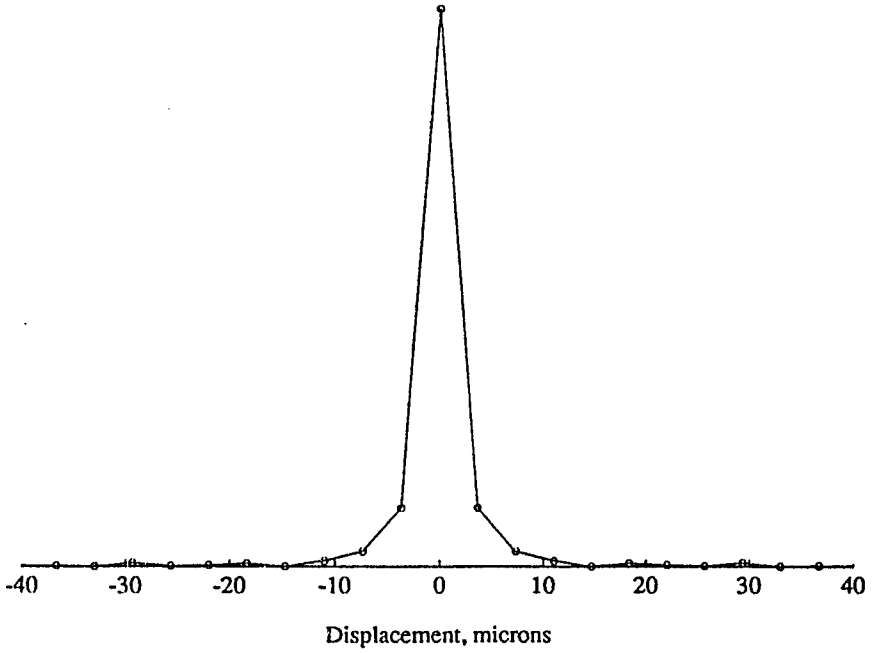

Figure 5.1 Diffusion displacement profile for cis–polybutadiene with diffusion time of 10 ms, encoding time of 4 ms, and maximum gradient 40 G/cm.

resolution, as mentioned earlier, depends on the encoding time and maximum gradient. This displacement profile sets the lower resolution of vesicles that can be detected with the conditions of the experiment. If a sample displacement profile is obtained similar to that of Figure 5.1, it would be an indication that the vesicle size is less than the experimental conditions can detect.

5.3. Results and Discussion

Figure 5.2 shows the ^1H diffusion displacement profile for the liquid phenoxide sample. As can be seen in the profile, the Gaussian response broadens as the diffusion time increases which indicates unbounded free diffusion. Figure 5.3 shows the plots of the full width at half maximum of the Gaussian from Figure 5.2 versus the square–root of the diffusion time. The relationship is linear, and the diffusion coefficient of the liquid phenoxide sample is extracted from the slope of Figure 5.3. The diffusion coefficient at 25°C for this sample is 1.3 (3) x 10^{-6} cm^2 sec^{-1} and it is this value that will be assigned as the diffusion coefficient for phenoxide salt dissolved in pore water. This value is smaller, as expected, than that for pure phenol in water which is 8.4 x 10^{-6} cm^2 sec^{-1} (*78,79*).

The ^1H diffusion displacement profile for 10% phenol by weight in C_3S paste is shown in Figure 5.4. It is very similar to that of Figure 5.1. The PFGSE NMR experiment, as used herein, does not have the proper spatial resolution for measuring the size of very large or very small vesicles. The results reported here only show that most vesicles are less than 3.8 μm in diameter because a large contribution from larger vesicles would have been observed as unbounded diffusion, and there was no evidence of this.

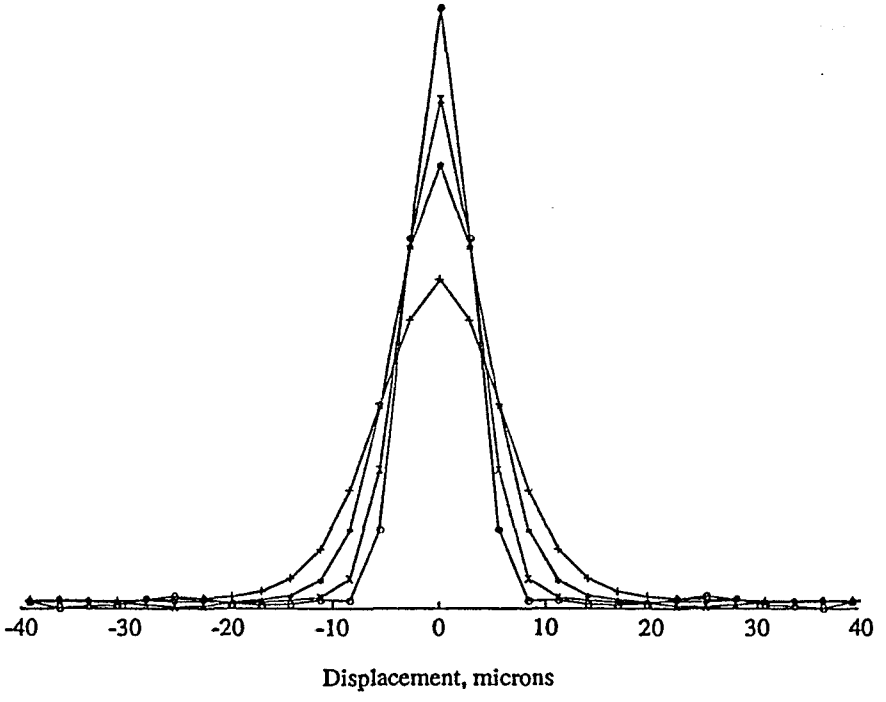

Figure 5.2 Diffusion displacement profile for liquid phenoxide with diffusion times of 20 ms (o), 40 ms (x), 80 ms (*), and 160 ms (+). The maximum gradient was 40 G/cm and the encoding time was 5.25 ms which covered a displacement range of ±88 μm.

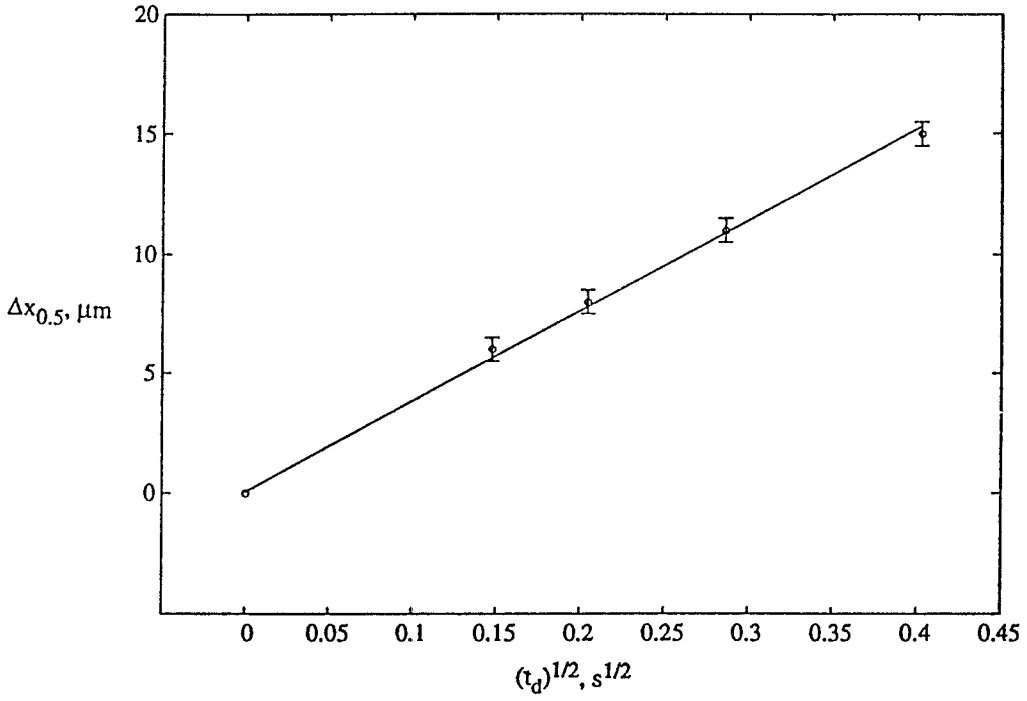

Figure 5.3 Plot of the full width at half–maximum for the diffusion displacement profiles given in Figure 5.2 for liquid phenoxide. The diffusion coefficient is calculated from the slope of the line which is obtained from the full width at half–maximum ($\Delta x_{0.5}$):
$\Delta x_{0.5} = 2[4\ D\ t_d\ \ln(2)]^{1/2}$ where D is the diffusion coefficient and t_d the diffusion time.

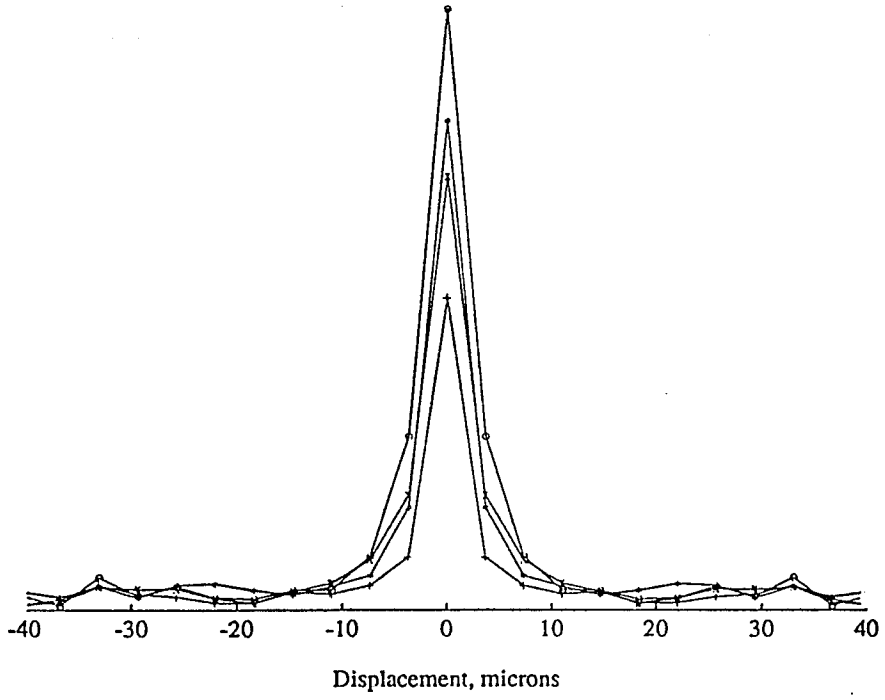

Figure 5.4 Diffusion displacement profile for 10% phenol by wt. in C_3S paste with diffusion times – 10 ms (o), 20 ms (*), 30 ms (x), and 70 ms (+). The maximum gradient was 40 G/cm and the encoding time was 4 ms which covered a displacement range of ±116 μm.

The loss in intensity from 10 to 70 ms diffusion times is due to a short T_1, on the order of t_d. There is a loss in signal intensity by a factor of $(1- e^{-t_d/T_1})$, which is very noticeable in this experiment because of the short T_1, ≈70 ms, of the sample.

There is an interesting difference in the results of this constant time PFGSE NMR experiment, which shows that most vesicles are less than 3.8 μm in diameter, and the results of SEM images, which show a distribution of spherical vesicles up to 1 mm in diameter. The difference is attributed to a Poisson distribution of vesicle sizes such that the NMR experiment is sensitive to the most common vesicle, on a mass basis, whereas the SEM images tend to be dominated by a few large, readily visible vesicles.

CHAPTER 6

THREE–DIMENSIONAL NMR IMAGING

6.1. Introduction

There are a number of reasons for three–dimensional imaging of hazardous waste in a solidification/stabilization (S/S) remediation project. Evidence of a connected pore structure would be an indication of poor S/S, since a readily accessible pathway is then available for leaching of the waste through the cement. Also, experiments can be conceived in which the mobility of the waste is monitored when (for example) one face of the matrix is exposed to representative environmental conditions, i.e., ground water.

This is the first use of 3D NMR imaging for the purpose of analyzing hazardous waste solidified in cement and demonstrates the feasibility of the technique. Three–dimensional imaging of a material like a waste/cement mixture is technically difficult. In fact, we know of no example in the field of hazardous waste S/S. Potential techniques for imaging these materials include synchrotron x–ray tomography (*80*), positron emission tomography (*81*), and nuclear magnetic resonance (NMR) imaging, also known as magnetic resonance imaging (MRI) in the biomedical community.

While NMR imaging has many biomedical applications (*82,83,47*), only recently have applications been presented for nonbiological materials: for example, observing water and dodecane (*84,85*) and water flow (*86-88*) in sedimentary rocks, imaging a chromatographic process (*89*), imaging gas imbibed in porous ceramics (*90*), monitoring chemical oscillators (*91*), measuring the rate of diffusion of solvents through polymers (*92,93*) and monitoring gas–solid chemical

reactions (*94*). In principle, imaging can be done on any NMR–active nucleus, though severe technical limitations remain for many sample types, and ^1H studies are by far the most common. The technical difficulties are particularly severe for cement samples due to short relaxation times and magnetic susceptibility effects (*95*). Herein, we have applied 3D ^1H NMR imaging to a waste (phenol)/cement sample with very encouraging results.

6.2. Experimental

The sample contained 10% phenol by weight relative to low iron content white portland cement. The water/cement ratio used was 0.5 by weight, hence the loading for this particular sample was 10 g white cement, 1 g phenol, and 5 mL D_2O. The mixture was stirred in a borosilicate glass vial until apparent homogeneity (ca. 2 minutes). Some of the bulk sample was transferred to a 5 mm NMR tube and allowed to cure for approximately six months. The particular portion of bulk sample used in this experiment was approximately 1 cm in length.

The images were acquired using a Bruker AMX–400 NMR spectrometer with a wide bore imaging probe and a sample temperature of 50 °C. A voxel size of 100 x 100 x 100 μm was acquired using the technique of spin echo 3D imaging with an echo time of 865.2 μs, recycle time of 100 ms, and 32 averages per image plane. The experiment duration was 3.6 h. The resulting image was 64 by 64 by 128 voxels yielding a field of view of 6.4 by 6.4 by 12.8 mm.

6.3. Results and Discussion

Figure 6.1 is a photo of two of the larger features found in the data set. Each feature is seen from three different views. These two dark features are probably air pockets because of the lack of proton signal, as pores filled with liquid phenol

would have been bright under the conditions of the experiment (the recycle delay is long with respect to the ^1H T_1 of phenol in cement, ~ 7 ms). In this first, rather crude, experiment, three positive findings are evident: (1) the experiment is relatively fast; (2) NMR imaging of cements is feasible, as shown by the sharp boundaries at the walls of the NMR tube; (3) imaging of an added component in cement is possible at a modest concentration of real practical interest.

Liquid–filled pore spaces in cement matrices cover a range from microns in diameter down to tenths of a micron. Void spaces, which vary in frequency and size depending on mixing parameters, are typically much larger. We were not able to see the smaller pore spaces in this first attempt due to our resolution, but resolutions in the range of 10 μm are possible, and direct observation of at least the larger pore spaces should be a realistic goal. Another application, which is clearly feasible with the current technology, and in fact is expected to be a straight forward experiment, is placing a sample in contact with a leaching medium and observing, over time, the infiltration of water into the sample or migration of an organic waste out of the sample. NMR imaging experiments have been developed that take advantage of differences in the chemical shifts (resonant frequency of a particular site within a molecule) such that it is possible to selectively image only one chemical species in a mixture, thus adding to the information content of the NMR imaging experiment.

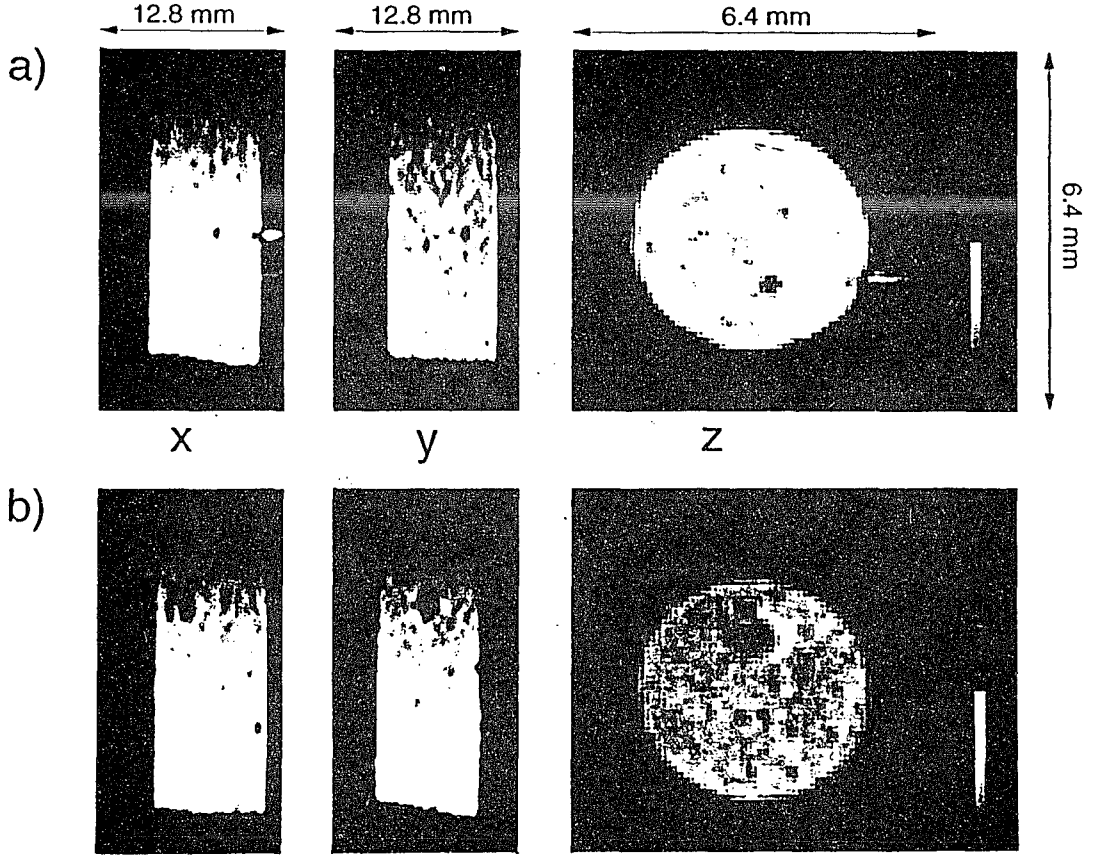

Figure 6.1 3D NMR images of a mixture of 10% phenol by weight in white portland cement. This is a photo of two of the larger features in the data set that extends over the entire length, ~ 1 cm, of the sample. Each feature is seen from three different views.

CHAPTER 7

HOLE–BURNING NMR SPECTROSCOPY

7.1. Introduction

There is an obvious need to establish clear proof that the process of waste solidification/stabilization (S/S) in cement does indeed work. We are developing a method for analyzing the microscopic motions of organic and inorganic waste in the cement matrix. Chemical shift anisotropy produces inhomogeneous broadening of NMR lines in solids. Holes can be burned into such lines, tagging molecules which are at certain orientations. Subsequent molecular reorientations result in a spectral diffusion. Detailed knowledge of the reorientation is obtained by measuring the broadening and recovery of the hole as a function of time.

Herein, we are using a NMR method called hole–burning that has shown useful information in other applications (*96-99*) but has not been applied to cementitious samples. The rationale for the hole–burning experiment on the waste/cement matrix is quite simple. If there is no microscopic motion of the waste in the cement matrix, then the recovery from the hole–burning experiment occurs on the time scale of the spin–lattice relaxation time (T_1), and the line shape does not change as a function of the variable delay. However, if there is microscopic motion of the waste, then the recovery occurs at a rate different from T_1, and the line shape of the hole shows increasing broadening with an increase in the variable delay time.

This technique will give information on the microscopic motions of hazardous waste in the cement matrix. This technique is quite unlike other methods for assessing the quality of S/S, for example, total leaching studies. This technique

gives information on the microscopic waste mobility which should offer a more definitive answer as to whether or not a waste is successfully trapped in the cement matrix.

7.2. Experimental

The experiments were performed on a Bruker MSL–200 NMR spectrometer. The pulse sequence used for hole–burning is a long low power saturation pulse, a variable delay for chemical site exchange, and a hard 90° pulse for sampling (Figure 7.1). The long low power pulse burns a hole into the NMR line. The low power pulse was supplied by a homemade transmitter (*100*). This pulse is typically 1 – 15 ms and 10 – 30 mV of rf amplitude. Hence, the frequency spectrum of the burn pulse is narrow. After the hole is burned, a delay of time τ occurs during which the molecules can reorient, diffusing the hole through the NMR line. The line is then inspected by application of a hard (normal rf amplitude) 90° pulse.

Two cement samples were tested (organic and inorganic waste): 1) 10% [1–13C]phenol by weight relative to white portland cement; 2) 10% Pb ($Pb(NO_3)_2$) by weight relative to white portland cement. Both samples had a water/cement ratio 0.5 by weight. The mixtures were stirred in a borosilicate glass vials until apparent homogeneity (ca. 2 minutes). The samples were immediately transferred to NMR glass tubes and allowed to solidify.

7.3. Results and Discussion

Figure 7.2 is a map of the selectively saturated frequency interval caused by the hole–burn experiment. It is the actual "hole" that is being created by the long low power pulse. Any spins that are in this frequency interval will be saturated and not contribute any magnetization to the powder pattern.

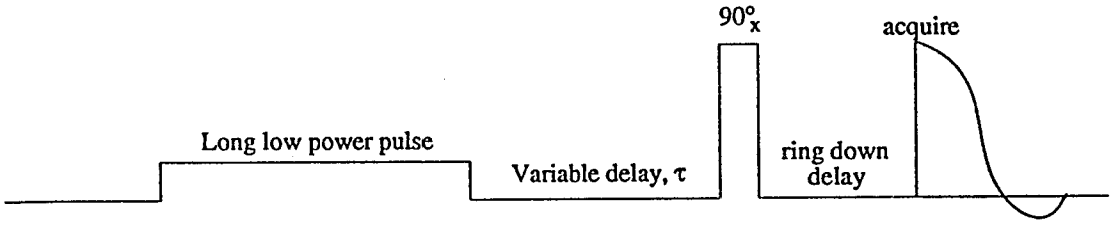

Figure 7.1 Pulse sequence used in hole–burning experiment.

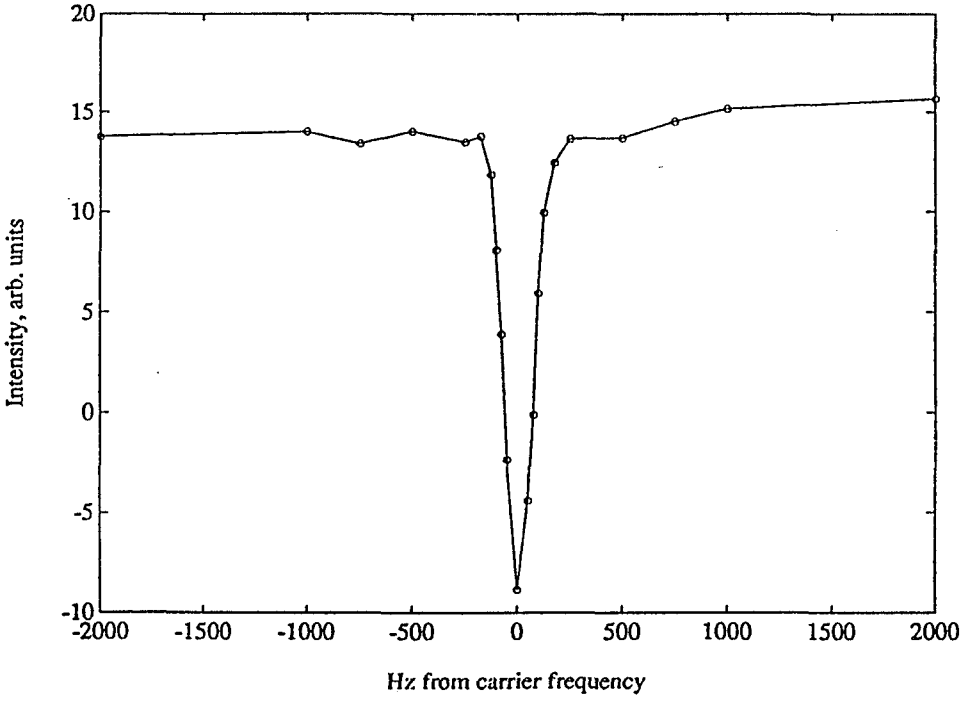

Figure 7.2 Map of selectively saturated frequency interval caused by the long low power pulse in the hole–burning experiment.

7.3.1. Organic Hole–Burning – [1–^{13}C]Phenol

Figure 7.3 shows spectra at 230 K of 10% [1–^{13}C]phenol by weight in white portland cement at various diffusion times. The burn pulse was 10 ms with a rf amplitude of 17.4 mV_{pp} which amounts to a 15° tip angle. The hard 90° pulse used in this experiment was 6.5 μs with 1.1 V_{pp} (Appendix C.1). It was not possible to burn a hole within the line shape, but instead a saturation of the line shape occurred. This indicates that the line shape was homogeneously broadened, meaning each spin has approximately the same resonance frequency, i.e. a liquid or glassy solid. We know from deuterium NMR spectroscopy that phenol has 2 components within the cement matrix, liquid–like and solid executing 180° ring flips. These spectra are obviously from the liquid–like component. Figure 7.4 shows the same sample at the same diffusion times but instead at 200 K. A hole was able to be burned within the line shape indicating inhomogeneously broadening by chemical shift anisotropy, each spin has a different resonance frequency, i.e. a solid. Spectral diffusion within an inhomogeneously broadened line shape can be detected by inspecting the burned hole and line shape. Spin–lattice relaxation (T_1) effects will only change the overall intensity of the line and hole, not their shape. Figure 7.4 shows evidence of molecular reorientations occurring during the diffusion time because the burn hole is broadening with increasing diffusion times, and the line shape is not recovering on the time scale of T_1. The sides of the line shape are being saturated by spins from the burn hole region moving during the diffusion time to that region. This is a clear indication of molecular motion of phenol within the cement matrix.

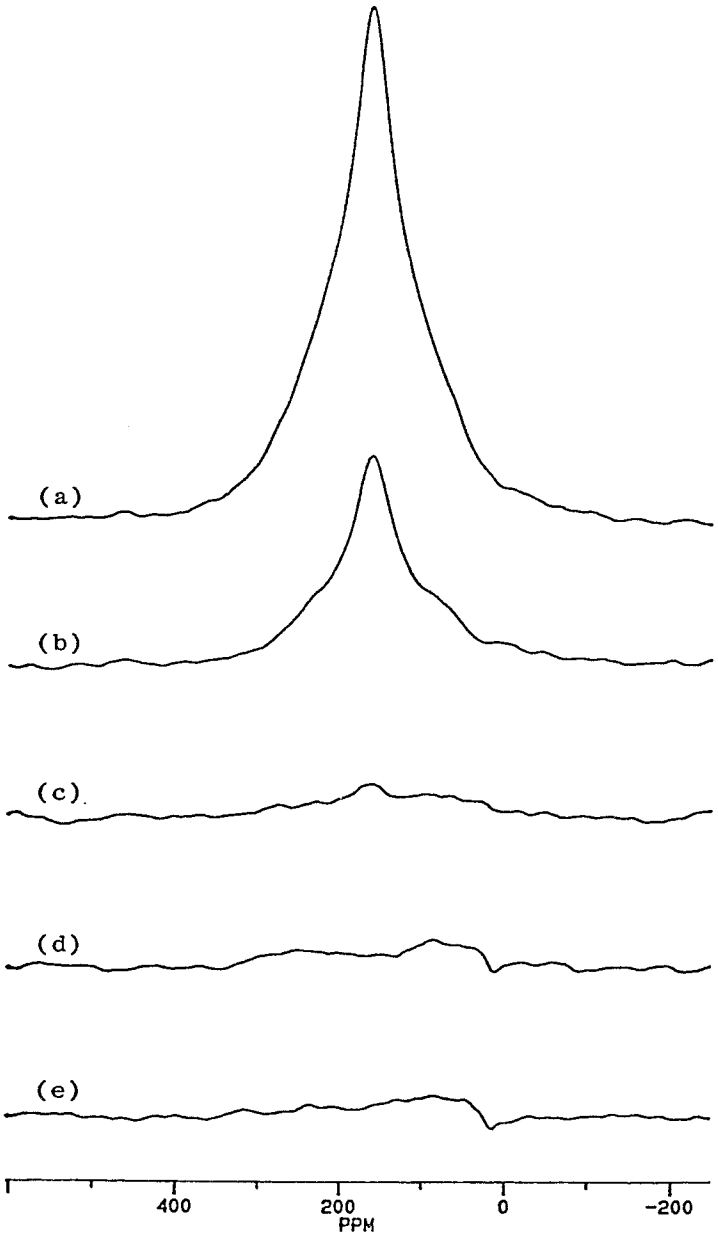

Figure 7.3 ^{13}C NMR hole–burning recovery of 10% [1–^{13}C]phenol/cement by weight at 230 K. Relaxation delay was 1 s with delays: a) 1 s, b) 50 ms, c) 5 ms, d)800 μs, e) 50 μs.

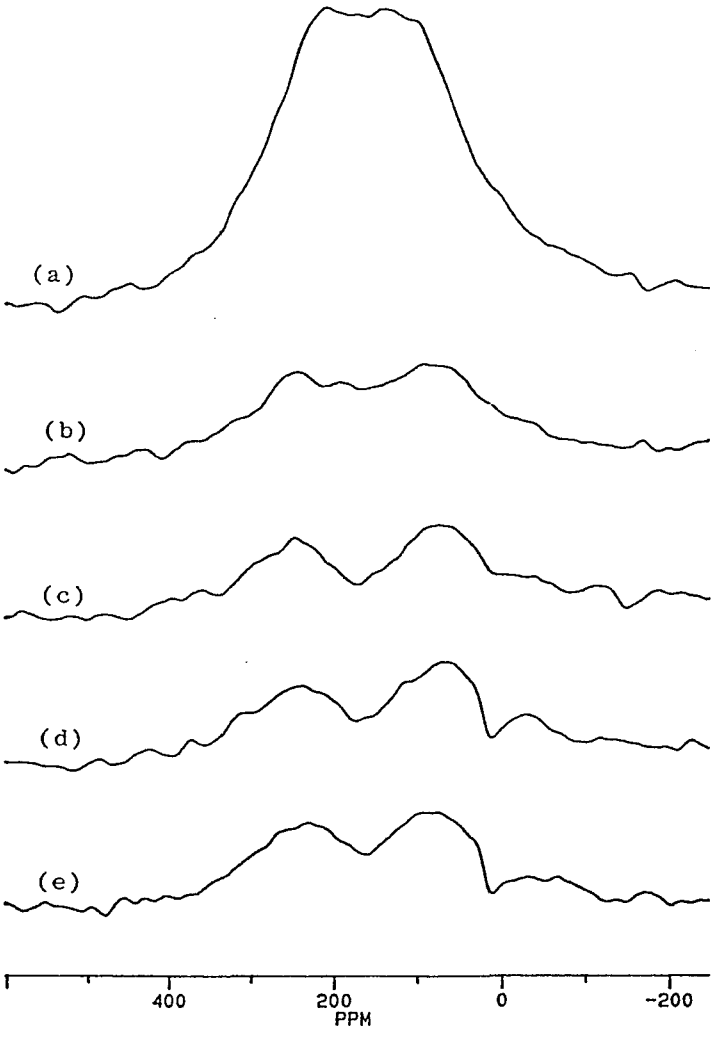

Figure 7.4 ^{13}C NMR hole–burning recovery of 10% [1–^{13}C]phenol/cement by weight at 200 K. Relaxation delay was 1 s with delays: a) 1 s, b) 50 ms, c) 5 ms, d)800 μs, e) 50 μs.

7.3.2. Inorganic Hole–Burning – $Pb(NO_3)_2$

The NMR hole–burning experiment was tested on lead nitrate (^{207}Pb) at room temperature (Figure 7.5). The burn pulse was 5 ms with a rf amplitude of 11.6 mV_{pp} which amounts to a 4° tip angle (Appendix C.2). The hard 90° pulse used in this experiment was 4 μs with 2.72 V_{pp}. The burned hole in the ^{207}Pb chemical shift powder pattern recovered at the ^{207}Pb T_1 and did not grow in width, in agreement with the expected lack of lead ion motion in this solid.

It is at this point that the experiment is completely set up and working. We would like to do this experiment on a Pb waste/cement sample, but a major hurdle must be overcome before this experiment can be done. We have not been able to find any Pb signal from the waste/cement samples. Many NMR experiments were attempted in order to obtain an effective pulse program that would maximize the Pb signal in waste/cement samples.

There are many reports in the literature that suggest $Pb(NO_3)_2$ forms a complex mixture in the cement matrix (*19,49,101*). The Pb in $Pb(NO_3)_2$/cement samples must be present in amorphous forms because x–ray diffraction detected no lead–containing crystalline phases (*101*). The most likely amorphous lead–containing phase in cement would be lead hydroxide.

Because pure $Pb(OH)_2$ (white powder) has a very large NMR powder pattern, a very poor NMR sensitivity, and the expected form of Pb in $Pb(NO_3)_2$/cement samples, it was used as the sample in the signal enhancement experiments. The experiments were attempted on all three probes (wideline, 4 mm, 7 mm) for the MSL–200 NMR spectrometer. The different experiments tried were magic angle spinning (MAS), cross polarization/MAS, stimulated echo (*102,103*), and non–spinning NMR. Of all these experiments the 4 mm MAS experiment gave the

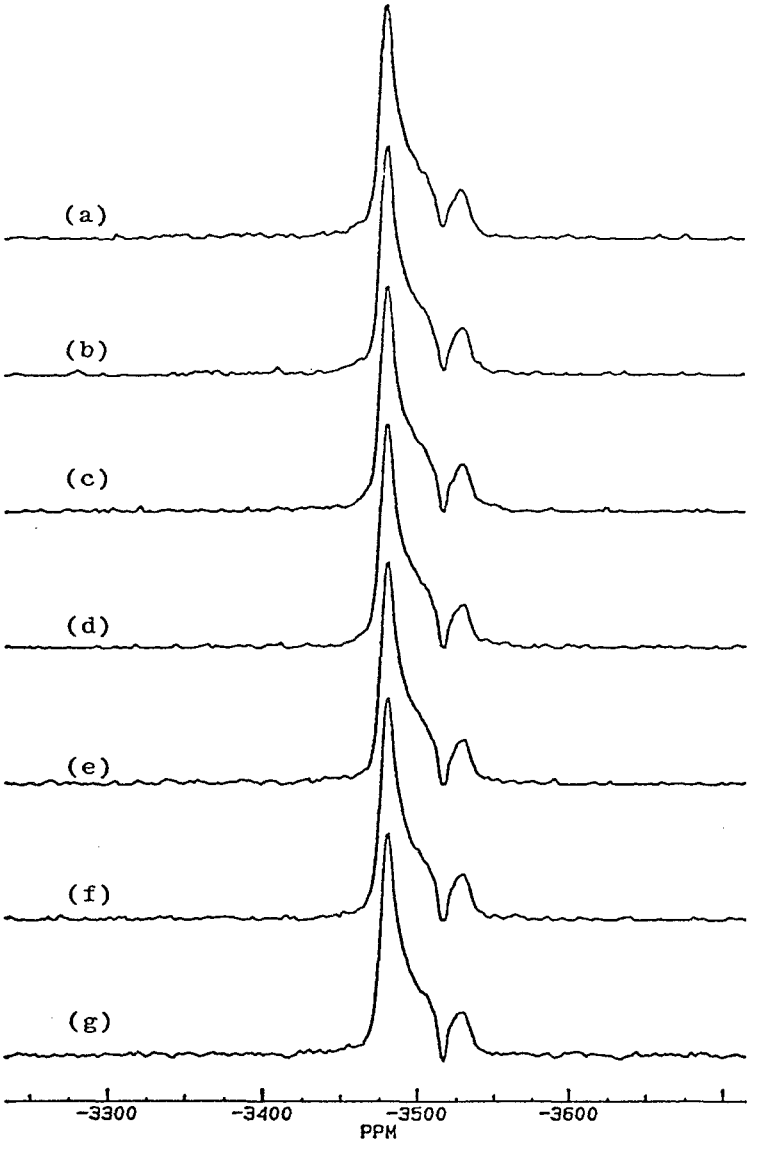

Figure 7.5 207Pb NMR hole–burning recovery of lead nitrate at 297K. The hole width remains constant through the recovery, indicating no motion. Relaxation delay was 5 seconds with delays: a) 1 s, b) 500 ms, c) 200 ms, d) 100 ms, e) 50 ms, f) 20 ms, g) 10 ms.

best results (Figure 7.6). This spectrum shows the very large powder pattern of $Pb(OH)_2$ (~170 kHz) which contributes to its poor sensitivity as can be seen by the 160,000 scans required for a S/N of 10.

An instrument problem was encountered that had a dramatic impact on the success of this experiment. The MSL–200 NMR spectrometer gave an intense NMR signal at 42 MHz which was very near that of Pb. This signal was so intense that it made tuning up the MSL and performing experiments very difficult. After many hours of searching, the problem was tracked to the third harmonic of 14 MHz clock signal in the graphics display processor. This signal misguided our results for a period of time, but when the problem was realized, it was overcome by acquiring data with the graphics display processor off; the advice from Bruker was largely useless. This problem was a considerable nuisance and limited our experimental capabilities for NMR near 42 MHz, i. e., ^{207}Pb NMR.

As for the Pb/cement samples, many long experiments (24–72 hrs) were done but failed to produce any Pb signal. The variables in these experiments were the carrier frequency covering a frequency range of ± 5000 ppm, and the recycle time varying from 200 ms – 60 s. The reasons that the Pb signal in $Pb(NO_3)_2$/cement samples might not be detected may be due to the fact that there are many Pb sites, it has a huge powder pattern (>1 MHz), and/or it has an extremely low sensitivity.

As for the Pb experiment, it must be realized that if the assumption that Pb in $Pb(NO_3)_2$/cement samples forms $Pb(OH)_2$ is correct, the amount of Pb in the cement samples is 24 μmoles which is 14 times less than that in pure $Pb(OH)_2$. Therefore, if it takes 24 hours to obtain a S/N of 10 for $Pb(OH)_2$, then it will take 14 days to acquire the same S/N for Pb in 10% $Pb(NO_3)_2$ by weight in cement. The major problem with the Pb/cement samples is a combination of sensitivity, and

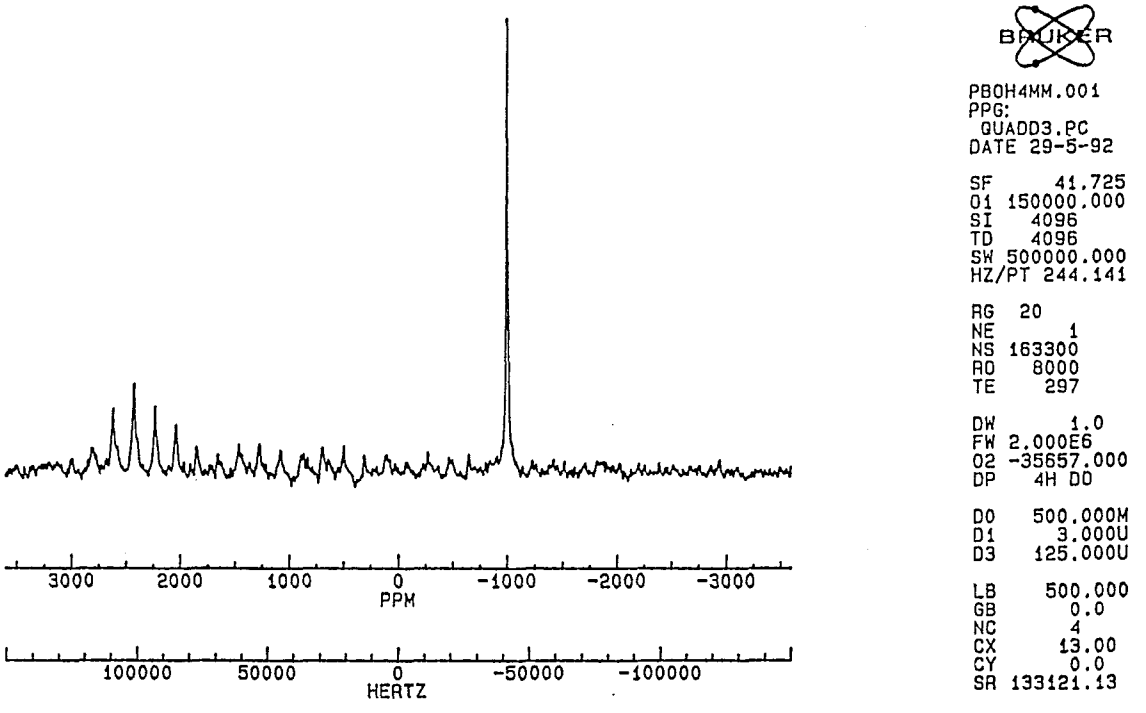

Figure 7.6 4 mm MAS NMR spectrum of lead hydroxide.

its large line width. Table 7.1 shows that Pb has a very broad chemical shift range (4550 to –3494 ppm) with very large powder patterns. If there is a wide range of sites for the Pb in cement, it would be very difficult to detect these sites over such a large range of chemical shifts and low sensitivity. The signal would be lost in the baseline. The question arises what is needed for this experiment to work? What is needed is a smaller chemical shift range with a smaller line width compared to Pb. Table 7.1 is a list of possible nuclei for the hole–burning experiment. These nuclei have either smaller chemical shift ranges or narrower line widths or both. Even if these nuclei form many sites within the cement matrix, they should be detectable because of the smaller chemical shift range over which the signal will occur.

Table 7.1: Principal Components of Miscellaneous Nuclei at Room Temperature

Nucleus	% Natural abundance	NMR ν @4.7 T	Compound	Chemical shift (ppm) δ_{iso}	$\Delta\delta$	reference
^{207}Pb	22.6	41.842	$Pb(NO_3)_2$ aq	-2961	0	(*104*)
			PbO_2	4550	?	(*104*)
			$Pb(NO_3)_2$	-3494	53	(*105*)
			PbO	?	1845	(*106*)
			$PbCO_3$	-2641	770	(*107*)
			$Pb(OH)_2$	?	4000	(*108*)
^{111}Cd	12.75	42.41	0.1 M $Cd(ClO_4)_2$	0	0	(*104*)
^{113}Cd	12.26	44.364	CdS	687	54	(*109*)
			$Cd(NO_3)_2.4H_2O$	-100	180	(*110*)
^{195}Pt	33.8	42.998	K_2PtCl_6	0	0	(*111*)
			$K_2[Pt(OH)_6]$	3476	420	(*112*)
			K_2PtCl_4	-1848	250	(*111*)
^{77}Se	7.58	38.134	$Se(CH_3)_2$	0	0	(*104*)
			H_2SeO_3	1288	453	(*113*)
			PbSe	-631	0	(*114*)
^{119}Sn	8.58	74.544	$(CH_3)_4Sn$			
			5% in CH_2Cl_2	0	0	(*104*)
			$CaSnO_3$	-612	0	(*115*)
			SnO_2	-604	125	(*115*)
			$[(CH_3)_2SnS]_3$	108	211	(*116*)
^{125}Te	6.99	63.192	$Te(CH_3)_2$	0	0	(*104*)
			CdTe	-1087	0	(*114*)
			$Te(OH)_6$	686	120	(*117*)

CHAPTER 8

CARBON–13 NMR SPECTROSCOPY

8.1. Introduction

This chapter gives the results of ^{13}C NMR spectroscopy of phenol solidified/stabilized in cement. This study was done to determine the nature of phenol solidified in a cement matrix. In the ideal case, optimal waste/cement interaction during solidification/stabilization (S/S) most likely requires an irreversible chemical reaction rather than simple physical entrapment. For phenol, the most likely reaction pathway is deprotonation in the highly basic cement ($pH \geq 12$), and formation of a calcium salt, since Ca^{+2} is the overwhelmingly predominant cation present in portland cement. Two Ca salts are possible, PhOCaOH and $(PhO)_2Ca$, and both have been characterized showing that the *ipso* carbons of the two salts have different ^{13}C chemical shifts, 168 and 161 ppm, respectively (*14*). We know from deuterium and ^{13}C hole–burning NMR spectroscopy that there are at least two environments of phenol in the cement matrix: a liquid-like and solid form. It is believed that if some information can be learned about the chemistry of the liquid–like component compared to the solid component, the S/S process could be modified to convert the liquid–like into solid form thereby allowing successful S/S of phenol. Herein, we have applied ^{13}C NMR spectroscopy to determine if there is a difference in structure between the two components.

8.2. Experimental

8.2.1. Sample Preparation

The sample was made using 10% [1–^{13}C]phenol by weight relative to white portland cement with a water/C_3S ratio of 0.5 by weight. The mixture was stirred in a borosilicate glass vial until apparent homogeneity (ca. 2 minutes) and some of the sample was transferred to 5 mm NMR glass tube. The sample cured for 15 months before the experiments were performed.

8.2.2. NMR Experiments

All experiments were acquired using a solid-state Bruker MSL–200 spectrometer. All spectra consisted of the same parameters such as relaxation delay between scans of 3 s, 200 scans averaged, spinning rate of 1000 Hz, and external reference to TMS (0.0 ppm). There were three different NMR experiments performed on the same sample. The differences between these three NMR experiments are the controlling factors of the information that can be obtained by each experiment. The first experiment consisted of a single 90° ^{13}C pulse. This experiment can detect liquid–state resonances and cannot detect solid-state resonances because they are weak without ^{1}H–^{13}C cross polarization. The second experiment consisted of ^{1}H–^{13}C cross–polarization with a contact time between ^{1}H–^{13}C of 5 ms. This experiment can detect solid–state resonances, and cannot detect liquid–state resonances because cross–polarization affects dipolar interactions which average to zero in liquids due to the rapid rotation of molecules in liquids. However, if the cross–polarization time is shorter than the reciprocal of the dipolar coupling constant, i.e. 20 μs, then ^{1}H–^{13}C vectors do not have enough time to reorient all angles with respect to the magnetic field to average the dipolar interactions to zero thereby allowing the observation of liquid–state resonances.

Experiment three consisted of exactly this situation with a $^{1}H-^{13}C$ cross–polarization of 5 μs. This experiment can detect liquid–state resonances and solid–state resonances of carbon sites that have an abundance of protons nearby. Spinning side bands detected in any of these experiments will be an indication of a solid because liquids do not have chemical shift anisotropy, therefore do not have spinning side bands.

8.3. Results and Discussion

Figure 8.1 shows the ^{13}C spectrum of phenol/cement using a single 90° pulse. There is a chemical shift of the *ipso* carbon atom (attached to oxygen of the hydroxyl group) by approximately 10 ppm downfield from 156 ppm in pure phenol to 166 ppm in cement. There are many examples of salts of hydroxides in which the chemical shift for the *ipso* carbon shifts downfield by about 7 - 10 ppm upon formation of a salt which makes it possible to distinguish ionized from nonionized phenol (*17*).

Figure 8.2 consists of the spectrum of the 5 ms $^{1}H-^{13}C$ cross–polarization while Figure 8.3 contains the 5 μs $^{1}H-^{13}C$ cross–polarization. There is a 3 ppm shift between the *ipso* carbon of these two figures from 163 ppm for Figure 8.2 to 166 ppm for Figure 8.3. There is also the presence of very strong spinning side bands in Figure 8.2 while there are only very weak ones in Figure 8.3. The spinning side bands in Figure 8.3 are correlated to an isotropic chemical shift position of 163 ppm and not to the 166 ppm peak in the spectrum indicating the presence of a liquid at 166 ppm and a solid at 163 ppm. Figure 8.1 is from liquid–like phenoxide while Figure 8.2 is from solid phenoxide, and Figure 8.3 shows signs of both liquid–like and solid phenoxide. Figures 8.1 and 8.2 show the presence of only one kind of phenoxide salt for each component. Typical NMR

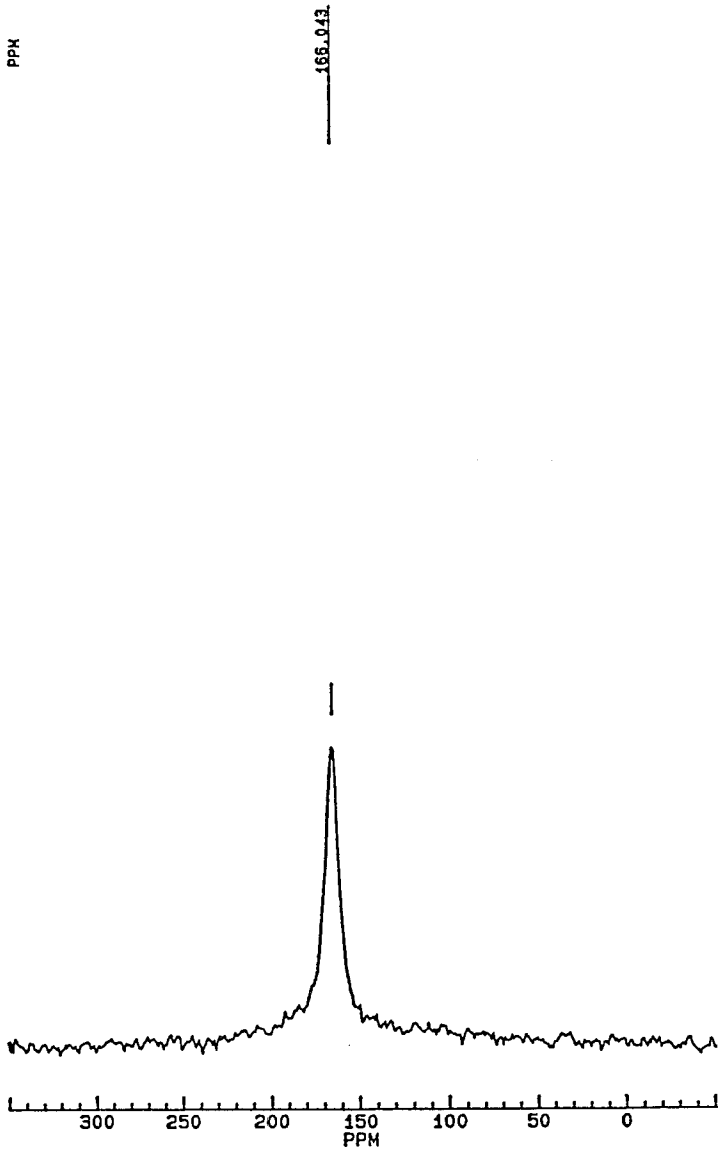

Figure 8.1 ^{13}C spectrum of 10% [1-^{13}C]phenol by weight relative to white portland cement with a water/C_3S ratio of 0.5 by weight. The sample cured for 15 months before the experiment was performed. This spectrum was acquired using a single 90° pulse, relaxation delay of 3 s, 200 scans, spinning rate of 1000 Hz, and an external reference to TMS.

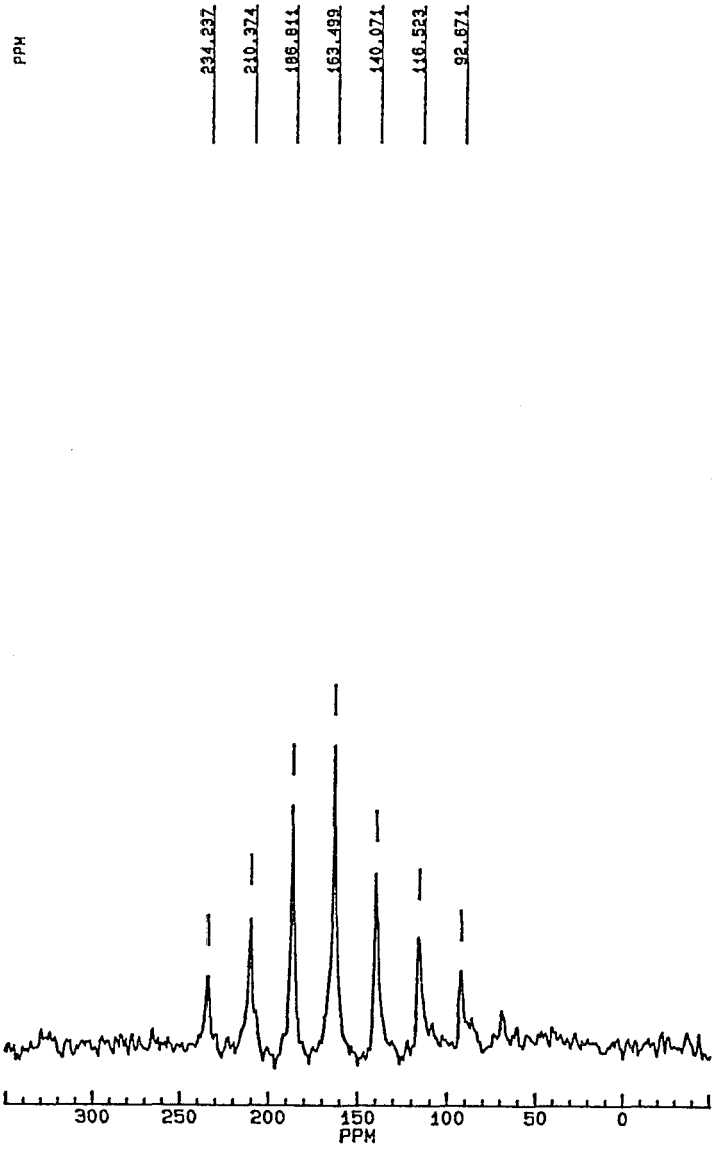

Figure 8.2 ^{13}C spectrum of 10% [1-^{13}C]phenol by weight relative to white portland cement with a water/C_3S ratio of 0.5 by weight. The sample cured for 15 months before the experiment was performed. This spectrum was acquired using ^{1}H–^{13}C cross-polarization with a contact time of 5 ms, relaxation delay of 3 s, 200 scans, spinning rate of 1000 Hz, and an external reference to TMS.

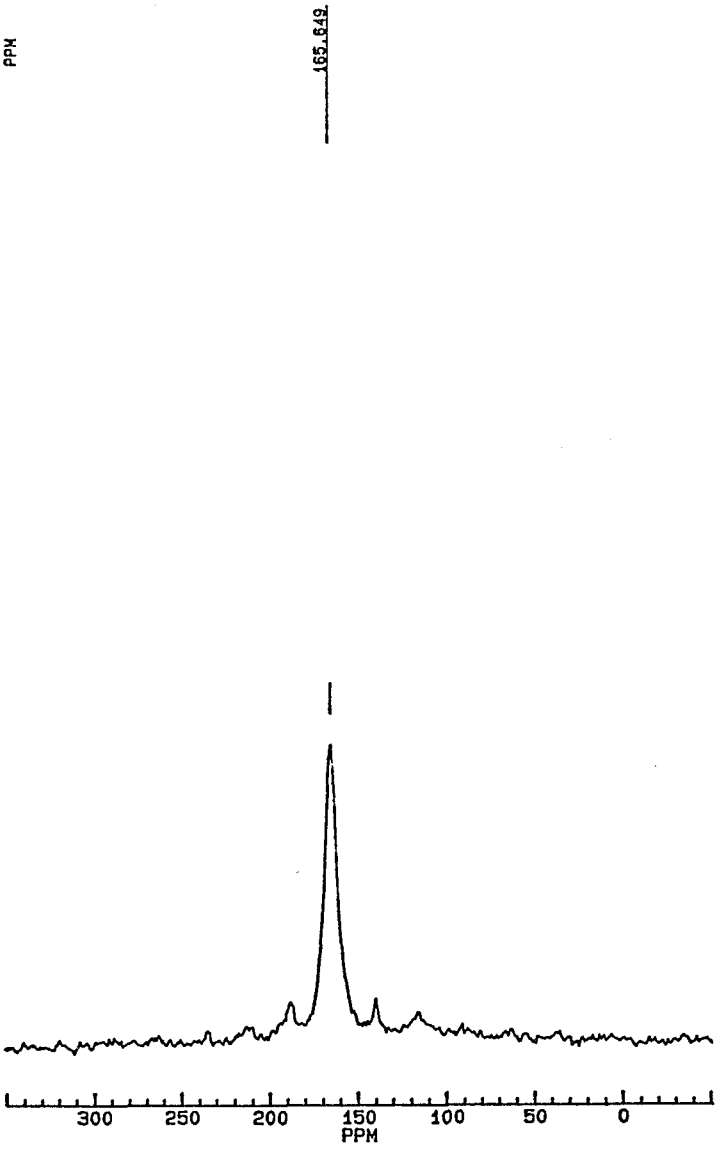

Figure 8.3 ^{13}C spectrum of 10% [1-^{13}C]phenol by weight relative to white portland cement with a water/C_3S ratio of 0.5 by weight. The sample cured for 15 months before the experiment was performed. This spectrum was acquired using ^{1}H–^{13}C cross-polarization with a contact time of 5 μs, relaxation delay of 3 s, 200 scans, spinning rate of 1000 Hz, and an external reference to TMS.

experiments require 10^{19} nuclei to be detected. The fact that only one kind of phenoxide salt for each component is obtained indicates that there is no presence of any other phenoxide salt above 5% by weight. The results of this experiment show the presence of two different phenoxides within the cement matrix: tentatively assigning, based on the chemical shifts of these salts (*14*), the liquid–like phenoxide to PhOCaOH and the solid phenoxide to $(PhO)_2Ca$.

CHAPTER 9

CONCLUSIONS

This research was done in order to develop techniques that will give basic chemical data that can help in the understanding of the solidification/stabilization of hazardous waste. We need to understand the process before we can predict performance or design a better technology. A summary of the information obtained by this research follows:

9.1. Solid–State Deuterium NMR Spectroscopy

Solid–state deuterium NMR provides information about the dynamics of a specifically labeled (deuterated) waste in the cement matrix. Both mode and rate of the molecular reorientation affect the spectrum. A distribution of modes and activation energies can exist in a heterogeneous environment such as a cement, and these can be monitored nondestructively by solid–state ^2H NMR spectroscopy.

Important results can be obtained by this technique that are not otherwise obtainable. Over a wide range of loading levels, approximately 50% of the phenol in cement remains quite mobile. The fraction of phenol that is bound to the cement matrix and is executing 180° ring flips has a dissociation energy greater than approximately 5.5 kcal/mol. This is a very important number because it is the lower limit of the phenol–matrix dissociation energy. Phenol is not successfully immobilized in cement on a microscopic scale because the phenoxides are slightly soluble in a highly basic media such as the pore water in portland cement, and this microscopic behavior is presumably the reason for macroscopic observations of high leaching potential for cement–solidified phenols.

This ^2H NMR based procedure can determine if a particular deuterated organic waste is effectively solidified/stabilized, and the lower limit of the bond strength between the waste and the cement matrix. The bond strength is clearly relevant to an evaluation of the reliability of the S/S process for a particular waste. NMR is an effective method for nondestructive monitoring of the microscopic mobility of waste in cements with significant advantages over EPA mandated leaching studies, since quantitative measurements of tethered and free waste can be made. The technique can give information not only about molecular motions but also on the mode of motion. The only significant disadvantage of ^2H NMR for analyzing the performance of S/S is the limitation to waste which can be deuterated; in practice, this restricts one to the study of organic waste. Otherwise, the ^2H NMR procedure is an effective and informative experiment.

9.2. Constant Time Pulsed Field Gradient Stimulated Echo NMR Spectroscopy

This technique can determine if there is liquid waste encapsulated within the solidified matrix. The technique yields a size distribution image of vesicles containing fluids, and measures the diffusion rate of organic materials in solid matrices. For the phenol/cement sample studied, the results show that most fluid–filled vesicles of waste are less than 3.8 μm in diameter though the experiments were done at conditions that, unfortunately, compromised the results. The main problem encountered was resolution which can be overcome by using a larger gradient that should lead to an improved assessment of vesicle size. We were not capable of using a larger gradient, therefore, we could not assess the actual vesicle size.

9.3. Three–Dimensional NMR Imaging

Three–dimensional NMR imaging can be used to determine the degree of homogeneity in solid samples, the structure and connectivity pattern of fluid–filled pores, and the rates of water infiltration into solid samples and waste migration out of solid samples. A major strength of NMR imaging is that it is nondestructive, and so is capable of observing changes in the sample over a period of time. It is a technique that shows promise in the testing of solidified hazardous waste as well as other applications in the near future.

9.4. Hole–Burning NMR Spectroscopy

The hole–burning experiment described is straightforward and applicable to any NMR line which is inhomogeneously broadened by chemical shift anisotropy. This technique gives information on the microscopic motions of waste in the cement matrix. The phenol/cement sample tested using ^{13}C NMR hole–burning shows more evidence that phenol within the cement matrix has two components: a liquid and a solid component and thus supports the results obtained from the ^{2}H NMR work. This technique also shows that the solid component of the phenol waste is undergoing molecular motions within the cement matrix.

While the hole–burning experiment is ready to be used on an inorganic waste/cement sample, it has not as yet been applied. There is potential for this experiment, although some technical difficulties remain to be resolved.

9.5. Carbon–13 NMR Spectroscopy

The ^{13}C experiments show a clear indication that phenol in cement has deprotonated to form the phenoxide salt and shows no evidence of nonionized phenol. An important fact that needs to be determined is if the liquid–like and solid

phenoxide are in different forms. This is very crucial information that is needed to develop a better S/S process for phenol. These three ^{13}C NMR experiments give this information and show that there are two forms of phenoxide in cement: liquid–like phenoxide (PhOCaOH) and solid phenoxide ($(PhO)_2Ca$).

9.6. Closing Statement

Now that we have techniques to obtain information on the microscopic waste/cement interactions, we believe that it will lead to faster development of a better S/S process. These techniques provide a nondestructive evaluation of the quality of S/S process much superior to the destructive techniques such as leaching. This is a giant improvement over leaching studies and gives us hope that future studies of cement additives can be done efficiently to give better understanding of the S/S process, in order that S/S can be applied intelligently, and one can rationally design improved technology.

BIBLIOGRAPHY

(1) U.S. EPA Federal Register. **50** (105), 23250-23258, **1985.**

(2) Resource Conservation and Recovery Act. PL 94-580, **1976.**

(3) Comprehensive Environmental Response, Compensation and Liability Act of 1980. PL 96-510, **1980.**

(4) Conner, J. R. *Chemical Fixation and Solidification of Hazardous Wastes*, Van Nostrand Reinhold, New York, 1990.

(5) Cullinane, M. J.; Jones, L. W. *Stabilization/Solidification of Hazardous Waste*, Cincinnati: U.S. Environmental Protection Agency Hazardous Waste Engineering Research Laboratory, EPA/600/D-86/028, 1986.

(6) Landreth, R. E. *Guide to the Disposal of Chemically Stabilized and Solidified Waste*, Cincinnati: U.S. Environmental Protection Agency Hazardous Waste Engineering Research Laboratory, EPA SW872, 1982.

(7) *Environ. Sci. Technol.* **1992**, *26,* 1473.

(8) Cote, P.; Hamilton, D. P. *Proceedings, 38th Ind. Waste Conf., Purdue Univ., Ann Arbor Science, Ann Arbor, MI* **1983**, 221-31.

(9) Cote, P. O.; Bridle, T. R.; Hamilton, D. P. *Fixation* **1985**, 302-8.

(10) Sheriff, T. S.; Sollars, C. J.; Montgomery, D.; Perry, R. *Environmental Technology Letters* **1987**, *8,* 501-14.

(11) Cartledge, F. K.; Eaton, H. C.; Tittlebaum, M. E. *U.S. EPA Risk Reduction Engineering Laboratory Project Report, EPA/600/S2-89/056* **1989**, avail. NTIS (PB90-134156).

(12) Kolvites, B.; Bishop, P. *Column Leach Testing of Phenol and Trichloroethylene Stabilized/Solidified with Portland Cement* in *Environmental Aspects of Stabilization and Solidification of Hazardous Radioactive Wastes, ASTM STP 1033, P.L. Cote and T.M. Gilliam, eds., ASTM: Philadelphia,* 1989, 238-50.

(13) Sheriff, T. S.; Sollars, C. J.; Montgomery, D.; Perry, R. *The Use of Activated Charcoal and Tetra-Alkylammonium-Substituted Clays in Cement-Based Stabilization/Solidification of Phenols and Chlorinated Phenols* in *Environmental Aspects of Stabilization and Solidification of Hazardous Radioactive Wastes*, STP 1033, P.L. Cote and T.M. Gilliam, eds., ASTM: Philadelphia, 1989, 273-86.

(14) Cartledge, F. K.; Bulter, L. G.; Akhter, H.; Tittlebaum, M. E.; Chalasani, D.; Janusa, M. A.; Yang, S. *Solid-State NMR Characterization of Organics in Cement* in *Cement Industry Solutions to Waste Management*, Proceedings, 1st Intl. Symp., Calgary, Oct. 1992: Canadian Portland Cement Association, 1992, Toronto, 289-305.

(15) Sell, N. J.; Revall, M. A.; Bentley, W.; McIntosh, T. H. *Solidification and Stabilization of Phenol and Chlorinated Phenol Contaminated Soils* in *Stabilization and Solidification of Hazardous, Radioactive and Mixed Waste, 2nd Volume*, STP 1123, M.Gilliam and C. Wiles, eds., ASTM: Philadelphia, 1992, 73-85.

(16) Lea, F. M. *The Chemistry of Cement and Concrete*, 3rd edition ed., Chemical Publishing Co., Chicago, 1971.

(17) Schlosberg, R. H.; Scouten, C. G. *Energy and Fuels* **1988**, *2,* 582-85.

(18) Sheffield, A.; Makena, S.; Tittlebaum, M.; Eaton, H.; Cartledge, F. *Hazardous Waste and Hazardous Material* **1987**, *4,* 273-286.

(19) Cartledge, F. K.; Butler, L. G.; Chalasani, D.; Eaton, H. C.; Frey, F.; Tittlebaum, M. E.; Yang, S.-L. *Environ. Sci. Technol.* **1990**, *24,* 867-73.

(20) Chou, A. C.; Eaton, H. C.; Cartledge, F. K.; Tittlebaum, M. E. *Hazardous Waste & Hazardous Materials* **1988**, *5,* 145-53.

(21) Walsh, M. B.; Eaton, H. C.; Tittlebaum, M. E.; Cartledge, F. K.; Chalasani, D. *Hazardous Waste & Hazardous Materials* **1986**, *3,* 111–23.

(22) Vipulanandan, C.; Krishnan, S. *J. Hazard. Mater.* **1990**, *24,* 123-36.

(23) Hartmann, S. R.; Hahn, E. L. *Phys. Rev.* **1962**, *128,* 2042.

(24) Gerstein, B. C.; Dybowski, C. R. *Transient Techniques in NMR of Solids*, Academic Press, Inc., Orlando, Florida, 1985.

(25) Jarrett, W. L.; Guo, K.; Jackisch, M. A.; Butler, L. G. *J. Magn. Res.* **1989**, *82,* 76-85.

(26) Hirschinger, J.; English, A. D. *J. Magn. Res.* **1989**, *85,* 542-553.

(27) Spiess, H. W., . *NMR-Basic Principles and Progress* **1978**, *15,* 59.

(28) Wittebort, R. J.; Olejniczak, E. T.; Griffin, R. G. *J. Chem. Phys.*. **1987**, *86,* 5411-20.

(29) Spiess, H. W.; Sillescu, H. *J. Magn. Res.* **1981**, *42,* 381-9.

(30) Batchelder, L. S.; Niu, C. H.; Torchia, D. A. *J. Am. Chem. Soc.* **1983**, *105,* 2228-31.

(31) Torchia, D. A.; Szabo, A. *J. Magn. Res.* **1982**, *49,* 107-121.

(32) Cory, D. G.; Garroway, A. N. *Magn. Reson. Med.* **1990**, *14,* 435-444.

(33) Hahn, E. L. *Phys. Rev.* **1950**, *37,* 359-87.

(34) Carr, H. Y.; Purcell, E. M. *Phys. Rev.* **1954**, *94,* 630-8.

(35) Stejskal, E. O.; Tanner, J. E. *J. Chem. Phys.* **1965**, *42,* 288-92.

(36) Callaghan, P. T. *Aust. J. Phys.* **1984**, *37,* 359-87.

(37) Callaghan, P. T.; MacGowan, D.; Packer, K. J.; Zelaya, F. O. *J. Magn. Reson.* **1990**, *90,* 177-182.

(38) Xia, Y.; Callaghan, P. T. *Macromolecules* **1991**, 4777-86.

(39) Gibbs, S. J.; Johnson, C. S. J. *Macromolecules* **1991**, 5224-5.

(40) Gibbs, S. J.; Johnson, C. S. J. *Macromolecules* **1991**, 6110-3.

(41) Daivis, P. J.; Pinder, D. N.; Callaghan, P. T. *Macromolecules* **1992**, 170-8.

(42) Tanner, J. E.; Stejskal, E. O. *J. Chem. Phys.* **1968**, *49,* 1768-1777.

(43) Kärger, J.; Heink, W. *J. Magn. Reson.* **1983**, *51,* 1-7.

(44) Lauterbur, P. C. *Nature* **1973**, *242,* 190-1.

(45) Mansfield, P.; Grannell, P. K. *J. Phys. C: Solid State Phys.* **1973**, *6,* L422-6.

(46) Listerud, J. M.; Sinton, S. W.; Drobny, G. P. *Anal. Chem.* **1989**, *61,* 23A-41A.

(47) Callaghan, P. T. *Principles of Nuclear Magnetic Resonance Microscopy*, Oxford University Press, Oxford, 1991.

(48) Bloembergen, N.; Purcell, E. M.; Pound, R. V. *Phys. Rev.* **1948**, *73,* 679.

(49) Ortego, J. D.; Barroeta, Y.; Cartledge, F. K.; Akhter, H. *Environ. Sci. Technol.* **1991**, *25,* 1171-74.

(50) Chalasani, D. Ph.D. Dissertation, Louisiana State University, Baton Rouge, LA, 1988.

(51) Akhter, H. Ph.D. Dissertation, Louisiana State University, Baton Rouge, LA, 1990.

(52) Jelinski, L. W. *Annu. Rev. Mater. Sci.* **1985**, *15,* 359-77.

(53) Sarkar, S. K.; Young, P. E.; Torchia, D. A. *J. Am. Chem. Soc.* **1986**, *108,* 6459-64.

(54) Torchia, D. A. *Annu. Rev. Biophys. Bioeng.* **1984**, *13,* 125-44.

(55) Altbach, M. I.; Hiyama, Y.; Wittebort, R. J.; Butler, L. G. *Inorg. Chem.* **1990**, *29,* 741-7.

(56) Fyfe, C. A. *Solid State NMR for Chemists*, C.F.C. Press, Guelph, Ontario, Canada, 1983.

(57) Bloom, M.; Davis, J. H.; Valic, M. I. *Can. J. Phys.* **1980**, *58,* 1510-7.

(58) Butler, L. G. *J. Magn. Reson.* **1991**, *91,* 396-9.

(59) Fukushima, E.; Roeder, S. B. W. *Experimental Pulse NMR: A Nuts and Bolts Approach*, Addison-Wesley, Reading, MA, 1981, Chapter 5.

(60) Kermit Distribution, Columbia University Center for Computing Activities, 612 West 115th St., New York, NY 10025.

(61) Casey, P. K.; Jarrett, W. L.; Mathias, L. J. *J. Am. Lab. (Shelton, Conn.)* **1989**, *21,* March, p 25-35.

(62) Michaels, D. C.; Kim, A. J.; Perilloux, B. C.; Barksdale, D.; Butler, L. G. *Computers Chem.* **1992**, *16,* 71-2.

(63) LabVIEW, National Instruments Corp., 6504 Bridge Point Parkway, Austin, Tx. 78730.

(64) Bevington, P. R. *Data Reduction and Error Analysis for the Physical Sciences*, McGraw-Hill, New York, 1969.

(65) Press, W. H.; Flannery, B. P.; Teukolsky, S. A.; Vetterling, W. T. *Numerical Recipes*, Cambridge University Press, Cambridge, 1986.

(66) Matlab, The Mathworks Inc., 24 Prime Parkway, Natick, MA 01760.

(67) Kim, A.; Butler, L. G. *Concepts in Magnetic Resonance* **1992**, *4,* 205-26.

(68) Cain, E. J.; Gardner, K. H.; Gabara, V.; Allen, S. R.; English, A. D. *Polym. Prepr., Am. Chem. Soc., Div. Polym. Chem.* **1990**, *31,* 518-20.

(69) We would have preferred and suggest for future studies the use of [2,3,5,6-^{2}H4]phenol instead of [2,3,4,5,6-^{2}H5]phenol as used in this study. This would have eliminated the para-carbon deuteron which was not included in eq.4.2, based on T_1 results.

(70) Janusa, M. A. *unpublished results* **1992.**

(71) Dumais, J. J.; Jelinski, L. W.; Galvin, M. E.; Dybowski, C.; Brown, C. E.; Kovacic, P. *Macromolecules* **1989**, *22*, 612-17.

(72) Akhter, H.; Cartledge, F. K. *unpublished results* **1992**.

(73) Janusa, M. A. *unpublished results* **1992**.

(74) Yang, S. M.S. Thesis, Louisiana State University, Baton Rouge, LA, 1983.

(75) Janusa, M. A. *unpublished results* **1991**.

(76) Janusa, M. A.; Wu, X.; Cartledge, F. K.; Butler, L. G. *Environ. Sci. & Technol.* **1993**, in press.

(77) Bax, A. *Two-Dimensional Nuclear Magnetic Resonance in Liquids*, D. Reidel Publishing Co., Dordrecht, Holland, 1983.

(78) "International Critical Tables of Numerical Data, Physics, Chemistry and Technology"; Washburn, E. W., Ed.; McGraw-Hill Book Co.: New York, 1929.

(79) Kazuhiko, K.; McGreevy, R. J.; Schechter, R. S. *J. Colloid Interface Sci.* **1989**, *132*, 395-402.

(80) Bonse, U.; Nusshardt, R.; Busch, F.; Pahl, R.; Kinney, J. H.; Johnson, Q. C.; Saroyan, R. A.; Nichols, M. C. *J. Mat. Sci.* **1991**, *26*, 4076-85.

(81) Jonkers, G.; Vonkeman, K. A.; van der Wal, S. W. A.; van Santen, R. A. *Nature* **1992**, *355*, 63-66.

(82) NMR Imaging in Biomedicine. Suppl. 2, **1982**.

(83) Morris, P. G. *Nuclear Magnetic Resonance Imaging in Medicine and Biology*, Claredon Press, Oxford, 1986.

(84) Hall, L. D.; Rajanayagam, V.; Hall, C. J. *J. Magn. Reson.* **1986**, *68*, 185-8.

(85) Attard, J. J.; Doran, S. J.; Herrod, N. J.; Carpenter, T. A.; Hall, L. D. *J. Magn. Reson.* **1992**, *96*, 514-25.

(86) Woessner, D. E.; Gleeson, J. W.; Jordan, C. F., Jr. *NMR Imaging of Pore Structures in Limestones SPE 20493* in *65th Ann. Tech. Conf.*, 1990, New Orleans, LA, Sept. 23-26, SPE preprint 20493.

(87) Gleeson, J. W.; Woessner, D. E. *Magn. Reson. Imag.* **1991**, *9*, 879-84.

(88) Robinson, M. A.; Deans, H. A.; Bansal, S. *Determination of Oil Core Flow Velocities and Porosities Using MRI SPE 23960* in *SPE Permian Basin Oil and Gas Recovery Conf.*, 1992, Midland, TX, March 18-20, SPE preprint 23960.

(89) Ilg, M.; Maier-Rosenkranz, J.; Müller, W.; Albert, K.; Bayer, E. *J. Magn. Reson.* **1992**, *96,* 335-44.

(90) Lizak, M. J.; Conradi, M. S.; Fry, C. G. *J. Magn. Reson.* **1991**, *95,* 548-57.

(91) Tzalmona, A.; Armstrong, R. L.; Menzinger, M.; Cross, A.; Lemaire, C. *Chem. Phys. Lett.* **1990**, *174,* 199-202.

(92) Weisenberger, L. A.; Koenig, J. L. *Macromolecules* **1990**, *23,* 2454-9.

(93) Samoilenko, A. A.; Artemov, D. Y.; Sibel'dina, L. A. *Russ. J. Phys. Chem.* **1987**, *61,* 1623-5.

(94) Butler, L. G.; Cory, D. C.; Dooley, K. M.; Miller, J. B.; Garroway, A. N. *J. Am. Chem. Soc.* **1992**, *114,* 125-35.

(95) Fordham, E. J.; Roberts, T. P. L.; Carpenter, T. A.; Hall, L. D.; Maitland, G. C.; Hall, C. *AIChE Jour.* **1991**, *37,* 1895-99.

(96) Conradi, M. S.; Kuhns, P. L. *Bull. Am. Phys. Soc.* **1981**, *26,* 219.

(97) Kuhns, P. L.; Conradi, M. S. *J. Chem. Phys.* **1982**, *77,* 1771-8.

(98) Siminovitch, D. J.; Ruocco, M. J.; Olejniczak, E. T.; DasGupta, S. K.; Griffin, R. G. *Biophys. Jpn.* **1989**, *54,* 373.

(99) Lin, T. H.; Vold, R. R. *J. Phys. Chem.* **1991**, *95,* 9032-4.

(100) Wu, X.; Patterson, D. A.; Butler, L. G.; Miller, J. B. *Review of Scientific Instruments* **1993**, in press.

(101) Zhao, B.; Daugherty, K. E.; Zhang, L.; Ingram, K. D.; Hill, R. *Portland Cement Doped with Lead Compounds* in *Cement Industry Solutions to Waste Management*, Proceedings, 1st Intl. Symp., Calgary, Oct., 1992, Canadian Portland Cement Assn., Toronto, 1992, 359-72.

(102) Liu, S. B.; Conradi, M. S. *Physical Review B* **1984**, *30,* 24-31.

(103) Gullion, T.; Conradi, M. S. *Physical Review B* **1985**, *32,* 7076-82.

(104) Duncan, T. M. *A Compilation of Chemical Shift Anisotropies*, The Farragut Press, Chicago, 1990.

(105) Lutz, O.; Nolle, A. *Z. Phys. B* **1980**, *36,* 323.

(106) Duncan, T. M.; Douglass, D. C. *unpublished results* **1985**.

(107) Nolle, A. *Z. Naturforch.* **1977**, *32a,* 964.

(108) Janusa, M. A. *unpublished results* **1992.**

(109) Nolle, A. *Z. Naturforsch.* **1978**, *33a,* 666.

(110) Mennitt, P. G.; Shatlock, M. P.; Bartuska, V. J.; Maciel, G. E. *J. Phys. Chem.* **1981**, *85,* 2087.

(111) Sparks, S. W.; Ellis, P. D. *J. Am. Chem. Soc.* **1986**, *108,* 3215.

(112) Harris, R. K.; Reams, P.; Packer, K. J. *J. Chem. Soc., Dalton Trans.* **1986**, 1015.

(113) Krieger, A. I.; Moskvich, Y. N.; Sukhovskii, A. A.; Falaleev, O. V. *Phys. Stat. Sol. (A)* **1982**, *69,* 455.

(114) Koch, W.; Lutz, O.; Nolle, A. *Z. Physik. A* **1978**, *289,* 17.

(115) Clayden, N. J.; Dobson, C. M.; Fern, A. *J. Chem. Soc. Dalton Trans.* **1989**, 843.

(116) Gay, I. D.; Jones, C. H. W.; Sharma, R. D. *J. Magn. Reson.* **1989**, *84,* 501.

(117) Collins, M. J.; Ripmeester, J. A.; Sawyer, J. F. *J. Am. Chem. Soc.* **1987**, *109,* 4113.

APPENDIX A

COMPUTER PROGRAMS

A.1. Two-Site Jump Calculation of T_1 vs. Reorientation Rate

```
clc; clear; clg;
% Torchia and Szabo equation for 2 Site Jumps
% See J. Magn. Reson. v49, p107-121 (1982), equation 39
qcc = 175e3;  wQ = (3/4)*(2*pi)*qcc;  w = 2*pi*30.7e6;
k_vector=logspace(2,12);
THETA = (120/2)*(2*pi/360);
A1 = sin(2*THETA)^2;
A2 = sin(THETA)^4;
A3 = sin(THETA)^3 * cos(THETA);
for j=1:length(k_vector)
k = k_vector(j);
theta = 0;
B1 = sin(2*theta)^2;
B2 = sin(theta)^4;
B3 = sin(theta)^3 * cos(theta);
B4 = cos(theta)^2 + cos(2*theta)^2;
B5 = sin(theta)^2 + 1/4*sin(2*theta)^2;
B6 = 1 + 6*cos(theta)^2 + cos(theta)^4;
tau = 1/(2*k);
g_tau_w = tau/(1 + w^2 * tau^2);
g_tau_2w = tau/(1 + (2*w)^2 * tau^2);
```

```
% assume rate constant is equal in both directions
% therefore peq1 and peq2 will equal 0.5
% Equation 39 but omitting phi dependence
% parallel to magnetic field (shoulders of pattern)
T10 = (wQ^2/2)*(1/2)*(1/2)*A1*(g_tau_w*(B4 - 0) + g_tau_2w*(4*B5 - 0) );
T1_0(j) = 1/T10;
theta = pi/2;
B1 = sin(2*theta)^2;
B2 = sin(theta)^4;
B3 = sin(theta)^3 * cos(theta);
B4 = cos(theta)^2 + cos(2*theta)^2;
B5 = sin(theta)^2 + 1/4*sin(2*theta)^2;
B6 = 1 + 6*cos(theta)^2 + cos(theta)^4;
% perpendicular to magnetic field (points of pattern)
T190 = (wQ^2/2)*(1/2)*(1/2)*A1*(g_tau_w*(B4 - 0) + g_tau_2w*(4*B5 - 0) );
T1_90(j) = 1/T190;
end; % end of j loop
V=[5 12 -4 0]; axis(V); x = log10(k_vector);
semilogy(x,T1_0,'-',x,T1_90,'-');
xlabel('log (k), 1/s');ylabel('T1, s');
```

A.2. Nonlinear Least-Squares Analysis Program

```
clg; clear; echo on; hold off;
global  FID_size Fract_two_sites Fract_gaussian xx yy y_calc_new two_sites
global  Int_two_sites Int_gaussian
t0 = clock;  flops(0);
load tube1a1yr;   % xx,yy data sets
y=100*yy/max(yy);
x=xx;
sigma =2;
a = [.1,100,7.5e+3, .3];
%plot for sigma
L=175; %number points to examine for sigma
P=1;
y_temp = y(P:L); %average value of y set at zero
y_temp = y_temp - sum(y_temp)/L;
V = [min(x(P:L)) max(x(P:L)) -3*max(y_temp) 3*max(y_temp)];
axis(V);
plot(x (P:L),y_temp, 'o');hold on;
plot([x(P) x(L)],[0 0], '-');
errorbar(x(P:L),y_temp,sigma*ones(L,1));
pause
inv_sigma_sqr = 1/(sigma^2);
V = [min(x) max(x) -0.1*max(y) 1.1*max(y)]; axis(V);
plot(x,y,'o');
errorbar(x,y,sigma*ones(x));
xlabel('Freq, kHz');          ylabel('Intensities'); hold on;
```

```
[y_calc] = y_Functn(x,a);
plot(x,y_calc);
alpha = zeros(length(a));
beta = zeros(1,length(a));
DA = zeros(1,length(a));
delta_a(1:4) = abs(0.01*a(1:4));
a_new = zeros(1,length(a));
dyda = zeros(length(x),length(a));
N_free = length(y_calc) - length(a);
%  Evaluate Chi Square at starting point and y_exp_new.
chi_sqr_old = CurFit_chisqr(y,y_calc,inv_sigma_sqr,N_free)
% Evaluate ALPHA and BETA.
[dyda] = CurFit_nonanal(x,a,delta_a);
for J = 1:length(a)
for K = J:length(a)
alpha(J,K) = sum(inv_sigma_sqr.*(dyda(:,J).*dyda(:,K)));
alpha(K,J) = alpha(J,K);
end;
end;
for K = 1:length(a)
beta(K) = sum(inv_sigma_sqr.*((y - y_calc).*dyda(:,K)));
end;
%  Invert modified curvature matrix to find new parameters.
lambda = 0.001;
alpha_prime = alpha*(eye(length(a))*(1+lambda));
DA =  beta*inv(alpha_prime);
```

```
a_new = a + DA;
[y_calc] = y_Functn(x,a_new);
chi_sqr_new = CurFit_chisqr(y,y_calc,inv_sigma_sqr,N_free)
while chi_sqr_old > (chi_sqr_new + 1) | lambda >= 0.001
if chi_sqr_new >= chi_sqr_old
lambda = lambda*10;
else
plot(x,y_calc)
a = a_new
lambda = lambda*0.1;
chi_sqr_old = chi_sqr_new;
[dyda] = CurFit_nonanal(x,a,delta_a);
for J = 1:length(a)
for K = J:length(a)
alpha(J,K) = sum(inv_sigma_sqr.*(dyda(:,J).*dyda(:,K)));
alpha(K,J) = alpha(J,K);
end;  % end K loop
end;  % end J loop
for K = 1:length(a)
beta(K) = sum(inv_sigma_sqr.*((y - y_calc).*dyda(:,K)));
end;  % end K loop
end;  % end if-then-else conditional
alpha_prime = alpha*(eye(length(a))*(1+lambda));
DA =  beta*inv(alpha_prime);
a_new = a + DA;
[y_calc] = y_Functn(x,a_new);
```

```
chi_sqr_new = CurFit_chisqr(y,y_calc,inv_sigma_sqr,N_free)
end;  % end while loop
clg;  hold off;
V = [min(x) max(x) -150 110]; axis(V);
plot(x,y,'o');hold on;
plot(x,y_calc -50);
xlabel('Frequency, kHz');  ylabel('Intensity, arb. units');
title('tube 10% phenol solidified 1yr  - 2K scans');
title('oven');
text(.13,.62,['a) experimental'],'sc');
text(.13,.47,['b)  fit'],'sc');
text(.13,.32,['c) two component fits'],'sc');
text(.7,.32,['liquid-like(---)'],'sc');
text(.7,.28,['180  ring flips (...)'],'sc');
text(.13,.22,['d)  residuals'],'sc');
residual = zeros(1,length(y_calc));
residual = y - y_calc;
max_res = ceil(max(abs(residual)));
two=a(1)*two_sites;
liq=a(2)*exp(-log(2)*(x/a(3)).^2);
plot(x,two - 100, ':');
plot(x,liq - 100, '--');
plot(x,residual-130,'+');
pause
error = sqrt(diag(inv(alpha)))';
etime(clock,t0)
flops;
```

```
Int_two_sites = sum(two_sites);
Int_gaussian = sum(exp(-log(2)*(x/a(3)).^2));
Fract_two_sites = a(1)*Int_two_sites/(a(1)*Int_two_sites + a(2)*Int_gaussian);
Fract_gaussian = a(2)*Int_gaussian/(a(1)*Int_two_sites + a(2)*Int_gaussian);
clg;  hold off;
V = [min(x) max(x) -100 110]; axis(V);
plot(x,y,'o',x,y_calc);hold on;
plot(x,residual-80,'+');
plot(x,two - 50, ':');
plot(x,liq - 50, '--');
xlabel('Frequency, kHz');  ylabel('Intensity, arb. units');
title('tube 10% phenol solidified 1yr - 2K scans');
title('2 month sample crushed, oven treated, 1yr - 2K scans');
f=100*Fract_two_sites;
text(.12,.6,['two-site = ',num2str(a(1)), ' ± ' , num2str(error(1))],'sc');
text(.12,.65,['liquid-like = ',num2str(a(2)), ' ± ' , num2str(error(2))],'sc');
text(.12,.85,['oven.1yr'],'sc');
text(.12,.75,['sigma = ',num2str(sigma)],'sc');
text(.12,.8,['reduced chi-sqr = ',num2str(chi_sqr_new)],'sc');
text(.65,.75,['experimental data - o '],'sc');
text(.65,.7,['best fit of data - __ '],'sc');
text(.65,.35,['two-site - ... '],'sc');
text(.65,.4,['liquid-like - --- '],'sc');
text(.65,.15,['residual - + '],'sc');
```

```
%calculate error for percent two-site
a1=a(1)*Int_two_sites;
e1=error(1)*Int_two_sites;
a2=a(2)*Int_gaussian;
e2=error(2)*Int_gaussian;
dwh=a1+a2;
der=sqrt(e1^2 +e2^2);
reld=(der/dwh)*100;
reln=(e1/a1)*100;
fa=a1/dwh;
fe=(sqrt(reld^2 +reln^2)*fa);  %relative uncertainty
text(.12,.7,['%  two-site=',num2str(f),'%  +/-  ',num2str(fe),'  %  '],'sc');
```

A.2.1. Subroutine: Curfit_Chisqr

```
function chi_sqr = Curfit_chisqr(y,y_calc,inv_sigma_sqr,N_free)
chi_sqr = (sum(inv_sigma_sqr*(y-y_calc).^2))/N_free;
```

A.2.2. Subroutine: CurFit_Nonanal

```
function [dyda] = CurFit_nonanal(x,a,delta_a)
% evaluates gaussian peak on a background
% Program 11-7, p242, Bevington
dyda = zeros(length(x),length(a));
y_plus_delta = zeros(length(x),1);
y_minus_delta = zeros(length(x),1);
a_temp = zeros(1,length(a));
for J = 1:length(a)
```

```
a_temp = a;  a_temp(J) = a(J) + delta_a(J);
[y_plus_delta] = y_Functn(x,a_temp);
a_temp(J) = a(J) - delta_a(J);
[y_minus_delta] = y_Functn(x,a_temp);
dyda(:,J) = ((y_plus_delta - y_minus_delta)/(2*delta_a(J)));
end;
```

A.2.3. Subroutine: Y_Functn

```
function [y_calc] = y_Functn(x,a)
two_sites = y_calc_new;
two_sites=100*two_sites/max(two_sites);
y_calc = a(1)*two_sites + a(2)*exp(-log(2)*(x/a(3)).^2)  + a(4);
```

A.3. PFGSE Displacement Profile Program

```
clc; clear; clg; hold off;
data_20ms=[FID intensity for 64 experiments - pts 2 and 3 of FID];
data_40ms=[FID intensity for 64 experiments - pts 2 and 3 of FID];
data_80ms=[FID intensity for 64 experiments - pts 2 and 3 of FID];
data_160ms=[FID intensity for 64 experiments - pts 2 and 3 of FID];
% calculate magnitude calculation/magnetization of first real and imag point
mag_20=abs(data_20ms(:,2)+data_20ms(:,3)*i);
mag_40=abs(data_40ms(:,2)+data_40ms(:,3)*i);
mag_80=abs(data_80ms(:,2)+data_80ms(:,3)*i);
mag_160=abs(data_160ms(:,2)+data_160ms(:,3)*i);
te=5.25e-3;      %encoding time in seconds
max_g=40 ;       %max gradient in gauss/cm
```

```
cm=1/(4*4257*te*max_g);  %caculate cm/pt
cm=cm*(1e6/100);         %convert cm to microns/pt
n1=32;          % number of positive experiments
n2=31;          %number of negative experiments
x1=n1*cm;       %negative axis limit
x2=n2*cm;       %positive axis limit
x_axis=linspace(-x1,x2,length(mag_20));
I=linspace(-1.9375,2,length(mag_20));   % current in amps used in exp
B_over_I = 20;  % gauss/cm A
for k=1:length(I)
G(k) = B_over_I * I(k);
end;
plot (G, mag_20,'-',G, mag_20,'o'); hold on;
plot (G, mag_40,'-',G, mag_40,'x');
plot (G, mag_80,'-',G, mag_80,'*'); grid;
plot (G, mag_160,'-',G, mag_160,'+');
xlabel('Gauss/cm');  ylabel('Magnetization, cm');
title('Diffusion times: o 20 ms, x 40 ms, * 80 ms, + 160 ms');
hold off; pause;
% fourier transformation of magnitude calculation
I_x_20 = abs(fftshift(fft(mag_20)));
I_x_40 = abs(fftshift(fft(mag_40)));
I_x_80 = abs(fftshift(fft(mag_80)));
I_x_160 = abs(fftshift(fft(mag_160)));
V=[-40 40 0 max(I_x_20)]; axis(V);
plot(x_axis,I_x_20,'-',x_axis,I_x_20,'o'); hold on;
```

```
plot(x_axis,I_x_40,'-',x_axis,I_x_40,'x');
plot(x_axis,I_x_80,'-',x_axis,I_x_80,'*');
plot(x_axis,I_x_160,'-',x_axis,I_x_160,'+');
xlabel('Displacement, microns');
text(0.8, .97,  ['Figure 2, Janusa et al.'], 'sc');
title('Liquid C3S Diffusion times: o 20 ms, x 40 ms, * 80 ms, + 160 ms');
text(0.7, 0.8,  ['Diffusion Times, td'], 'sc');
text(0.7, 0.7,  ['o - 20 ms'], 'sc');
text(0.7, 0.6,  ['x - 40 ms'], 'sc');
text(0.7, 0.4,  ['+ - 160 ms'], 'sc');
text(0.7, 0.5,  ['* - 80 ms'], 'sc');hold off;
```

A.4. Diffusion Coefficient Calculation from Displacement Profile

```
clc; clear; clg; hold off;
te= 5.25e-3;          % encoding time in sec
td=[-te/3 .02 .04 .08 .16]; %diffusion time in seconds
td_corr=td + te/3; % corrected diffusion time
error=[0 .5 .5 .5 .5 ];% in micron for micro axis
x_pt_5= [0 6e-4 8e-4 11e-4 15e-4]; %full width half height, microns
td_sqrt=td_corr.^(1/2);
x_pt_5=x_pt_5*1e4;
V=[-0.05 0.45 -5 20]; axis(V);
plot(td_sqrt, x_pt_5,'o'); hold on;
%least squares analysis
n=length(x_pt_5);
x=td_sqrt.^2;              % x square with x being amp^2
x_sum=sum(x);              % sum of x square
```

```
J=td_sqrt(1,:)*x_pt_5(1,:)';   % sum of x time y
d=[x_sum sum(td_sqrt);sum(td_sqrt) n];
de=det(d);              % d factor
m=[J sum(td_sqrt);sum(x_pt_5) n];
me=det(m)/de;           % slope
b=[x_sum J;sum(td_sqrt) sum(x_pt_5)];
be=det(b)/de;           % y intercept
m2=(me^2)/(4*4*log(2)); % calculate diffusion coeff.
D=m2*1e-8;  %convert to cm diff
y_calc=me*x_calc + be;
%error analysis
error1=(error(1,:)./x_pt_5(1,:));  %calculate percent uncertainty
error2=(td_sqrt(1,:).*error(1,:));  %calculate new error
error3=(sum(error2.^2))^.5;   %calculate sum xy error
errorsum=(sum(error.^2))^.5;
error4=(error3/J)*J*n;
error5=(errorsum/sum(x_pt_5))*sum(x_pt_5)*sum(td_sqrt);
error6=(error4^2 + error5^2)^.5;
error7=(error6/det(m))*det(m)/de;%me error
errorfinal=(error7/me)*(me^2)/(4*4*log(2))*1e-8;%convert to cm diff;
plot(x_calc,y_calc,'-');
text(0.8, .97,  ['Figure 3, Janusa et al.'], 'sc');
e = [0 .5 .5 .5 .5];
errorbar(td_sqrt, x_pt_5,e);
xlabel('(diffusion time)1/2');
ylabel('diffusion length, μm');
```

```
title('Diffusion plot Liquid C3S');
text(0.3, 0.3, ['D = ',num2str(D),' cm^2 s-1'], 'sc');
text(0.3, 0.2, ['error = ',num2str(errorfinal),' cm^2 s-1'], 'sc');
```

A.5. T1 Calculation - Inversion Recovery

```
% equation - M(t) = M_eq(1 - 2e^-t/T1)
global tau data
clc; clear; clg; hold off;
data=[-11.67 -11.56 -11.23 -10.33 -9.95 -7.99 -5.63 -2.61 2.13 5.92 9.54 13.38];
tau=[100e-6 200e-6 500e-6 1e-3 2e-3 5e-3 10e-3 20e-3 50e-3 .1 .2 .5];
subplot(211); plot(tau,data,'o');hold on;
%title('T1 calculation 90 degrees plot (largest peak positive/negative)');
xlabel('tau,sec'); ylabel('Intensity');
%Now, enter some guesses as to I and T1
Guess_I=9; Guess_T1=.005;Guess_A=1;
y_guess=Guess_I*(1 - Guess_A*exp(-tau/Guess_T1));
%Now, use the guesses as starting points for a simplex fit
E=fmins('func_invrec',[Guess_I Guess_T1 Guess_A]);
I_calc = E(1); T1_calc = E(2);A_calc=E(3);
y_calc=I_calc*(1 - A_calc*exp(-tau/T1_calc));
subplot(211); plot(tau,y_calc);hold off;
E(2)=E(2)*1e3;
text(0.6,0.7, ['T1 = ',num2str(E(2)),' ms'],'sc');
text(0.6,0.65, ['A = ',num2str(E(3))],'sc');
```

A.5.1. Subroutine: Func_Invrec of T1

```
function error_parameter = func_invrec(p);
I = p(1); T1 = p(2);A=p(3);
difference =I*(1 - A*exp(-tau/T1)) - data;
error_parameter = sum(difference.^2);
```

A.6. T2 Calculation

```
% equation - M(t) = Meq(e-t/T2)
clc; clear; clg; hold off;
I=[15.286 14.54 12.509 9.445 6.625];
A=log(I);
tau=[10e-6 20e-6 50e-6 100e-6 200e-6];
tau=tau*2;
%least squares analysis
n= length(tau);
x=tau.^2;              % x square with x being amp^2
x_sum=sum(x);          % sum of x square
J=tau(1,:)*A(1,:)';    % sum of x time y
d=[x_sum sum(tau);sum(tau) n];
de=det(d);             % d factor
m=[J sum(tau);sum(A) n];
me=det(m)/de;          % slope
b=[x_sum J;sum(tau) sum(A)];
be=det(b)/de;          % y intercept
m2=-1/me;
D=m2; % T2 calculation
```

```
x_calc = linspace(min(tau),max(tau),20);
y_calc = me*x_calc + be;
hold on;
plot(x_calc,y_calc,'-');
```

APPENDIX B

ADDITIONAL EXPERIMENTAL NMR SPECTRA

B.1. Nonlinear Least-Squares Analysis for Data in Table 4.1

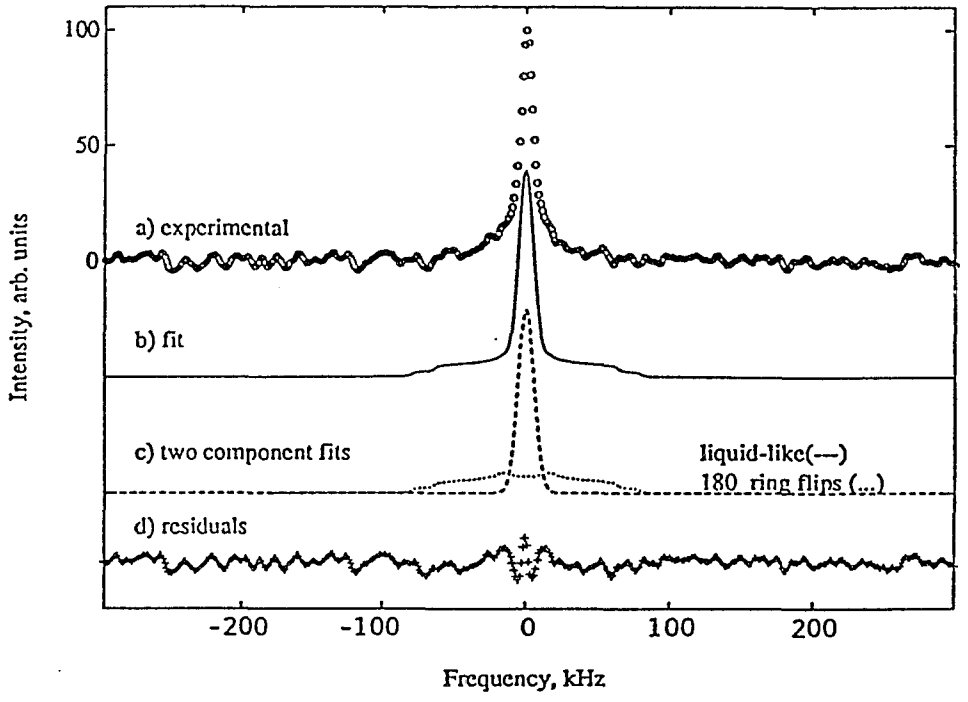

Figure B.1.1 Results from a nonlinear least–squares analysis of the ^2H NMR spectrum 1% d_5–phenol by wt. in white portland cement solidified in an NMR tube for one month: a) experimental ^2H NMR spectrum; b) best calculated fit with eq. 4.2; c) the fit is composed of two deuterium components: liquid–like (——) and 180° ring flips (...); d) residuals. $\chi^2_\nu = 0.82$. The amount of solid calcium phenoxide (phenol executing 180° ring flips) = 45 (2)%; the remaining phenol exists in a freely mobile, liquid–like phase and is not bound to the cement matrix.

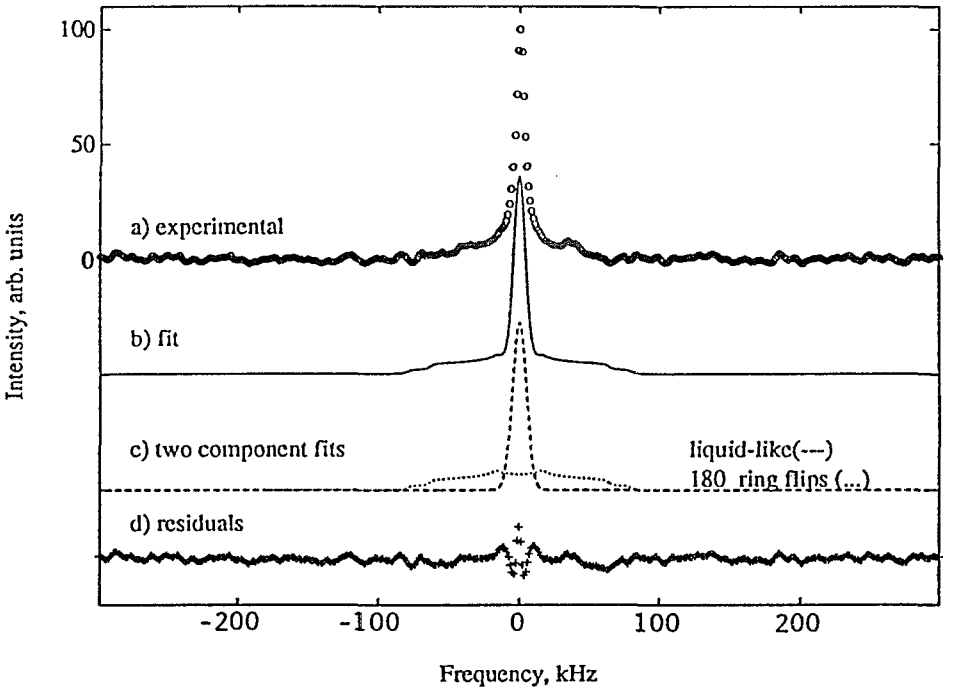

Figure B.1.2 Results from a nonlinear least–squares analysis of the ^2H NMR spectrum 1% d_5–phenol by wt. in white portland cement solidified in an NMR tube for one year: a) experimental ^2H NMR spectrum; b) best calculated fit with eq. 4.2; c) the fit is composed of two deuterium components: liquid–like (——) and 180° ring flips (...); d) residuals. $\chi^2_\nu = 0.95$. The amount of solid calcium phenoxide (phenol executing 180° ring flips) = 48 (2)%; the remaining phenol exists in a freely mobile, liquid–like phase and is not bound to the cement matrix.

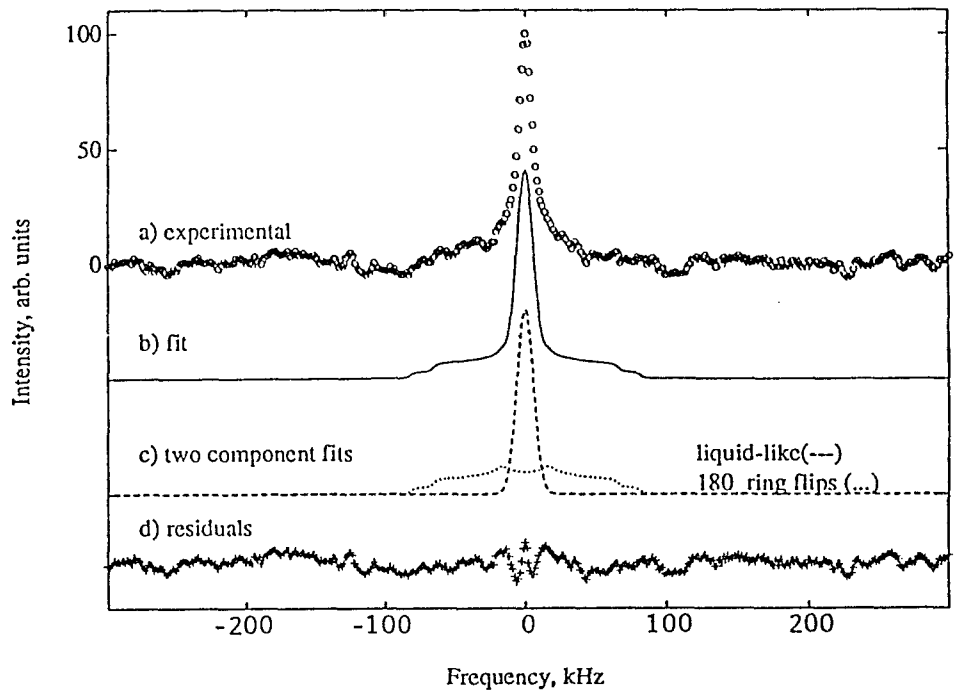

Figure B.1.3 Results from a nonlinear least–squares analysis of the ^2H NMR spectrum 1% d_5–phenol by wt. in white portland cement solidified in an NMR tube for 14 months: a) experimental ^2H NMR spectrum; b) best calculated fit with eq. 4.2; c) the fit is composed of two deuterium components: liquid–like (——) and 180° ring flips (...); d) residuals. χ^2_ν = 1.2. The amount of solid calcium phenoxide (phenol executing 180° ring flips) = 52 (2)%; the remaining phenol exists in a freely mobile, liquid–like phase and is not bound to the cement matrix.

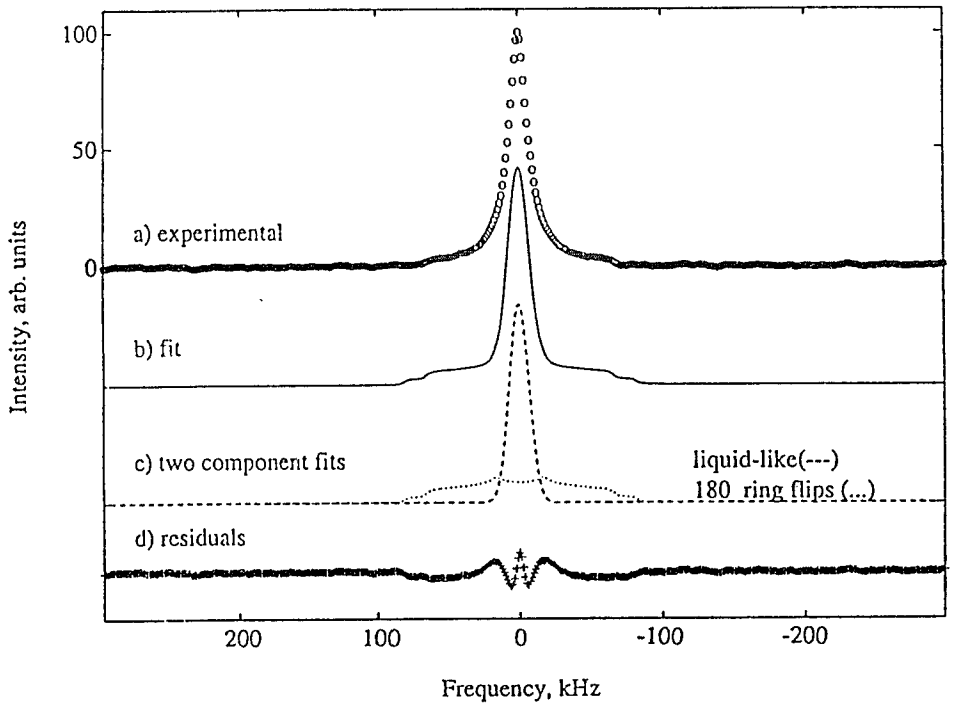

Figure B.1.4 Results from a nonlinear least–squares analysis of the ^{2}H NMR spectrum 10% d_5–phenol by wt. in white portland cement solidified in an NMR tube for one month: a) experimental ^{2}H NMR spectrum; b) best calculated fit with eq. 4.2; c) the fit is composed of two deuterium components: liquid–like (——) and 180° ring flips (...); d) residuals. $\chi^2_\nu = 0.55$. The amount of solid calcium phenoxide (phenol executing 180° ring flips) = 44 (2)%; the remaining phenol exists in a freely mobile, liquid–like phase and is not bound to the cement matrix.

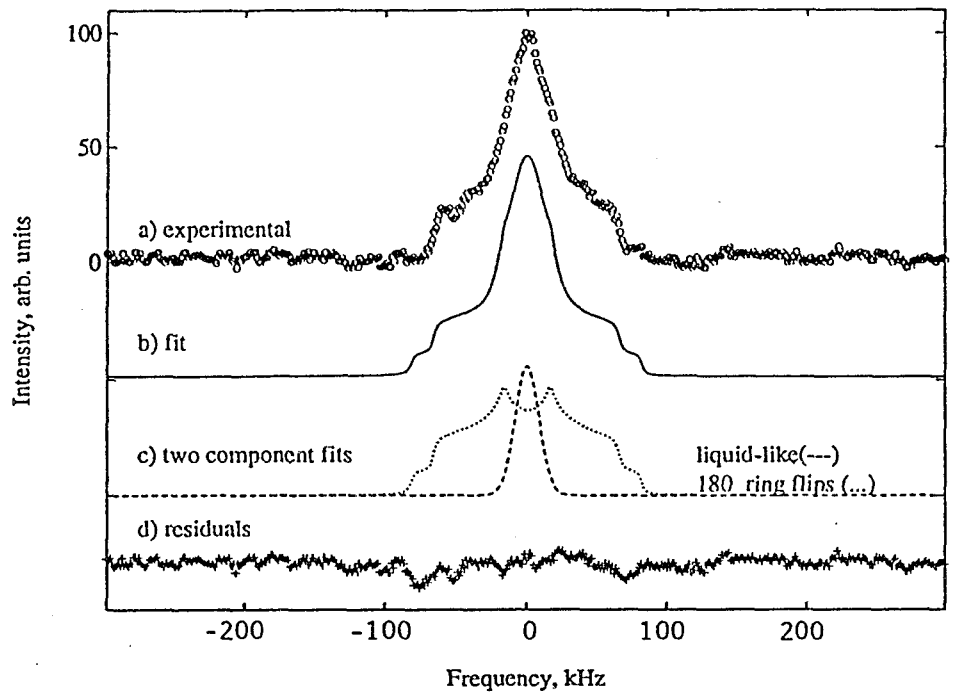

Figure B.1.5 Results from a nonlinear least–squares analysis of the ^2H NMR spectrum 10% d_5–phenol by wt. in white portland cement solidified in an NMR tube for 15 months: a) experimental ^2H NMR spectrum; b) best calculated fit with eq. 4.2; c) the fit is composed of two deuterium components: liquid–like (——) and 180° ring flips (...); d) residuals. $\chi^2_\nu = 1.1$. The amount of solid calcium phenoxide (phenol executing 180° ring flips) = 80 (2)%; the remaining phenol exists in a freely mobile, liquid–like phase and is not bound to the cement matrix.

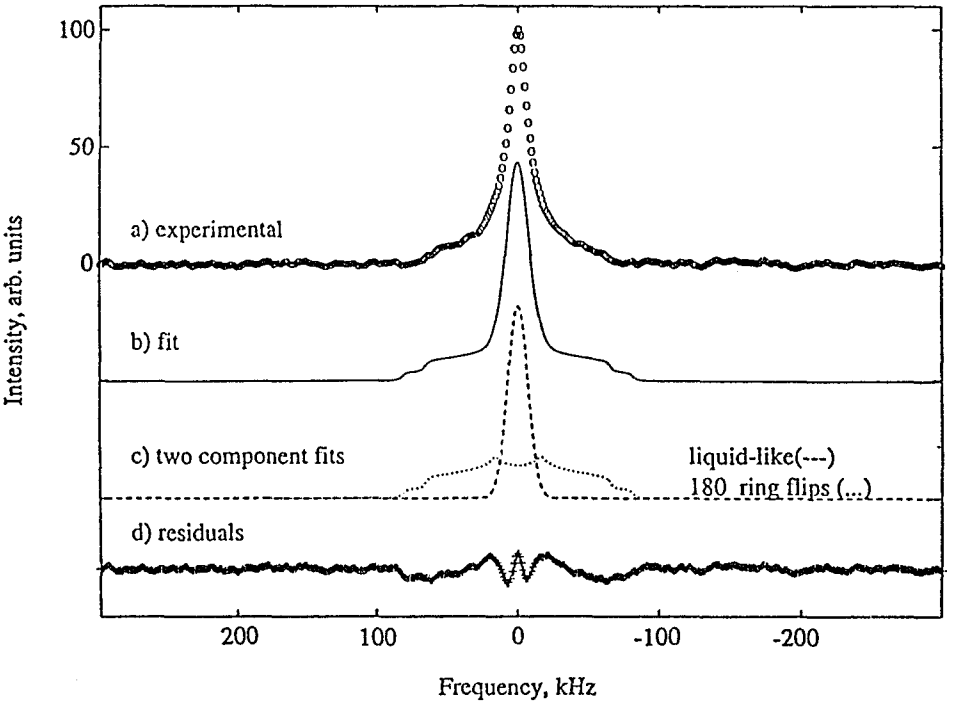

Figure B.1.6 Results from a nonlinear least–squares analysis of the ^2H NMR spectrum 10% d_5–phenol by wt. in white portland cement cured for two months, then crushed and studied as the powder: a) experimental ^2H NMR spectrum; b) best calculated fit with eq. 4.2; c) the fit is composed of two deuterium components: liquid–like (——) and 180° ring flips (...); d) residuals. $\chi^2_\nu = 0.85$. The amount of solid calcium phenoxide (phenol executing 180° ring flips) = 55 (2)%; the remaining phenol exists in a freely mobile, liquid–like phase and is not bound to the cement matrix.

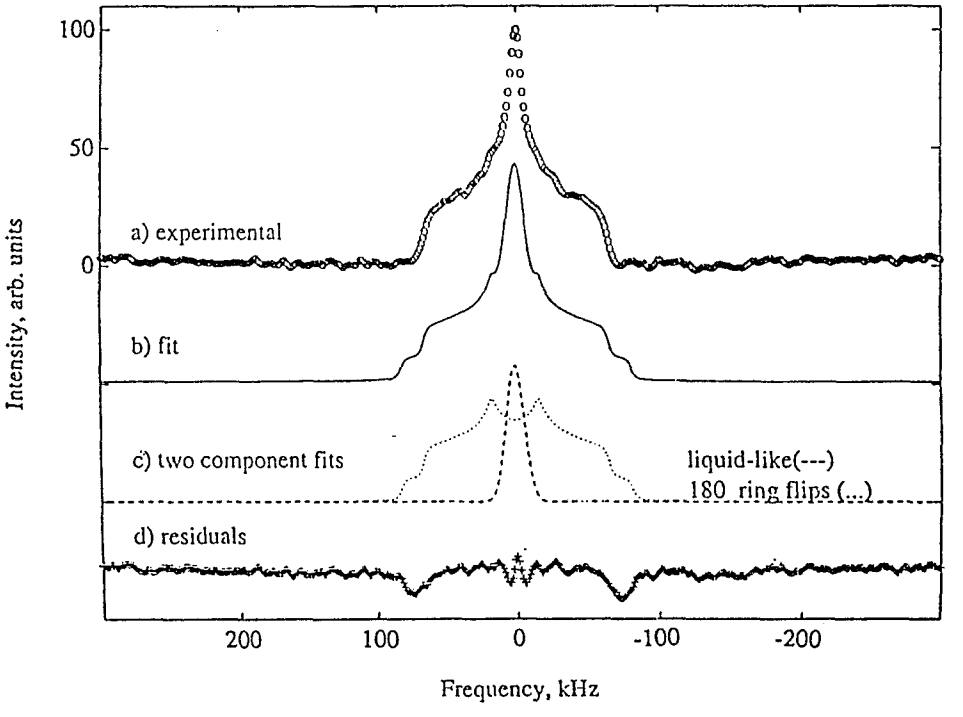

Figure B.1.7 Results from a nonlinear least–squares analysis of the ^2H NMR spectrum 10% d_5–phenol by wt. in white portland cement cured for two months, then crushed and shelved for an additional ten months (same sample as in B.1.6); b) best calculated fit with eq. 4.2; c) the fit is composed of two deuterium components: liquid–like (——) and 180° ring flips (...); d) residuals. $\chi^2_\nu = 1.1$. The amount of solid calcium phenoxide (phenol executing 180° ring flips) = 84 (2)%; the remaining phenol exists in a freely mobile, liquid–like phase and is not bound to the cement matrix.

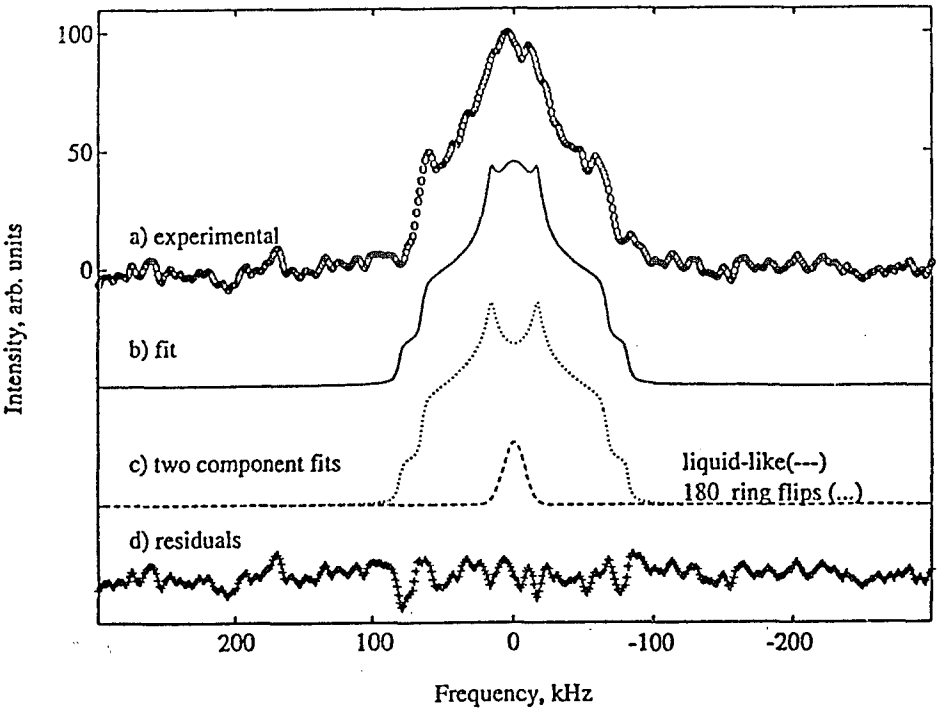

Figure B.1.8 Results from a nonlinear least–squares analysis of the ^2H NMR spectrum 10% d_5–phenol by wt. in white portland cement cured for two months, then crushed and oven treated for 36 hours at 90°C: a) experimental ^2H NMR spectrum; b) best calculated fit with eq. 4.2; c) the fit is composed of two deuterium components: liquid–like (——) and 180° ring flips (...); d) residuals. $\chi^2_\nu = 0.28$. The amount of solid calcium phenoxide (phenol executing 180° ring flips) = 95 (3)%; the remaining phenol exists in a freely mobile, liquid–like phase and is not bound to the cement matrix.

B.2. Supplementary Material

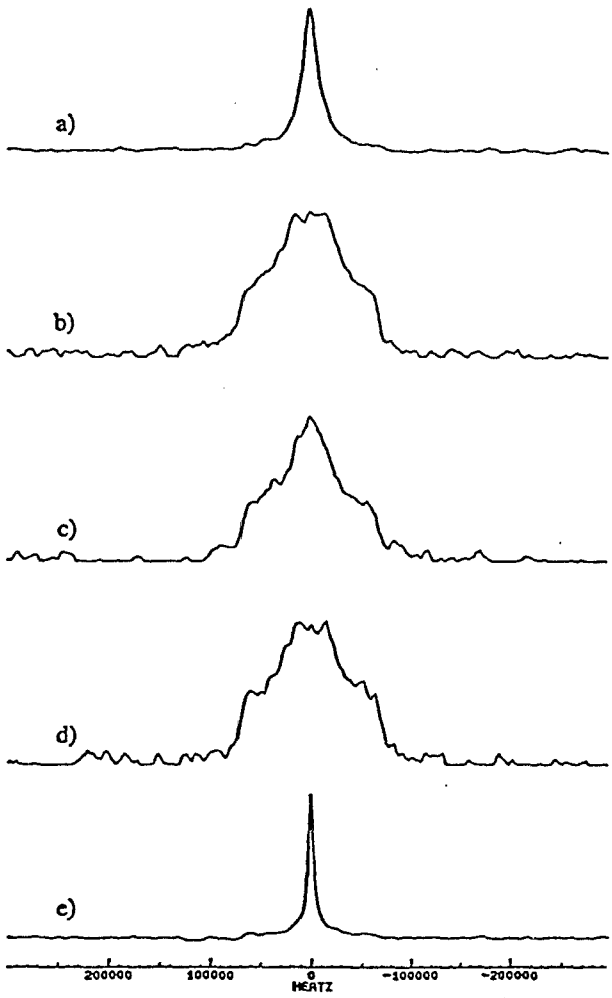

Figure B.2.1 Deuterium NMR spectra of monitoring the sample mass (water gain/loss) for 10% d_5–phenol by weight in white portland cement that has been crushed after 1 month cure (all spectra of same sample): a) immediately after crushing, weight - 0.231 g; shows large liquid-like phenol resonance; b) oven treated for 24 hours at 95°C, weight - 0.200 g; shows very little liquid-like phenol; c) approximately one week later, weight - 0.211 g; shows combination of liquid-like and solid calcium phenoxide component; d) oven treated for an additional 2 hours, weight - 0.206 g, spectrum similar to b; e) addition of 0.1 ml water; shows very little solid calcium phenoxide component - almost all the phenol/cement bonds are broken by solvation process.

APPENDIX C

HOLE-BURNING POWER CALCULATIONS

C.1. Hole-Burning Calculations for ^{13}C Pulses

Data

burn pulse duration - 10 ms

voltage peak to peak (V_{pp}) - 17.4 mV

hard 90° pulse - 6.5 μs

V_{pp} - 1.1 V

power - 60.4 W

γ_{Pb} -6728 rad s^{-1} G^{-1}

(1) Calculate field strength, B_1, of the hard 90° pulse, θ, for a duration of time, t_p.

$$\theta = \gamma B_1 t_p \qquad \text{(C.1)}$$

$$\pi/2 = (6728 \text{ rad s}^{-1} \text{ G}^{-1})\ (B_1)\ (6.5 \times 10^{-6} \text{ s})$$

$$B_1 = 36.0 \text{ G}$$

(2) Calculate power of burn pulse with the following equation:

$$P = \frac{V_{pp}^2}{8R} \qquad \text{(C.2)}$$

where R is resistance in ohms.

$$P = (17.4 \times 10^{-3} \text{ V})^2 / 8\ (50\ \Omega)$$

$$P = 7.6 \times 10^{-7} \text{ W}$$

(3) Calculate the field strength of the burn pulse by comparison to hard pulse,

$$B_1 = 3\sqrt{\frac{PQ}{\nu V}} \qquad \text{(C.3)}$$

where comparing the burn pulse to the hard pulse leads to the following relationship:

$$\frac{B_{1burn}}{B_{1hard}} = \sqrt{\frac{P_{burn}}{P_{hard}}} \qquad (C.4)$$

$$B_{1burn} = (36.0\ G)\sqrt{\frac{7.6 \times 10^{-7} W}{60.4\ W}}$$

$$B_{1burn} = 4.0 \times 10^{-3}\ G$$

(4) Calculate the tip angle of the burn pulse using equation C.1.

$$\theta = (6728\ rad\ s^{-1}\ G^{-1})\ (4.0 \times 10^{-3}\ G)\ (10.0 \times 10^{-3}\ s)\ (360 / 2\ \pi)$$

$\theta = 15°$ tip angle for burn pulse

C.2. Hole-Burning Calculations for ^{207}Pb Pulses

Data

burn pulse duration - 5 ms

voltage peak to peak (V_{pp}) - 11.6 mV

hard 90° pulse - 4 μs

V_{pp} - 2.72 V

power - 337 W

γ_{Pb} - 5596 rad s^{-1} G^{-1}

(1) Calculate field strength, B_1, of the hard 90° pulse, θ, for a duration of time, t_p, using equation C.1.

$$\pi/2 = (5596 \text{ rad } s^{-1} G^{-1}) (B_1) (4.0 \times 10^{-6} \text{ s})$$

$$B_1 = 70.2 \text{ G}$$

(2) Calculate power of burn pulse with equation C.2.

$$P = (11.6 \times 10^{-3} \text{ V})^2 / 8 (50 \Omega)$$

$$P = 3.4 \times 10^{-7} \text{ W}$$

(3) Calculate the field strength of the burn pulse by comparison to hard pulse using equation C.4.

$$B_{1burn} = (70 .2 \text{ G}) \sqrt{\frac{3.4 \times 10^{-7} \text{W}}{337 \text{ W}}}$$

$$B_{1burn} = 2.2 \times 10^{-3} \text{ G}$$

(4) Calculate the tip angle of the burn pulse using equation C.1.

$$\theta = (5596 \text{ rad } s^{-1} G^{-1}) (2.2 \times 10^{-3} \text{ G}) (5.0 \times 10^{-3} \text{ s}) (360 / 2 \pi)$$

$$\theta = 4° \text{ tip angle for burn pulse}$$

VITA

Michael Albert Janusa was born in New Orleans, Louisiana on November 1, 1963. He graduated from St. John Vianney Prep high school in May 1981. He received a B.S. degree in November 1985 in Agricultural Engineering from Louisiana Tech University. He married Cheryl Young on May 28, 1988 and entered graduate school at Louisiana State University in June 1988. On October 22, 1991 his first child was born named Michael Joseph.

His research is concentrated in the area of environmental chemistry where he has developed new methods for assessing solidification/stabilization (S/S) of hazardous waste using solid–state nuclear magnetic resonance for the purpose of diagnosing on a microscopic level its performance as a hazardous waste disposal technique. He has three publications: (1) "Structure of the Eudesmanolide Gazaniolide", Janusa, M.A.; Jeansonne, M.S.; Fronczek, F.R.; Watkins, S.F. *Acta Cryst.*, **1990**, *C46*, 2474-2476; (2) "Solid-State NMR Characterization of Organics in Cement", Cartledge, F.K.; Butler, L.G.; Tittlebaum, M.E.; Akhter, H.; Chalassani, D.; Janusa, M.A.; Yang, S. *Cement Industry Solutions to Waste Management,* Proceedings, 1st Intl. Symp., Calgary, Oct. 1992; Canadian Portland Cement Association, Toronto, **1992**, 289-305; (3) "Solid-State Deuterium NMR Spectroscopy of d_5-Phenol in White Portland Cement: A New Method for Assessing Solidification/Stabilization", Janusa, M.A.; Wu, X.; Cartledge, F.K.; Butler, L.G. *Environ. Sci. Technol.*, **1993**, in press.

DOCTORAL EXAMINATION AND DISSERTATION REPORT

Candidate: Michael A. Janusa

Major Field: Chemistry

Title of Dissertation: Development of New Methods for Assessing Solidification/Stabilization of Hazardous Waste Using Solid-State Nuclear Magnetic Resonance Techniques

Approved:

Leslie S. Butler
Major Professor and Chairman

Daniel Fogel
Dean of the Graduate School

EXAMINING COMMITTEE:

Edward B. Coughlin

Robert J. Gale

Franklin Cartledge

Willard Daly

Julian Evans

Date of Examination:

4/6/93